TABLE DES MATIÈRES

LISTE DES TABLEAUX

Page

LISTE DES FIGURES

LISTE DES ABRÉVIATIONS, SIGLES ET ACRONYMES

3-D	Trois dimensions
AM	Fabrication additive (*Additive manufacturing*)
APDL	*ANSYS Parametric Design Language*
ASTM	*American Society for Testing Material*
CAO	Conception assistée par ordinateur
CT	*Computed tomography*
DDL	Degrés de liberté (*Degrees of freedom*)
DIC	Corrélation d’image numérique (*Digital image correlation*)
EBM	Fusion sélective sur lit de poudre par faisceau d’électrons (*Electron beam melting*)
EDM	Électroérosion (*Electrical discharge machining*)
FDA	*U.S. Food and Drug Administration*
FDETS	Fonds de développement de l'ÉTS
FE	Éléments finis (*Finite element*)
FEA	Analyse par éléments finis (*Finite element analysis*)
FEM	Modèle d’éléments finis (*Finite element model*)
FOV	Champ de vision (*Field of view*)
FRQ-NT	Fonds de recherche du Québec Nature et Technologies
ISO	Organisation internationale de normalisation (*International Organization for Standardization*)
LENS	*Laser Engineered Net Shaping*
NSERC	Conseil de recherches en sciences naturelles et en génie du Canada (*Natural Sciences and Engineering Research Council of Canada*)

PVF	Fraction volume des pores (*Pore volume fraction*)
RVE	Volume élémentaire représentatif (*Representative volume element*)
S_{RVE}	Taille de volume élémentaire représentatif (*Size of the representative volume element*)
S_{RVE}^{min}	Taille minimale de volume élémentaire représentatif (*Minimum size of the representative volume element*)
SLM	Fusion sélective sur lit de poudre par faisceau laser (*Selective laser melting*)
STL	Stéréolithographie (*Stereolithography*)
S_V	Surface spécifique (*Specific surface area* or *Surface-to-volume ratio*)

LISTE DES SYMBOLES ET UNITÉS DE MESURE

d_{10}, µm	Diamètre équivalent où 10% de la distribution des pores est de taille inférieure
d_{50}, µm	Diamètre équivalent où 50% de la distribution des pores est de taille inférieure (ou diamètre médian)
d_{90}, µm	Diamètre équivalent où 90% de la distribution des pores est de taille inférieure
E, GPa	Module de Young
S_Y, MPa	Contrainte d'écoulement
S_{UT}, MPa	Contrainte ultime
ν	Coefficient de poisson
δ, mm/mm	Déformation à la rupture

INTRODUCTION GÉNÉRALE

0.1 Problématique

En orthopédie, le remplacement d'os endommagés nécessite la mise en place d'un implant par le biais d'une intervention chirurgicale. Chaque année, un grand nombre de patients ont recours à ce type d'opération, notamment pour la hanche, le genou et l'épaule. De plus, entre 2013 et 2014 au Canada, 9 % des 49 500 arthroplasties de la hanche réalisées étaient des reprises (Institut Canadien d'Information sur la Santé, 2015), c'est-à-dire une opération additionnelle suite à certaines complications comme le descellement aseptique de l'implant (24 % des cas). Similairement, aux États-Unis, il est prévu d'ici 2030 qu'environ 97 000 et 268 000 opérations de reprise soient nécessaires pour la hanche et le genou respectivement (Kurtz et al., 2007).

Ces chirurgies de reprise sont principalement causées par la grande différence de rigidité entre l'implant et les tissus osseux (Cameron, Macnab et Pilliar, 1978; Huiskes, Weinans et Rietbergen, 1992; Robertson, St Pierre et Chahal, 1976). En effet, les matériaux actuellement utilisés pour fabriquer les tiges fémorales sont généralement des métaux comme les alliages de titane, de cobalt-chrome ou les aciers inoxydables. Sous forme dense, la rigidité de ces métaux peut varier autour de 110 GPa pour les alliages de titane et entre 200 à 230 GPa pour les aciers inoxydables et les alliages de cobalt-chrome. Les os quant à eux possèdent une rigidité variant de 5 à 30 GPa (Currey, 2012) et leur morphologie, en apparence poreuse, est loin de s'apparenter à celle des matériaux métalliques denses.

Les activités quotidiennes telle que se lever, marcher et monter les escaliers sollicitent les os. Au niveau du fémur par exemple, ces sollicitations sont principalement créées par le poids du corps et les muscles abducteurs (Taylor, 2006). Toutefois, dans le cas où une tige fémorale est intégrée au sein d'un fémur, ces chargements sont presque entièrement déviés (ou repris) par l'implant dû au fait qu'il est beaucoup plus rigide que le fémur. Ce phénomène appelé déviation des contraintes (*stress shielding* en anglais) induit un changement pathologique au niveau de la distribution des contraintes au sein des tissus osseux en périphérie de l'implant (Huiskes et al., 1987). Par conséquent, sachant que l'os est un matériau qui adapte sa morphologie en fonction des chargements qu'il subit, une diminution de la densité minérale osseuse est observée autour de l'implant (Huiskes et al., 1987). Ce phénomène est appelé remodelage osseux (*bone remodeling* en anglais).

À long terme, étant donné que l'os présente une densité minérale osseuse anormalement basse autour de l'implant, les risques comme le descellement aseptique de l'implant ou la fracture de l'os sont considérablement augmentés (Kröger et al., 1998). Ceci démontre donc un inconvénient majeur lié aux implants présentement commercialisés et fabriqués à partir d'un matériau métallique dense. Pour remédier à cette problématique, la conception d'implants possédant des propriétés mécaniques semblables à celles des tissus osseux humains devient souhaitable.

0.2 Solution proposée

Une des solutions possibles pour aborder cette problématique est de concevoir des implants à partir de mousses métalliques plutôt qu'à partir de matériaux métalliques denses (Gibson, Ashby et Harley, 2010; Lefebvre, 2013). En effet, dû à leur morphologie poreuse, cette nouvelle génération d'implant possède plusieurs avantages par rapport à leurs prédécesseurs, dont entre autres (Gibson, Ashby et Harley, 2010) :

- Un comportement mécanique similaire à celui des os en contrôlant la porosité de la structure;
- Une réduction du phénomène de déviation des contraintes et par le fait même une diminution du phénomène de remodelage osseux;
- Une croissance osseuse au sein de la structure poreuse permettant une meilleure stabilisation initiale de l'implant;
- Une grande surface spécifique favorisant la venue de plusieurs facteurs biologiques.

Même si le développement de structures poreuses pour les applications médicales est étudié depuis plusieurs années, ce sujet de recherche est toujours très actif comme peut le témoigner le nombre grandissant de publications au cours des dernières années. À cet effet, la fabrication et la caractérisation des propriétés biologiques, morphologiques et mécaniques des structures poreuses (Rivard et al., 2014; Yan et al., 2015; Zhao et al., 2016), le développement d'outils de conception numériques (Hedayati et al., 2016; Khanoki et Pasini, 2012; Wieding, Wolf et Bader, 2014) et la réalisation d'essais *in-intro* et *in-vivo* (Arabnejad et al., 2016; Khanoki et al., 2016; Pattanayak et al., 2011) sont des aspects primordiaux à considérer pour l'utilisation des mousses à titre d'implants orthopédiques. C'est d'ailleurs dans cette veine que le présent projet doctoral est orienté.

0.3 Objectifs de recherche

L'objectif principal de ce projet est de modéliser, fabriquer et caractériser mécaniquement et morphologiquement des mousses métalliques dont les propriétés mécaniques vont se rapprocher de celles de l'os humain et dont la morphologie va favoriser la croissance osseuse, tout en mettant un accent particulier sur la modélisation par éléments finis du comportement mécanique des mousses. Ceci permettra ainsi de développer des outils de simulation numériques pour la conception d'implants métalliques poreux. Afin de répondre à l'objectif global du projet, ce dernier est segmenté en trois objectifs spécifiques qui sont atteints de façon séquentielle et publiés dans des articles scientifiques distincts :

1. Modéliser, caractériser et valider expérimentalement la morphologie de structures poreuses fondée sur l'approche du volume élémentaire représentatif;
2. Caractériser numériquement et expérimentalement les propriétés mécaniques de mousses métalliques à l'aide de la méthode des éléments finis et d'essais de traction;
3. Concevoir, fabriquer, modéliser et tester mécaniquement une tige fémorale intégrant une structure métallique poreuse.

0.4 Organisation de la thèse

Une revue de la littérature des structures poreuses est d'abord présentée au Chapitre 1. Les principaux résultats obtenus lors de ces travaux de recherche permettant d'atteindre les trois objectifs spécifiques ont été publiés dans trois articles de revue qui sont présentés dans les

Chapitres 2, 3 et 4. Enfin, une discussion générale, suivie d’une conclusion générale et de recommandations sont proposées à la fin de cette thèse.

Article 1 : Développement et validation expérimentale de la méthodologie utilisée pour la génération de la morphologie de mousses métalliques.

Cette partie est présentée dans le Chapitre 2 et contient le premier article intitulé : "*Modeling of metallic foam morphology using the Representative Volume Element approach: Development and experimental validation*" par C. Simoneau, P. Terriault, J. Rivard, V. Brailovski publié dans International Journal of Solids and Structures, 2014, vol. 51, n° 21, p. 3633-3641.

Article 2 : Conception, fabrication et propriétés mécaniques de mousses métalliques.

Cette partie est présentée dans le Chapitre 3 et contient le deuxième article intitulé : "*Design, manufacture and tensile properties of stochastic porous metallic structures*" par C. Simoneau, V. Brailovski, P. Terriault publié dans Mechanics of Materials, 2016, vol. 94, p. 26-37.

Article 3 : Conception, fabrication, simulation et test mécaniques d’une tige fémorale poreuse.

Cette partie est présentée dans le Chapitre 4 et contient le troisième article intitulé : "*Development of a porous metallic femoral stem: design, simulation, manufacture and mechanical test*" par C. Simoneau, P. Terriault, B. Jetté, M. Dumas et V. Brailovski publié dans Materials & Design, In Press.

Enfin, il est à noter que certains résultats de la thèse ont également été présentés sous forme d’affiches et présentation orale lors de quatre congrès internationaux :

- V. Brailovski, P. Terriault, S. Prokoshkin, C. Simoneau, J. Rivard and S. Dubinskiy (2015). « Superelastic Nickel-free Porous Materials for Load-bearing Medical Implants: Fabrication and Modeling », Paper presented at the 14th International Conference on Martensitic Transformation, ICOMAT 2014, July 6 – July 11 2014, Bilbao, Spain (Vol. 2, Supplement 3, 511-516).

- C. Simoneau, P. Terriault and V. Brailovski (2016). « Stochastic porous metallic structures for biomedical application: mesoscale modeling, manufacturing and testing », Conference abstract presented at the 10th World Biomaterials Congress, WBC 2016, May 17 – May 22 2016, Montreal, Canada (Front. Bioeng. Biotechnol.).
- C. Simoneau, P. Terriault and V. Brailovski (2016). « Multiscale modeling and additive manufacturing of stochastic porous structures for biomedical application », Paper presented at the 9th International Conference on Porous Metals and Metallic Foams Technology, METFOAM 2015, August 31 – September 2 2015, Barcelona, Spain (submitted).
- V. Brailovski, P. Terriault, C. Simoneau, M. Dumas and B. Jetté (2016). « Development of a biomimetic metallic femoral stem: methodological approach », Paper presented at the 9th International Conference on Processing & Manufacturing of Advanced Materials, THERMEC 2016, May 29 – June 3 2016, Graz, Austria (submitted).

CHAPITRE 1

REVUE DE LA LITTÉRATURE

Ce chapitre présente tout d'abord une brève introduction aux tissus osseux afin de fournir des informations pour l'éventuelle conception d'un implant possédant des caractéristiques similaires à l'os. Ensuite, une revue de la littérature concernant l'utilisation des structures métalliques poreuses pour applications médicales est présentée. Les quatre thèmes suivants sont abordés : exigences fonctionnelles biomécaniques, procédés de mise en forme, méthodes de caractérisation et simulations numériques. Pour chaque thème, une courte discussion sur les axes de recherche adoptés dans la thèse ainsi qu'une liste des principaux outils utilisés sont présentées. Il est à noter qu'une grande partie des informations fournies dans ce chapitre peuvent également être retrouvée dans les différents livres ou articles de revue suivants : Banhart (2001), Brailovski et Terriault (2016), Dukhan (2013), Gibson et Ashby (1999).

1.1 Introduction aux tissus osseux

Les os sont formés de deux types de tissus, soit l'os cortical (*cortical* ou *compact bone* en anglais) et l'os spongieux (*spongious* ou *trabecular bone* en anglais). Tel qu'illustré à la Figure 1.1, l'os cortical et l'os spongieux se situent respectivement aux surfaces périphérique et intérieure de l'os. En raison de sa densité plus élevée, l'os cortical est plus dur, plus résistant et plus rigide que l'os spongieux : module de Young variant entre 5 et 30 GPa pour l'os cortical (Currey, 2012) et variant entre 0.01 et 3 GPa pour l'os spongieux (Gibson, 2005). Toutefois, le volume occupé par l'os spongieux est supérieur à celui de l'os cortical. De plus, en raison de sa structure hétérogène et poreuse, l'os (en particulier l'os spongieux) possède des propriétés mécaniques fortement influencées par la densité du tissu.

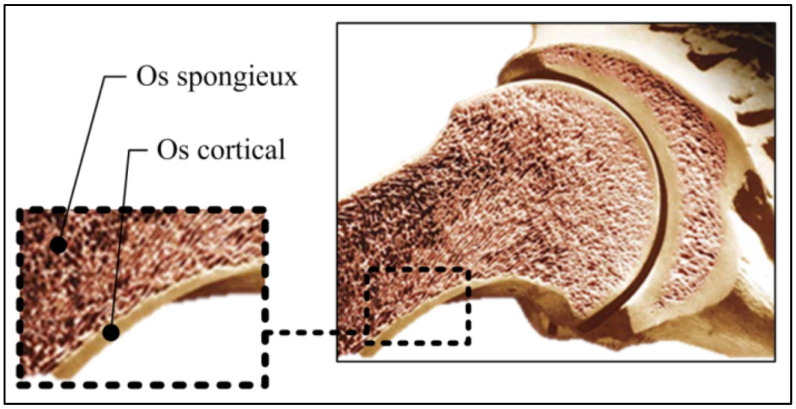

Figure 1.1 Structure et nomenclature de l'os
Tirée et adaptée de Britannica Online Encyclopedia

1.2 Exigences fonctionnelles des structures poreuses pour les applications médicales

Afin que les structures poreuses métalliques (également appelé mousses métalliques ou matériaux poreux) puissent être utilisés en tant qu'implant, certaines exigences biologiques et mécaniques se doivent d'être remplies. Cette section effectue un bref survol de ces exigences biomécaniques. Un traitement plus détaillé peut être trouvé dans les ouvrages suivants : Gibson, Ashby et Harley (2010), Lefebvre (2013), Levine et al. (2006) ou Ryan, Pandit et Apatsidis (2006).

1.2.1 Exigences biologiques

Les mousses métalliques doivent posséder une porosité ouverte, c'est-à-dire une interconnectivité des pores, ainsi qu'une taille de pore variant entre 50 et 800 µm afin de favoriser la formation de tissus osseux minéralisés au sein de la structure poreuse (Bobyn et al., 1980; Lefebvre, 2013). Il est à noter que cette plage de taille des pores varie légèrement d'un auteur à un autre. La limite inférieure (50 µm) est établie en fonction de la taille des ostéoblastes variant entre 25 et 50 µm (cellules constituant le tissu osseux). À l'opposé, des pores possédants une taille supérieure à la limite de 800 µm vont initier le risque de formation de tissus fibreux et par conséquent, entraver la formation de tissus minéralisés (Bobyn et Miller, 1994).

En se basant sur des données de la littérature sur les tissus osseux humains (Coelho et al., 2009; Martin, 1984), une porosité variant entre 30 et 50 % devrait être visée afin de maximiser la surface spécifique des structures poreuses (*specific surface area* ou *surface-to-volume ratio* en anglais). Ce faisant, les capacités de remodelage osseux seront augmentées (Beaupré, Orr et Carter, 1990). De plus, une grande surface spécifique ainsi qu'une excellente perméabilité vont permettre la croissance, la migration et la prolifération des cellules au sein de la structure poreuse (Gibson, Ashby et Harley, 2010; Min et al., 2004).

L'utilisation de métaux biocompatibles comme le titane commercialement pur et allié comme le Ti-6Al-4V, l'acier inoxydable 316L, le tantale, le superalliage cobalt-chrome-molybdène est à privilégier puisque ces matériaux restent relativement inertes *in-vivo* et ne provoquent pas de réaction inflammatoire des tissus osseux entourant l'implant (Levine et al., 2006; Ryan, Pandit et Apatsidis, 2006).

La résistance à la corrosion est une autre exigence à laquelle doivent répondre les structures métalliques poreuses. En effet, en plus d'influencer le comportement mécanique des mousses sur le plan de résistance à la fatigue et de la contrainte ultime (Ryan, Pandit et Apatsidis, 2006), la corrosion peut mener à des réactions allergiques (Lefebvre, 2013). Les matériaux métalliques généralement utilisés présentent une bonne résistance à la corrosion due à la création d'une fine couche passive d'oxyde (Ryan, Pandit et Apatsidis, 2006). Par ailleurs, Seah, Thampuran et Teoh (1998) mentionnent que la résistance à la corrosion est améliorée lorsque l'architecture des mousses métalliques est ouverte et interconnectée favorisant ainsi le passage d'un fluide.

En raison du fait que les matériaux métalliques utilisés sont généralement inertes, ces derniers ne s'attachent pas directement aux tissus osseux (Levine et al., 2006; Ryan, Pandit et Apatsidis, 2006). Dans le but de provoquer cette réaction biologique, il est nécessaire de créer des matériaux bioactifs. Ceci est généralement accompli lorsqu'un revêtement d'hydroxyapatite, principal minéral constituant les tissus osseux, est appliqué sur l'implant (*bone-like hydroxyapatite* en anglais). Par exemple, Kim et al. (1996) et bien d'autres ont créé un tel revêtement in vitro à l'aide de traitements alcalins et thermiques suivi par un bain dans un fluide corporel simulé.

1.2.2 Exigences mécaniques

Bien que les mousses métalliques destinées pour des applications orthopédiques soient majoritairement conçues pour supporter des charges de compression, l'étude du comportement en flexion, tension et torsion reste inévitable en raison des chargements multiaxiaux que vont subir les implants.

De manière générale, le module de Young des mousses métalliques doit se rapprocher le plus possible de celui des tissus osseux dans le but de minimiser le phénomène de déviation des contraintes. Il s'agit de l'une des principales exigences mécaniques à considérer. De plus, la résistance mécanique des mousses métalliques (limite d'écoulement et contrainte ultime) se doit d'être plus élevée que celle des tissus osseux afin de prévenir la défaillance de l'implant avant celle des os (Bansiddhi et al., 2008; Lefebvre, 2013).

Les mousses métalliques doivent également posséder une excellente résistance à la fatigue sachant que, par exemple, l'articulation de la hanche subit environ 1.1 million de cycles de marche par année. Il est cependant bien connu qu'en raison de l'hétérogénéité de la structure poreuse, et donc à l'inévitable présence de concentrateurs de contrainte, la résistance en fatigue des matériaux poreux est plus faible que celle des matériaux denses (Yue, Pilliar et Weatherly, 1984). Cependant, Brenne, Niendorf et Maier (2013), Cook et al. (1988) et Van Hooreweder et al. (2016) mentionnent que certains traitements thermiques (recuits et compression isostatique à chaud) peuvent être appliqués aux mousses métalliques dans le but d'améliorer leur résistance en fatigue. Van Hooreweder et al. (2016) mentionnent également qu'un post-traitement du fini de surface par attaque chimique permet d'adoucir les concentrateurs de contrainte et donc d'améliorer la durée de vie en fatigue des structures poreuses.

Lors de l'insertion de l'implant au sein des tissus osseux, un ajustement serré (*press-fit* en anglais) permet d'offrir une stabilité initiale adéquate évitant ainsi d'utiliser du ciment osseux lors de l'intervention chirurgicale. Par conséquent, il est nécessaire que la mousse métallique possède une bonne résistance à l'usure pour empêcher l'arrachement (ou le détachement) de particules ou débris métallique pouvant causer des problèmes usures au sein des articulations (*third-body wear* en anglais) ou des réactions inflammatoires à corps étrangers (Lefebvre, 2013).

1.2.3 Discussion

En raison du fait que les exigences fonctionnelles précédemment listées sont très nombreuses, ces dernières ne sont pas toutes atteintes dans le cadre de ce projet. Cependant, un accent particulier sera porté au niveau des plus importantes, soient :

- Des pores interconnectés de taille optimale favorisant la croissance osseuse;
- Une rigidité se rapprochant le plus possible de celle de l'os;
- Une résistance mécanique supérieure à celle de l'os;
- L'utilisation des matériaux biocompatibles.

Enfin, il est à noter qu'afin de pleinement satisfaire ce cahier des charges, la porosité (*porosity* ou *pore volume fraction* ou PVF en anglais) est l'élément clé à considérer puisque ce paramètre a une influence directe sur la morphologie ainsi que sur les propriétés mécaniques des structures poreuses.

1.3 Fabrication des structures poreuses

De nombreux procédés de fabrication sont disponibles pour la mise en forme des mousses métalliques (voir Banhart (2001), Baumeister et Weise (2013), Ryan, Pandit et Apatsidis

(2006) ou Singh et al. (2010a) par exemple). Banhart (2001) et Baumeister et Weise (2013) proposent de catégoriser ces méthodes de fabrication en fonction de l’état de la matière première, c’est-à-dire le métal sous une forme solide (poudre), liquide ou gazeuse.

Pour les applications médicales, les procédés de fabrication impliquant la métallurgie des poudres ont été fréquemment adoptés (Brailovski et Terriault, 2016; Ryan, Pandit et Apatsidis, 2006). Il est cependant important de mentionner que depuis environ une décennie les technologies de fabrication additive (FA) métallique sont de plus en plus répandues pour la mise en forme de structures métalliques poreuses pour applications médicales. En effet, un rapide survol de la littérature permet de facilement constater le virage récent vers les technologies de FA métallique (Hao, Li et Yang, 2016; Khanoki et al., 2016; Yan et al., 2015; Zhao et al., 2016). Pour les applications médicales, les deux principaux avantages des technologies de fabrication additive par rapport aux autres procédés de mise en forme des structures poreuses sont les suivants :

- Contrôle locale et globale de chaque aspect morphologique de la structure poreuse;
- Mise en forme directe d’un implant de forme complexe s’adaptant aux besoins spécifiques du patient.

1.3.1 Métallurgie des poudres

Parmi les nombreux procédés impliquant la métallurgie des poudres, il est possible d’en mentionner quelques-uns.

Le frittage de poudres métalliques avec matériau espaceur (*space holder method* en anglais) se déroule en quatre étapes de fabrication (Figure 1.2). La première étape consiste à mélanger les particules métalliques et d’espaceurs. La deuxième étape consiste à compacter (de façon isostatique ou uniaxiale) le mélange poudres métalliques-espaceurs. Le produit résultant de cette compaction est appelé le produit vert et possède une certaine intégrité structurelle lui permettant d’être manipulé et usiné. La troisième étape consiste à traiter thermiquement le produit vert (à basse température) afin de retirer le matériau espaceur par pyrolyse. Le produit brun est alors obtenu. Enfin, la quatrième étape consiste à fritter le produit brun (la poudre compactée et vide d’espaceurs) à l’aide d’un traitement thermique à haute température (en deçà de la température de fusion du matériau). Il est alors possible d’assister à la consolidation des particules métalliques et à l’obtention d’une mousse métallique dont l’intégrité structurelle est maximale (Imwinkelried, 2007; Niu et al., 2009; Rivard et al., 2014; Wang et al., 2009). Ces dernières études ont d’ailleurs démontré la possibilité d’obtenir des mousses métalliques biocompatibles ayant des propriétés mécaniques similaires à celle des os humains tout en présentant une morphologie adéquate pour la croissance osseuse.

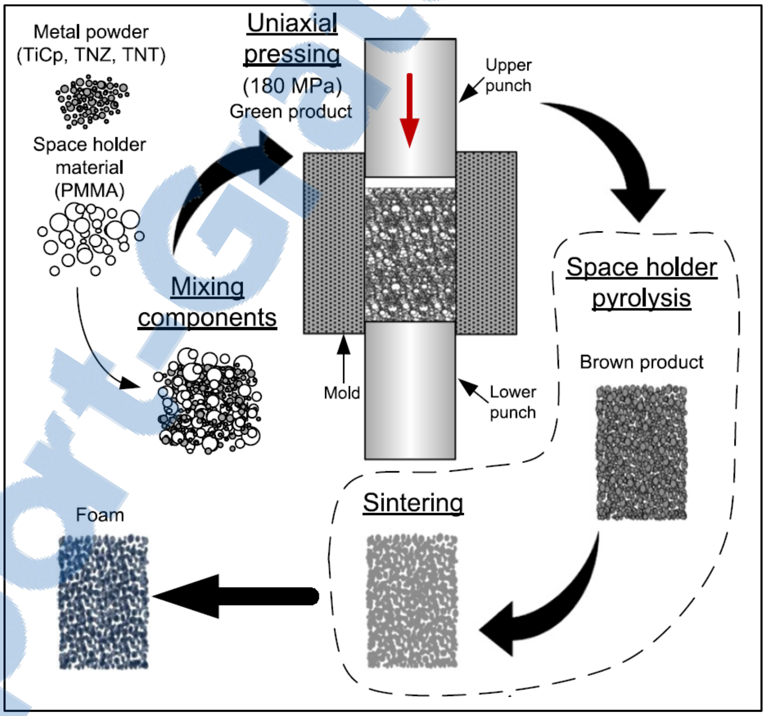

Figure 1.2 Schématisation du procédé de frittage de poudres métalliques avec matériau espaceur
Tirée de Rivard et al. (2014)

La synthèse par combustion (*combustion synthesis* en anglais) est particulièrement utilisée pour le développement d’alliage nickel-titane superélastique poreux même si les technologies de FA deviennent de plus en plus courantes (Elahinia et al., 2016). La consolidation des poudres suivant leur compaction est obtenue suite à une élévation locale de température produite par une décharge électrique, un faisceau laser ou dans un four menant à une forte réaction exothermique (Li et al., 2000; Li, Rong et Li, 2002) (Figure 1.3). Les propriétés intrinsèques des alliages superélastiques combinées à la morphologie des structures poreuses font que ce type de mousse métallique est particulièrement intéressant pour les applications médicales (Maîtrejean, Terriault et Brailovski, 2013b).

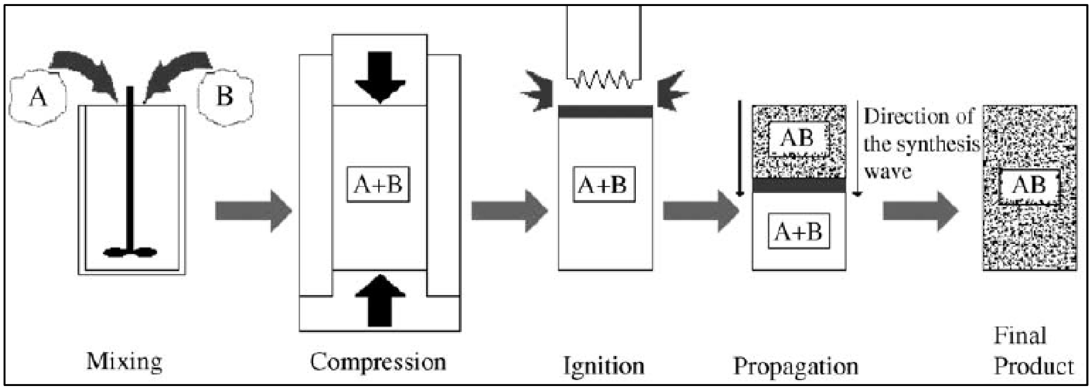

Figure 1.3 Schématisation du procédé de synthèse par combustion
Tirée de Ryan, Pandit et Apatsidis (2006)

Le frittage de poudre avec matériau espaceur, la synthèse par combustion et la majorité des autres procédés de mise en forme impliquant la métallurgie des poudres vont généralement mener à des structures poreuses possédant une morphologie aléatoire (ou stochastique). Toutefois, d'autres procédés restent disponibles pour produire des structures poreuses à morphologie ordonnée (ou régulière). Parmi ces derniers, il est possible de mentionner la technique de réplication utilisée par Ryan, Pandit et Apatsidis (2008). Ce procédé consiste, en premier lieu, à fabriquer le squelette d'une structure ordonnée à l'aide d'une imprimante 3D en utilisant de la cire. En deuxième lieu, le modèle de cire est plongé dans un mélange semi-liquide de poudre de titane et d'éthylène glycol. Après avoir retiré l'éthylène glycol (par capillarisation) et la cire (par chauffage à basse température), la structure de titane est frittée produisant ainsi une structure métallique poreuse possédant une morphologie ordonnée (Figure 1.4). Il est à noter que d'autres techniques de réplication pouvant mener à des structures poreuses à morphologie stochastique existent (Li et al., 2002).

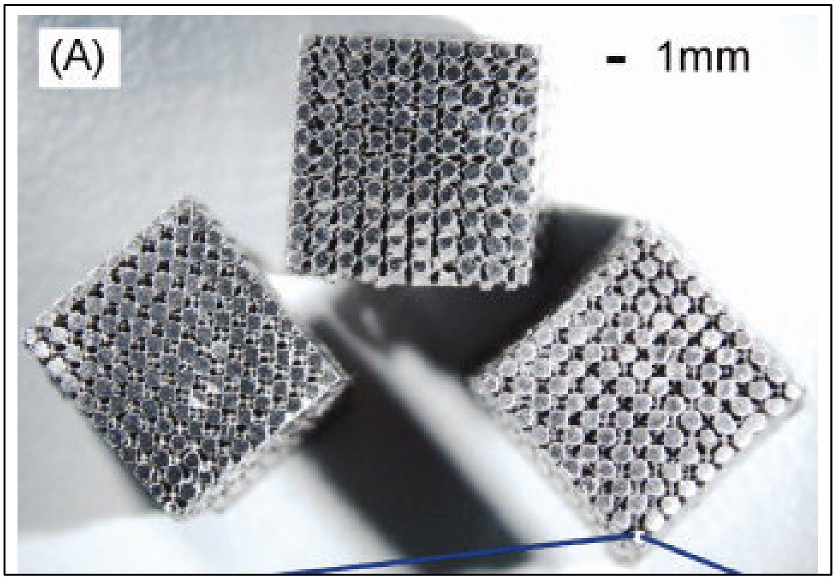

Figure 1.4 Structures poreuses en titane produites par une technique de réplication
Tirée de Ryan et al. (2009)

1.3.2 Fabrication additive métallique

L'organisme *ASTM International* propose une norme permettant de catégoriser l'ensemble des procédés de fabrication additive (FA) selon sept grandes familles (ASTM F2792-12a, 2015). La famille la plus répandue pour la fabrication additive de structure métallique poreuse est la fusion sélective sur lit de poudre (*powder bed fusion* en anglais) utilisant soit l'énergie d'un faisceau laser (*selective laser melting* ou SLM en anglais) ou d'un faisceau d'électrons (*electron beam melting* ou EBM en anglais) pour la fusion des poudres métalliques.

La fabrication typique d'une pièce par SLM est réalisée grâce à la fusion successive de couches composées de poudres métalliques et empilées les unes par-dessus les autres (Figure 1.5). Sur chacune de ces couches, la consolidation de certaines régions est réalisée en utilisant l'énergie thermique d'un faisceau laser contrôlé par un système de déflexion de miroirs. Les couches physiquement reproduites lors de la fabrication sont obtenues à partir d'un modèle numérique sectionné en plusieurs tranches et conçu à partir d'un logiciel de conception assistée par ordinateur (CAO). Il est à noter que dans le but d'éviter les risques de feu et d'explosion, la fusion des particules métalliques doit être réalisée sous une atmosphère inerte d'argon ou d'azote (pauvre en oxygène). Ceci permet également de minimiser l'oxydation des composants lors de leur fabrication. Les quatre principaux paramètres de fabrication de ce procédé sont la puissance du faisceau laser, la vitesse du faisceau laser, la distance entre deux parcours du faisceau et l'épaisseur des couches de poudre métallique (Kruth et al., 2005; Vandenbroucke et Kruth, 2007). Lorsque combinés, ces paramètres déterminent la densité d'énergie du faisceau laser.

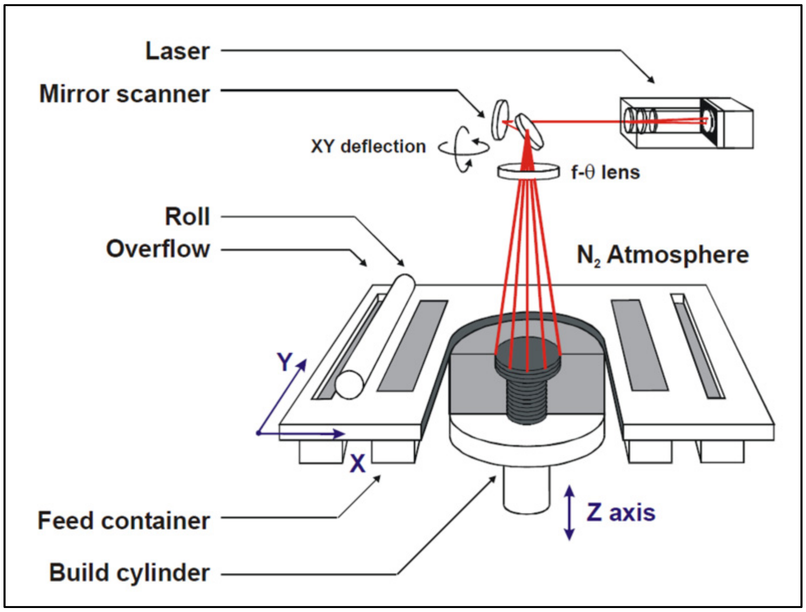

Figure 1.5 Schématisation du procédé de fusion sélective sur lit de poudre par faisceau laser
Tirée de Kruth et al. (2005)

Toutefois, en raison du fait que ces technologies n'ont pas encore atteint un niveau de maturité très élevé, certaines limitations d'ordre technologique doivent encore être réglées avant que ces procédés puissent être utilisés sans aucune contre-indication. Parmi ces limitations, il est possible de mentionner les suivantes :

- La difficulté de réaliser les très petites caractéristiques morphologiques des structures poreuses afin d'atteindre une taille de pore favorisant la croissance osseuse (50-800 µm) (Horn et al., 2014). Cette limitation est principalement liée à la taille des particules métalliques ainsi qu'au diamètre du faisceau laser utilisé pour la fusion des poudres.

- La présence de microporosité menant à la présence de concentrateurs de contrainte et pouvant donc affecter la vie en fatigue des structures poreuses (Hrabe et al., 2011). Le contrôle adéquat des paramètres de fabrication (la puissance du faisceau laser, la vitesse du faisceau laser, la distance entre deux parcours du faisceau et l'épaisseur des couches de poudre métallique) permet de minimiser la présence de micropores.
- La non-uniformité du fini de surface influencée par l'orientation des composants par rapport à la direction de fabrication (EOS GmbH Electro Optical Systems) et pouvant à son tour affecter la vie en fatigue des structures poreuses (Chan et al., 2013). Le post-traitement du fini de surface à l'aide de diverses techniques (polissage mécanique, électrochimique, mécano-chimique, etc.) permet d'uniformiser la rugosité de surface des composants.
- La nécessité d'inclure des structures de support qui peuvent être parfois difficiles à retirer. Il est à noter que cette problématique est associée au procédé SLM puisque le procédé EBM ne nécessite pas l'ajout de structures de support.
- La possible présence de poudre partiellement ou non fusionnée pouvant se retrouver au sein du corps humain et menant à une « réaction à corps étranger ». Les principales conséquences d'une telle réaction ont été discutées par Schmalzried, Jasty et Harris (1992) et Willert et Semlitsch (1977) et pourraient être évitées si des post-traitements adéquats de finis de surface étaient utilisés. Il est à noter que la porosité ouverte des mousses métalliques va faciliter l'enlèvement des particules métalliques indésirables.
- Enfin, l'anisotropie des propriétés mécaniques et la présence de contraintes résiduelles d'origine thermique causées par le refroidissement instantané et unidirectionnel des composants lors de la fusion des poudres sont parmi les autres problématiques inhérentes à la FA métallique (Frazier, 2014).

Même si elles sont nombreuses, ces limitations n'ont pas empêché la *U.S. Food and Drug Administration* (ou FDA) d'autoriser l'utilisation de plus de 85 dispositifs médicaux fabriqués additivement (métal et plastique confondu) (U.S. Food and Drug Administration, 2016). De plus, la FDA propose un guide intitulé *Technical Considerations for Additive Manufactured Devices* (version préliminaire en date du mois d'octobre 2016) afin d'orienter les gens de l'industrie lors du développement de dispositifs médicaux.

Enfin, il est à noter que mis à part la fusion sélective sur lit de poudre, le procédé de mise en forme LENS^{TM} (*Laser Engineered Net Shaping*) de la compagnie américaine Optomec faisant partie de la famille du dépôt de matière sous énergie concentrée (*directed energy deposition* ou DED en anglais) a également été utilisé pour la FA de structure métallique poreuse (Bandyopadhyay et al., 2008). Ce procédé reste toutefois marginal par rapport aux autres puisque peu de chercheurs ont réussi à atteindre des niveaux de porosité très élevés satisfaisant les exigences biomécaniques.

1.3.3 Discussion et outils utilisés

Pour la mise en forme des structures métalliques poreuses, les technologies de FA mettent de l'avant les aspects de personnalisation des implants puisque la porosité en tout point dans le volume de l'implant peut être contrôlée grâce à la création de gradients de porosité. Ce faisant, il est possible d'optimiser localement les propriétés mécaniques et morphologiques de la prothèse selon les besoins biomécaniques spécifiques du patient. C'est pour cette principale raison que la FA est adoptée dans le cadre de ce projet avant les procédés fondés sur la métallurgie des poudres. De plus, il est à noter que la FA offre la possibilité d'adapter la forme et la taille de l'implant à l'anatomie du patient.

Le procédé de fabrication additive de fusion sélective sur lit de poudre par faisceau laser est utilisé pour la fabrication des structures poreuses de ce projet. La fabrication est réalisée avec une machine *EOSINT M 280* (EOS GmbH, Munich, Allemagne) disponible à l'ÉTS. Deux types poudre biocompatibles fournis par EOS sont utilisés : *EOS Titanium Ti64* et *EOS CobaltChrome MP1*. Les paramètres de fabrication fournis par EOS sont employés. Le travail préparatoire pour la FA (traitement des fichiers STL, orientation des échantillons par rapport à la plateforme de fabrication et génération des structures de support) est réalisé à l'aide du logiciel *MAGICS 17.02 Support Generation Module* (Materialise, Louvain, Belgique). Tous les échantillons fabriqués par la machine *EOSINT M 280* sont traités thermiquement afin d'éliminer les contraintes résiduelles thermiques et d'homogénéiser les propriétés mécaniques. Tous les traitements thermiques sont réalisés dans un four *N41/H* (Nabertherm GmbH, Lilienthal, Allemagne) sous une atmosphère d'argon. Les temps et températures de maintien fournis par EOS sont employés.

1.4 Caractérisation des structures poreuses

Cette section se concentre sur la caractérisation des propriétés morphologiques et mécaniques des structures poreuses et les principales références à consulter sont les suivantes : Ashby et al. (2000), Banhart (2001), Gibson et Ashby (1999) et Rouquerol et al. (1994). Il est à noter que même si la caractérisation des propriétés biochimiques reste essentielle pour l'utilisation des structures métalliques poreuses pour applications médicales, cet aspect n'est pas discuté ici puisqu'il n'est pas abordé dans cette thèse.

1.4.1 Propriétés morphologiques

En premier lieu, la morphologie des structures poreuses peut être classifiée en deux familles, soit les structures poreuses ordonnées (régulières) et stochastiques (aléatoires). Le choix d'une ou l'autre des familles va avoir une influence significative sur les caractéristiques morphologiques et mécaniques.

Les métriques à considérer lors de la caractérisation de la morphologie des structures poreuses sont nombreuses, mais les principales sont la porosité, la taille, la forme et la distribution des pores, la surface spécifique et la perméabilité. Plusieurs méthodes destructives et non destructives peuvent être employées pour la caractérisation des différents aspects morphologiques des mousses métalliques (Banhart, 2001; Rouquerol et al., 1994).

La porosité peut être mesurée à l'aide d'une simple pesée à sec si le volume apparent de l'échantillon est connu. Sinon, des méthodes standardisées fondées sur le principe d’Archimède peuvent également être utilisées (ASTM B962-15, 2015; ASTM C20-00, 2015). Même si elle n’est pas directement destinée pour les mousses métalliques, la norme ASTM C20-00 (2015) est particulièrement intéressante puisqu’elle permet de caractériser en partie l’interconnectivité des pores en fournissant des données sur la porosité ouverte et fermée d’un échantillon.

Les méthodes d’analyse d’image comme la stéréologie sont couramment utilisées pour caractériser la taille, la forme et la distribution des pores ainsi que la surface spécifique des structures poreuses (Abell, Willis et Lange, 1999; Rivard et al., 2014). La fonction *Analyze Particles* du logiciel ImageJ (Rasband) spécialisé en analyse d’image ou la fonction *Regionprops* du *Image Processing Toolbox* de MATLAB permettent d’effectuer de telles analyses à partir d’une coupe transversale binarisée d’une structure poreuse (voir la Figure 1.6 pour une métallographie typique d’une mousse de titane observée par microscopie optique). Il est à noter que la porosimétrie par intrusion de mercure peut également être utilisée pour mesurer la taille, la forme et la distribution des pores (Rivard et al., 2014) ainsi que la perméabilité (Zhiye et Qinhong, 2013) des structures poreuses.

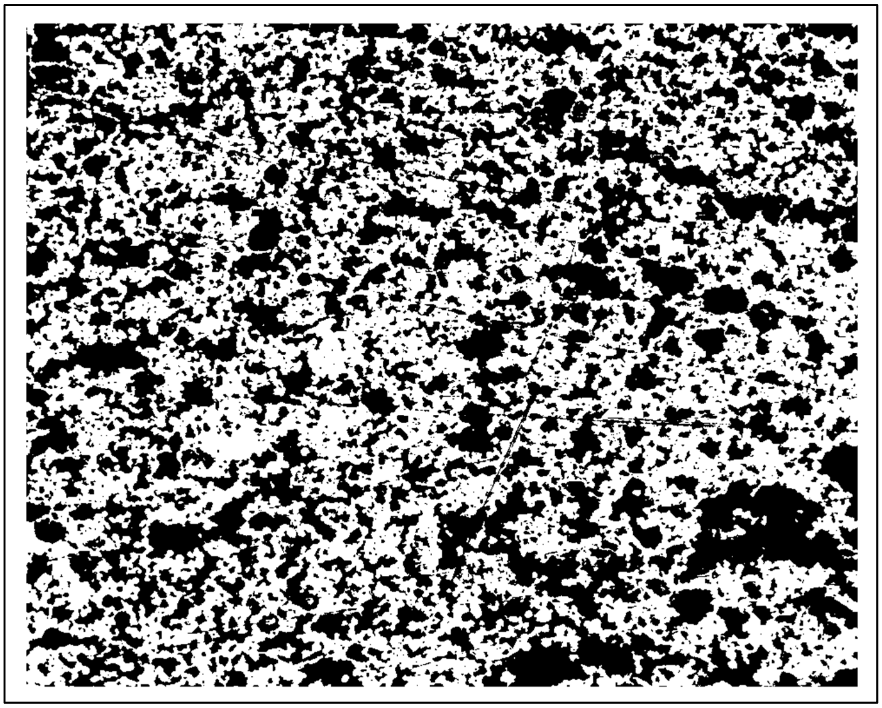

Figure 1.6 Métallographie d’une mousse de titane pouvant être utilisée pour l’analyse de la taille, forme et distribution des pores (la matière est blanche et les pores sont noirs)

La microtomographie par rayons X est une méthode de caractérisation fondée sur la reconstruction d’un modèle 3D à partir d’une série d’acquisitions d’images 2D d’un échantillon. En plus d’être non-destructive, la microtomographie par rayons X permet de caractériser la majorité des métriques morphologiques autrement obtenues à l’aide des méthodes précédemment discutées (Ho et Hutmacher, 2006; Maire et al., 2007). Plusieurs logiciels commerciaux sont également disponibles pour le traitement des résultats et parmi ces derniers, il est possible de mentionner le *Foam structure analysis module* de VGStudio Max 3.0 de la compagnie allemande Volume Graphics (Figure 1.7). Ce module fournit une grande quantité d’informations morphologiques spécifiques aux structures poreuses (Volume Graphics, 2016). Un inconvénient relié à cette méthode est le coût d’acquisition d’un tel équipement incluant les logiciels de post-traitement.

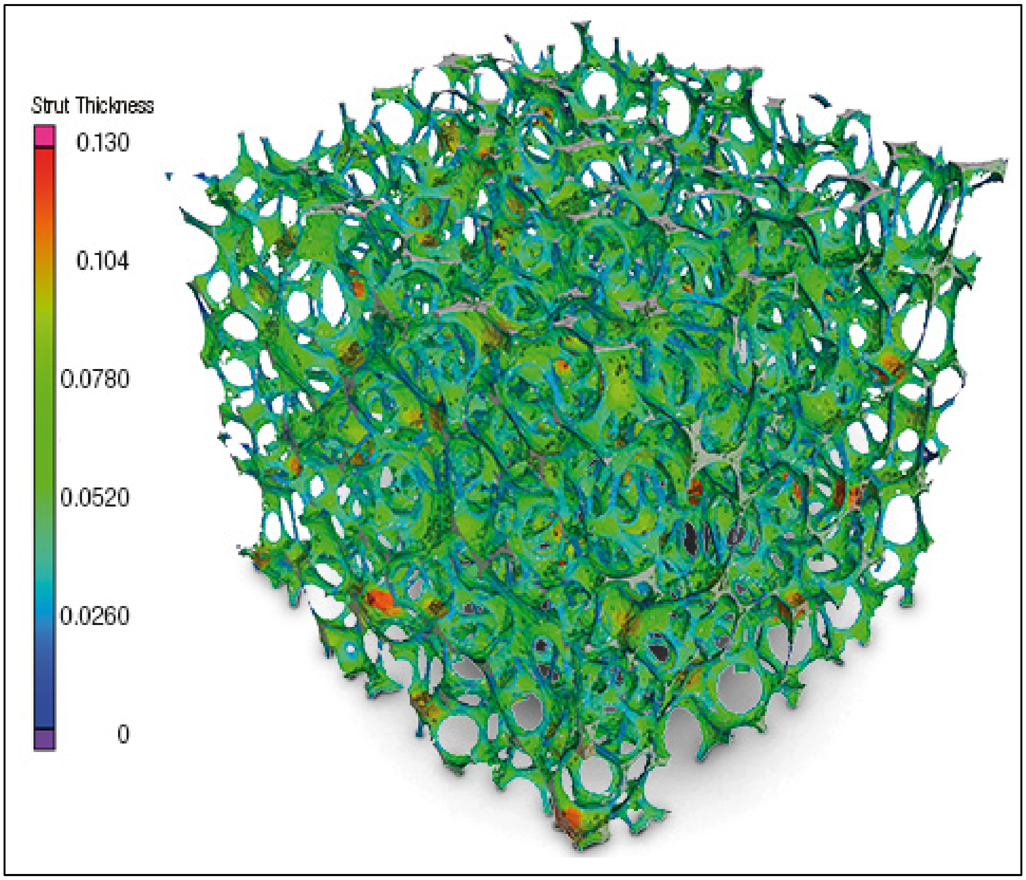

Figure 1.7 Exemple d'analyse de l'épaisseur des membrures d'une mousse par le Foam structure analysis module de VGStudio Max 3.0
Tirée de Volume Graphics (2016)

1.4.2 Propriétés mécaniques

La caractérisation des propriétés mécaniques des mousses s'effectue généralement au niveau du comportement global ou apparent de ces dernières plutôt à l'échelle locale des pores. L'analyse du comportement mécanique à l'échelle des pores est plutôt faite afin de pouvoir interpréter les résultats à l'échelle globale (c'est-à-dire, l'identification des modes de déformation et de rupture).

Les deux principales métriques à considérer lors de la caractérisation des propriétés mécaniques des structures poreuses pour applications médicales sont le module de Young et la contrainte d'écoulement. La caractérisation de ces deux métriques est identique en tension et en compression. Toutefois, au-delà de la limite élastique, le comportement en compression de la mousse est caractérisé par un plateau où la contrainte reste relativement constante suivi d'une phase de densification où la contrainte augmente rapidement. En tension, les modes de déformation et de rupture sont différents de ceux en compression puisqu'ils dépendent fortement de la morphologie et du matériau constituant la structure poreuse (Gibson et Ashby, 1999).

Tandis que plusieurs méthodes normalisées (ASTM) existent pour la caractérisation du comportement mécanique de composants possédant un revêtement poreux, Banhart (2001) mentionne que les méthodes de caractérisation des structures poreuses ne diffèrent pas beaucoup de celles utilisées pour les matériaux denses. Il est cependant nécessaire de contrôler adéquatement la représentativité statistique des résultats. En effet, en raison de l'hétérogénéité de la morphologie des mousses, une grande quantité d'échantillons est parfois requise afin d'avoir des résultats significatifs (Banhart, 2001; Davis et al., 2001). Toutefois, afin de diminuer l'influence de ce facteur sur les résultats, il est possible de suivre certaines recommandations. Par exemple, Ashby et al. (2000) mentionne que lors d'un essai de tension ou compression, les dimensions de la section utile de l'échantillon devraient être égales à au moins sept fois la taille d'un pore afin d'éviter des effets de bord. En d'autres mots, il est important que la section utile de l'échantillon soit morphologiquement représentative de la structure poreuse afin de démontrer un comportement mécaniquement représentatif.

L'étude du comportement local (à l'échelle des pores) des structures poreuses peut être réalisée avec succès à l'aide de plusieurs techniques comme la corrélation d'images numériques (Brenne, Niendorf et Maier, 2013; Zhang et Arola, 2004) et la microtomographie par rayons X (Maire et al., 2003; Petit et al., 2016). La première méthode permet d'avoir une information à la surface de la structure, alors que la seconde analyse le comportement mécanique de la structure poreuse dans son intégralité. Ces deux méthodes permettent donc d'analyser les mécanismes de déformation et de rupture au cours du chargement.

1.4.3 Discussion et outils utilisés

Dans le cadre de ce projet, les efforts de recherche se concentreront autour des structures poreuses stochastiques plutôt que régulières en raison du fait que la morphologie de l'os s'apparente davantage à une structure poreuse stochastique (Figure 1.1). Ce choix est également fondé sur le fait que les structures poreuses stochastiques sont plus propices à présenter un comportement mécanique isotrope contrairement à certains types de structure poreuse ordonnée fortement anisotropes.

Deux méthodes sont utilisées pour caractériser la morphologie des structures poreuses : 1) la la taille, forme et distribution des pores sont obtenues à l'aide de la stéréologie en utilisant la fonction *Regionprops* du *Image Processing Toolbox* de *MATLAB 2013b* et 2) la microtomographie par rayons X est utilisée pour obtenir un modèle 3D complet des structures poreuses. Ce modèle permet notamment d'évaluer l'aspect général de la morphologie, le niveau de porosité et la présence de poudre partiellement ou non fusionnée. De plus, des coupes transversales sont effectuées sur les modèles 3D des mousses en vue de l'analyse stéréologique.

La ductilité sous tension des structures poreuses est très basse lorsqu'elle est comparée à celle d'un essai de compression ou encore à la ductilité sous tension du matériau dense constituant la structure poreuse (Ronan, Deshpande et Fleck, 2016). Ce faisant, même si la majorité des ouvrages retrouvés dans la littérature sont fondés sur des essais de compression, l'étude du comportement en tension reste essentielle puisque les structures poreuses sont appelées à subir des chargements multiaxiaux lorsqu'elles seront utilisées pour la conception de prothèse. C'est pour cette raison que, dans le cadre de ce projet, les propriétés mécaniques des structures poreuses sont caractérisées à l'aide d'essais de traction réalisés avec une machine de traction MTS 810 équipée d'une cellule de charge de 500 kN (MTS Systems Corporation, Eden Prairie, MN, É.-U.)

La caractérisation du comportement mécanique des tiges fémorales est fondée sur la norme ISO 7206-4 (2010) utilisée pour déterminer les propriétés d'endurance et les performances des tiges fémorales. Ces conditions normalisées de chargement sont représentatives d’un cycle de marche avec une attaque du talon (Chanda et al., 2015). Cependant, il est à noter que dans le cadre du projet, des essais statiques sont réalisés.

Enfin, il est à noter que durant tous des essais mécaniques, un système de mesure par corrélation d’images numériques (*ARAMIS 5M*, GOM mbH, Brunswick, Allemagne) est couplé à la machine de traction afin de mesurer localement et globalement les champs de déplacement et déformation des échantillons au cours de leur chargement.

1.5 Modélisation des structures poreuses

1.5.1 Approche de modélisation multiéchelle

Dans le domaine de la science des matériaux où les méthodes d’analyses numériques sont très répandues, Elliott (2011) mentionne que certains problèmes sont intrinsèquement difficiles à conceptualiser au sein d’un seul modèle dû au fait que ce dernier concerne parfois plusieurs échelles de grandeur différentes. Pour pallier à cette problématique, de Pablo et Curtin (2007), Elliott (2011) et bien d’autres proposent d’employer une approche de modélisation multiéchelle. Ce principe énonce qu’afin de pleinement comprendre le comportement d’un matériau donné, il est nécessaire de l’étudier à différents ordres de grandeur devant être cohérents entre eux (de Pablo et Curtin, 2007).

L’approche de modélisation multiéchelle a été utilisée dans plusieurs domaines de recherche comme les matériaux composites (Belsky et al., 1995; Muliana et Haj-Ali, 2005; Rozicka et al., 2011). Cette approche a également été adoptée pour l’étude des structures poreuses (Daxner, 2002; Maîtrejean, Terriault et Brailovski, 2013b; Mangipudi et Onck, 2011) en raison du fait que les dimensions d’un pore par rapport aux dimensions apparentes de la mousse diffèrent de plusieurs ordres de grandeur. La modélisation multiéchelle du comportement mécanique d’une mousse métallique est généralement composée de trois échelles soit macro-, méso- et microscopique (voir la Figure 1.8). La méthode des éléments finis est généralement l'approche numérique retenue pour la réalisation de telles simulations.

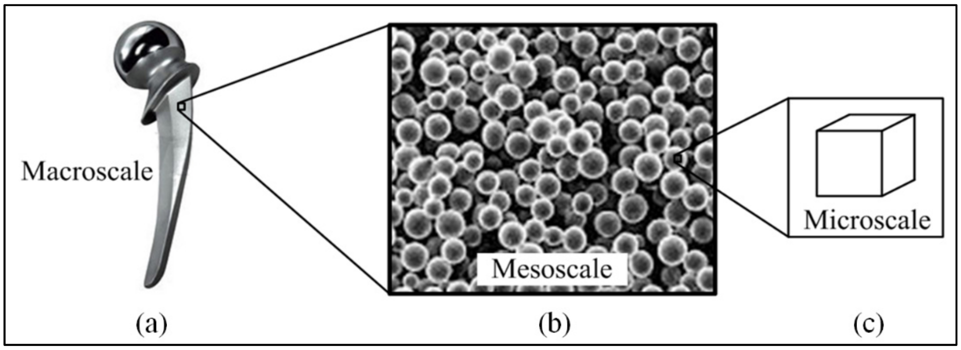

Figure 1.8 Schématisation de l'approche de modélisation multiéchelle
Tirée et adaptée de Terriault, Maîtrejean et Brailovski (2013)

Le modèle macroscopique (Figure 1.8a) est employé pour simuler le comportement global de l'implant. Toutefois, dans le but d'éviter la représentation explicite de la porosité à cette échelle de grandeur, l'implant est plutôt modélisé à partir d'un matériau dense possédant des propriétés de matériaux fictives, mais équivalentes à celles du matériau poreux. Ces propriétés mécaniques sont déterminées à l'échelle mésoscopique (mais peuvent aussi être déterminées de façon expérimentale, analytique ou numérique).

L'un des principaux défis concernant le développement de l'approche de modélisation multiéchelle pour les structures poreuses réside au niveau du modèle mésoscopique. En effet, selon Shahbeyk (2013), le modèle mésoscopique (Figure 1.8b) se doit d'être à la fois réaliste et représentatif en plus d'allouer la possibilité de simuler différents comportements mécaniques des mousses métalliques : il est alors question d'un volume élémentaire représentatif (*representative volume element* ou RVE en anglais). Il est aussi impératif que ce modèle soit également morphologiquement représentatif. Ce faisant, la morphologie de la structure poreuse est explicitement modélisée à cette échelle.

Enfin, chaque élément de matière composant le modèle mésoscopique obéit au modèle microscopique (Figure 1.8c) dans lequel est implémentée une relation constitutive décrivant le comportement mécanique du matériau constituant la mousse métallique à son état dense. Dans le cas où seulement le comportement élastique de la mousse est recherché, une loi de comportement élastique linéaire est utilisée. La théorie classique de la plasticité est la plus fréquemment utilisée s'il est visé de décrire l'endommagement des mousses métalliques (Yu, 2002). À cet effet, les lois de comportement élastoplastique sont très répandues (Jang, Kyriakides et Kraynik, 2010; Kwon, Cooke et Park, 2003; Michailidis et al., 2008; Ryan et al., 2009; Shen et Brinson, 2006).

1.5.2 Relations de mise à l'échelle

La technique par excellence permettant de faire le pont entre les trois échelles de modélisation a été proposée par Gibson et Ashby (1999). Cette approche utilise des relations de mise à l'échelle (*scaling relation* en anglais) fondée sur des lois de puissance : voir l'équation (1.1) où P est la propriété équivalente du matériau fictif à employer à l'échelle *macroscopique* et à caractériser à l'échelle *mésoscopique*, P_S est la même propriété du matériau à son état dense et est à utiliser à l'échelle *microscopique*, ρ et ρ_S sont respectivement la masse volumique du matériau dense et poreux et C et n sont les coefficients de la loi de puissance à déterminer. Dans cette dernière équation, le rapport ρ/ρ_S (*relative density* en anglais) correspond à l'inverse de la porosité.

$$\frac{P}{P_S} = C\left(\frac{\rho}{\rho_S}\right)^n \tag{1.1}$$

Afin de déterminer les coefficients C et n, plusieurs analyses expérimentales, analytiques ou numériques à l'échelle mésoscopique sont d'abord effectuées sur des structures poreuses possédant différents niveaux de porosité afin d'obtenir les propriétés de matériau P pour chacune de ces porosités. Des fonctions mathématiques d'ajustement de courbe (*curve fitting* en anglais) sont ensuite utilisées pour déduire les coefficients C et n de la loi de puissance qui s'adapte le mieux aux résultats. Suivant cette étape, les relations de mise à l'échelle peuvent être utilisées pour déterminer les propriétés apparentes du matériau poreux à utiliser au niveau du modèle macroscopique.

1.5.3 Génération de la morphologie des structures poreuses

À l’échelle mésoscopique, il est impératif de pouvoir générer explicitement la morphologie des structures poreuses. Les différentes approches de modélisation disponibles pour représenter la morphologie des structures poreuses sont divisées en deux classes, soit une classe pour les structures poreuses ordonnées et une autre pour les structures stochastiques.

Les approches utilisées pour la génération de la morphologie des structures poreuses ordonnées sont fondées sur la répétition de structures ou cellules unitaires (*unit cell* en anglais). À titre d’exemple, il est possible de mentionner le tétrakaidécaèdre de la Figure 1.9, soit un polyèdre composé de 6 faces cubiques et 8 faces hexagonales (Jang, Kyriakides et Kraynik, 2010; Maîtrejean et al., 2014; Takahashi, Okumura et Ohno, 2010).

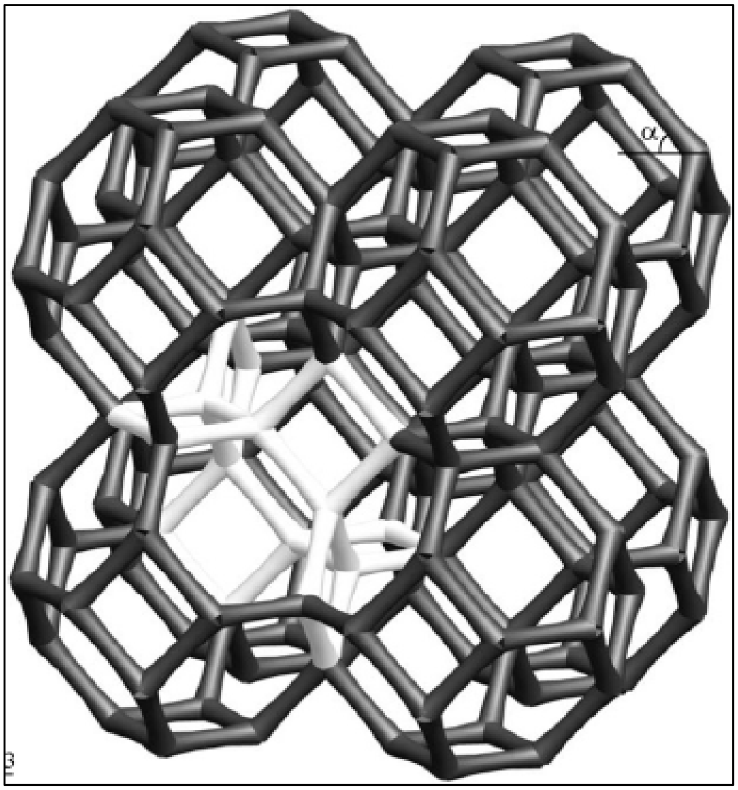

Figure 1.9 Structure poreuse ordonnée fondée sur la répétition de cellules unitaires de tétrakaidécaèdre
Tirée de Jang, Kyriakides et Kraynik (2010)

Les approches utilisées pour la génération de la morphologie des structures poreuses stochastique sont très variées (Brailovski et Terriault, 2016). Parmi celles-ci, il est possible de mentionner la désorganisation de structures ordonnées (Mullen et al., 2010), les diagrammes de Voronoi (Sotomayor et Tippur, 2014; Tang et al., 2014), la reconstruction à partir d'une série d'images obtenues par métallographies (Shen et al., 2006) ou par microtomographie par rayons X (Maire et al., 2006; Michailidis et al., 2008), la création successive et aléatoire de voxels (DeGiorgi et Qidqai, 2002; Maîtrejean, Terriault et Brailovski, 2013b; Panico et Brinson, 2008), etc. Il est à noter qu'un voxel (contraction de *volumetric pixel* en anglais) est un pixel en trois dimensions.

Il est à noter que les structures générées à l'aide de ces diverses méthodes stochastiques doivent posséder une taille suffisamment grande pour être mécaniquement et morphologiquement représentative des mousses métalliques malgré la nature aléatoire de leur géométrie et suffisamment petite pour ne pas être trop pénalisante au point de vue des simulations numériques.

1.5.4 Discussion et outils utilisés

Dans le cadre de ce projet, une démarche de modélisation multiéchelle fondée sur la méthode des éléments finis, l'approche du volume élémentaire représentatif et les relations de mise à l'échelle est utilisée. Cette approche de modélisation est inévitable puisqu'il est numériquement impraticable de simuler le comportement mécanique de structure poreuse aux échelles macro-, méso- et microscopique simultanément en raison des temps de calcul très élevés et de la grande taille des modèles.

L'environnement *ANSYS Mechanical APDL 15.0* (ANSYS, Canonsburg, PA, É.-U.) est utilisé pour la réalisation de toutes les analyses par éléments finis. Il est à noter que certaines simulations sont réalisées sur le superordinateur *Guillimin* de l'Université McGill (Montréal, Canada) plutôt que sur un ordinateur de bureau. En effet, la grande quantité de mémoire vive, la parallélisation des calculs sur plusieurs processeurs et l'accessibilité des ressources du superordinateur permettent l'accélération des analyses numériques.

Afin de générer la morphologie stochastique des structures poreuses à porosité ouverte, un algorithme de génération fondée sur la création successive et aléatoire de voxels est développé dans l'environnement *MATLAB 2013b* (MathWorks, Natick, MA, É.-U.). Il est à noter que cet algorithme a été en partie développé dans des travaux de recherche antérieurs (Maîtrejean, Terriault et Brailovski, 2013b). Cet algorithme constitue la base de ce projet puisque les structures poreuses découlant de l'algorithme seront analysées numériquement, fabriquées additivement, et caractérisées du point de vue des propriétés morphologiques et mécaniques. Il est à noter que les modèles numériques des structures poreuses peuvent être transférés en fichier STL pour leur fabrication additive ou discrétisés en maillage éléments finis pour leur analyse numérique.

CHAPITRE 2

MODELING OF METALLIC FOAM MORPHOLOGY USING THE REPRESENTATIVE VOLUME ELEMENT APPROACH: DEVELOPMENT AND EXPERIMENTAL VALIDATION

Charles Simoneau, Patrick Terriault, Jonathan Rivard, Vladimir Brailovski

Département de génie mécanique, École de technologie supérieure,
1100, rue Notre-Dame Ouest, Montréal, Québec, Canada H3C 1K3

Article publié dans la revue « International Journal of Solids and Structures »,
vol. 51, n° 21-22, p. 3633-3641, octobre 2014

2.1 Avant-propos

La première étape de ce projet consiste à modéliser et caractériser la morphologie de structures poreuses. Ceci est accompli au moyen d'un algorithme de génération développé dans l'environnement MATLAB 2013 et d'une technique d'analyse d'image, soit la stéréologie. Suite à la validation expérimentale des résultats, l'algorithme de génération ainsi que les propriétés morphologiques des structures poreuses pourront être utilisés pour la suite du projet.

2.2 Résumé

Un algorithme est développé pour la génération de la morphologie de structures poreuses. L'algorithme utilise l'approche du volume élémentaire représentatif afin de s'assurer que les structures poreuses soient morphologiquement représentatives. La taille, la forme et la distribution des pores contenus dans la mousse sont déterminées à l'aide de la stéréologie, une méthode de caractérisation fondée sur l'analyse d'image de coupes transversales de mousses. Pour plusieurs niveaux de porosité, le plus petit volume élémentaire représentatif est numériquement déterminé en effectuant une analyse de convergence des métriques morphologiques (taille, forme et distribution des pores). La validation expérimentale de l'algorithme de génération morphologique est effectuée en comparant la morphologie des

mousses numériques à celle de mousses de titane produites à l’aide du frittage de poudre avec matériau espaceur.

2.3 Abstract

This paper focuses on the development of an algorithm capable of generating morphologically-representative foam structures using the Representative Volume Element (RVE) approach. Stereology, a sampling method based on direct observations of the foam cross-sections, is used to characterize the pore size and shape distributions. Using the morphology generation algorithm, the smallest RVEs corresponding to the numerically-convergent foam morphologies are calculated for different foam porosities. To validate the foam generation algorithm, the pore size and shape distributions of the numerically-generated foams are compared to those of the titanium foams manufactured by the space holder method.

2.4 Introduction

In orthopedics, the use of conventional, essentially bulk, metallic implants to replace damaged bones and worn articulations presents a well-known drawback caused by the substantial difference between the stiffness of an implant and that of bone. This difference, called stress-shielding, means that the loads become almost entirely supported by the implant, thus leaving bone tissues unloaded. This pathological change in stress distribution within the bone tissues provokes bone-resorption around the implant (Huiskes et al., 1987) and may eventually lead to loss of the bone-implant union, aseptic loosening of the implant, or bone fracture.

To address the stress-shielding problem, one solution is to use porous superelastic structures instead of conventional bulk materials (Bansiddhi et al., 2008; Zhao et Taya, 2006). Indeed, due to open-cell porous morphology and superelasticity, such an implant will ensure firm fixation through bone ingrowth while mimicking the mechanical behavior of bone (Brailovski et al., 2011). In other words, by adequately controlling the pore volume fraction (PVF), implant osseointegration ability and stiffness can be optimized.

To simulate the mechanical behavior of an entire device made of porous superelastic metal, we use the multiscale approach with three modeling scales. A macroscale model (Figure 2.1a) simulates the implant's response at a global level; it represents a bulk component with fictive material properties equivalent to those of the porous material. These equivalent properties are calculated using a mesoscale model (Figure 2.1b) that explicitly represents the morphology of the porous material. Finally, each element of the mesoscale model is driven by a microscale model (Figure 2.1c) which implements the constitutive relations of the bulk superelastic material (Terriault et Brailovski, 2013).

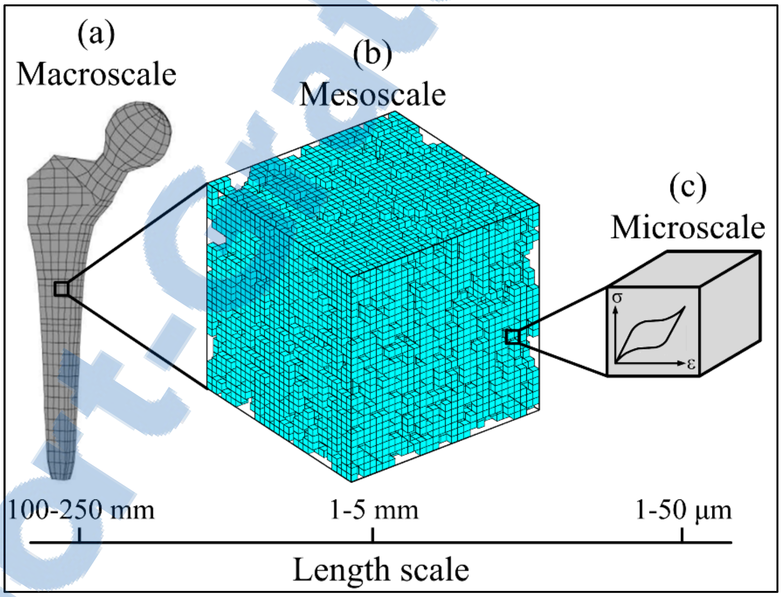

Figure 2.1 Schematization of the multiscale modeling approach for superelastic metallic implants

One of the main challenges in implementing the multiscale modeling approach is the development of a numerically efficient and morphologically-representative mesoscale model (Shahbeyk, 2013). On one hand, micromechanical averaging techniques (Nemat-Nasser et al., 2005) and the Unit Cell finite element approach (Qidwai et al., 2001) are limited to low-porosity or regular cellular structures. On the other hand, the Representative Volume Element (RVE) approach seems to be promising, provided that particular care is paid to the size of the RVE, since the length scale of an individual pore and that of an entire implant differs by several orders of magnitude (Maîtrejean, Terriault et Brailovski, 2013a).

To preserve the morphological features of the studied porous materials, Michailidis et al. (2010) and Shen et al. (2006) developed RVE models based on the 3D reconstruction of the metallic foam architecture from a series of 2D metallographic cross-sections. Shen et al. (2006) note that such an approach represents a valuable alternative to X-ray tomography, as shown in Maire et al. (2007) and Singh et al. (2010b), where the 3D foam morphology is directly measured. However, in all of these cases the RVEs were created based on the experimentally-produced foams of a given porosity.

Similarly to what was attempted by Panico et Brinson (2008) and Maîtrejean, Terriault et Brailovski (2013b) developed an original foam generation algorithm capable of numerically and randomly creating foams with different target pore volume fractions (PVFs). In that work, RVEs generated by this algorithm were composed of interconnected matter voxels (or volumetric pixels) contained within a cubic domain (see the mesoscale model of Figure 2.1b). To decrease the computation time of finite element simulations, the smallest possible size of the RVE capable of exhibiting suitable (or representative) mechanical behavior was targeted. However, even though the overall mechanical behavior of the RVEs generated by this algorithm has been partially validated, the role of the foam morphology (pore size, shape and distribution) has not yet been evaluated. The absence of this validation represents a major limitation, since the mechanical strength and the biological functionality of porous metals are strongly influenced by their morphology (Ho et Hutmacher, 2006).

Consequently, the main objective of this work is to create and validate an RVE-based algorithm capable of generating morphologically-representative foams. A morphological analysis is performed on the RVEs generated by this algorithm for the target open-cell porosities ranging from 0.05 to 0.95. Based on the results obtained, efforts are made to calculate the minimum RVE size capable of adequately representing the pore morphology for the whole range of the studied porosity. Finally, the proposed foam generation algorithm is validated experimentally, and its advantages and limitations are discussed.

2.5 Characterization of the foam morphology (metrics)

Several methods are available to characterize foam morphology (Banhart, 2001; Ho et Hutmacher, 2006; Matějíček et al., 2006; Rouquerol et al., 1994). The method employed in this work, stereology, is based on direct observations of the foam cross-sections. Stereology has often been used in studies involving metallic foams for medical applications (Ho et Hutmacher, 2006; Marshall et Ratner, 2005; Niu et al., 2009). Rouquerol et al. (1994) have established two practical requirements for using stereology: (1) plane cross-sections with clear contrast between matter and pores must be prepared prior to optical microscopy, and (2) a sufficient number of micrograph cross-sections must be collected in order to produce representative results.

In this work, prior to optical microscopy, the samples were prepared according to the following procedure. Firstly, the foams were sectioned, incorporated into bakelite and ground with abrasive paper to open the surface pores (240, 320, 400, 600 and 800 grit). Then, an epoxy resin (ULTRATHINTM 2, Pace technologies, AZ, USA) was pumped through the sample. Finally, the samples were ground again with abrasive paper (240, 320, 400, 600 and 800 grit) followed by polishing using 6 and 1 μm polycrystalline diamond solutions.

The use of epoxy resin (Banhart, 2001) has two main advantages: it prevents small pores from closing and bigger pores from being deformed during subsequent operations and also prevents the light from penetrating thought the sample during the optical microscopy. In other words, the risk to observe metal struts that are still in the microscope depth of field (but not on the plane cross-section) and that could cause a possible bias in the pore size measurement is avoided.

Direct observations of the foam cross-sections are taken by a Leica DM Light Microscope and are subsequently analyzed using either the “Analyse Particles” function of ImageJ (Rasband), a software dedicated to image analysis, or the built-in MATLAB function “RegionProps” (MathWorks, Natick, MA, USA). Prior to the analysis, each image must be binarized (black and white) to clearly distinguish pores filled with resin from metal struts. Both the ImageJ and MATLAB calculations lead to identical results and allow evaluation of the following geometrical parameters of each pore, using pixel-based units: the section (S), the perimeter (P) and the best-fit ellipse's major (M_a) and minor (M_i) axes. The best-fit ellipse corresponds to an ellipse that has the same area, orientation and centroid as the pore (Rasband).

Figure 2.2 illustrates a typical image analysis procedure: Figure 2.2a presents a binarized optical micrograph of 0.39-porosity Ti foam, while Figure 2.2b corresponds to the enlargement up to pixel dimensions of a square zone containing six pores (white) surrounded by matter (black). Figure 2.2c contains the best-fit ellipses for each pore (M_a and M_i of pore #5 are identified). Conversion of pixel to length unit is given by the microscope resolution (1280 × 1080 pixels) and enlargement (25X): in this case 1 pixel width equals 3.49 µm.

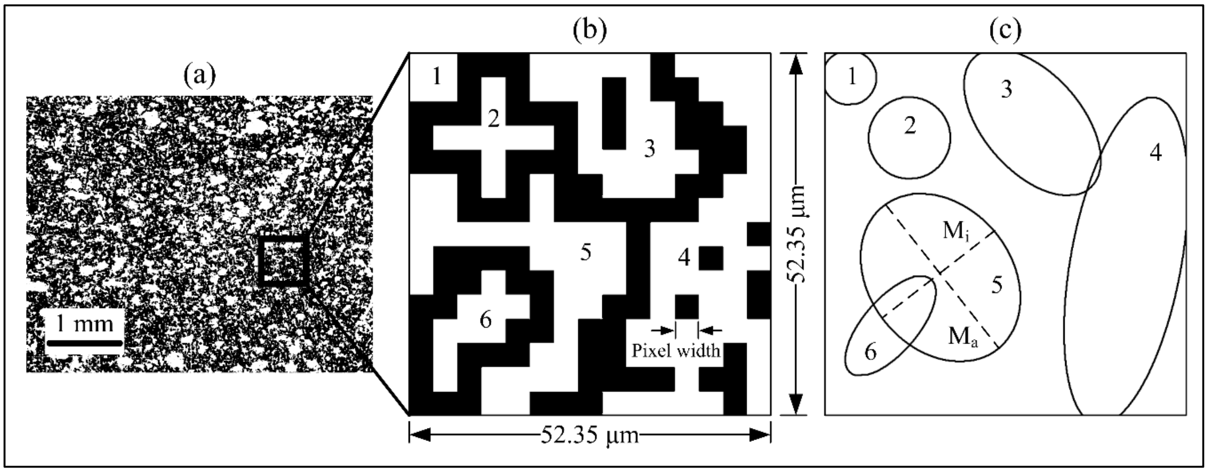

Figure 2.2 (a) Binarized optical micrograph of a Ti foam cross-section (PVF = 0.39) at 25X, (b) enlarged cross-section up to pixel size, and (c) best-fit ellipses for each pore of the enlarged cross-section

Once the images are analyzed, the equivalent projection area of a circle, or equivalent diameter (d), circularity (c) and roundness (r) are calculated for each pore following Eqs. (2.1), (2.2) and (2.3) (Rasband):

$$d = \sqrt{\frac{4S}{\pi}} \tag{2.1}$$

$$c = \frac{4\pi S}{P^2} \tag{2.2}$$

$$r = \frac{M_i}{M_a} \tag{2.3}$$

The circularity ($0 < c < 1$) indicates how close the shape of a pore comes to that of a circle, whereas the roundness ($0 < r < 1$) is the inverse of the aspect ratio commonly employed in finite elements (FE) analysis for the FE shape assessment (ANSYS ®, 2011). To illustrate a distinction between circularity and roundness, note that the circularity of pores #1 and #2 are $c = 0.78$ and 0.28, respectively, while their roundness are both $r = 1$ (Figure 2.2c).

By applying the described procedure to every pore of a cross-section, the distributions of the pore equivalent diameter, circularity and roundness can be obtained. Note that, generally, the pore equivalent diameter distribution refers to the total area occupied by the pores on an optical micrograph; therefore, its cumulative value always corresponds to 100%, irrespective of the global pore surface area fraction (Brailovski et al., 2011).

From these results, it is now possible to extract the following six metrics that characterize foam morphology:

- The pore equivalent diameters (size) and their distributions: d_{10}, d_{50} and d_{90} correspond to the equivalent diameters of pores, which occupy respectively up to 10%, 50% and 90% of the total pores' surface area;
- The circularity and roundness and their distributions, c_{50} and r_{50}, correspond respectively to the mean circularity and roundness of the d_{50} pores;
- The total number of pores, N_p.

Finally, it has to be mentioned that the procedure described above, which quantifies the foam morphology using image analysis of 2D-cross sections, is applied in this work for both the experimentally-obtained and the numerically-generated foams.

2.6 Modeling the foam morphology

2.6.1 The modeling algorithm

To generate a foam structure, the proposed algorithm requires two input parameters: the size of the Representative Volume Element (S_{RVE}) and the pore volume fraction (PVF_{in}). Depending on the value of the PVF_{in}, the algorithm takes one of two alternative routes to generate open-cell interconnected foams.

If $1 > PVF_{in} \geq 0.50$ (1st route), a cubic domain of empty voxels is defined in the first step (for example, when $S_{RVE} = 10^3$, a domain of $10 \times 10 \times 10 = 1000$ voxels is considered). The first voxel of matter is then created in the center of the domain, and the foam (a pathway of matter voxels) is generated by affecting the matter to a randomly picked neighbor, sharing a face with the just previously created matter voxel. This affectation process is performed until the target pore volume fraction is reached. This approach guarantees that all matter voxels share at least one common face.

Meanwhile, if $0.50 > PVF_{in} > 0$ (2nd route), the algorithm takes an inverse approach by first defining a cubic domain of matter voxels. The same procedure as for the 1st route is then applied, but instead, a pathway of empty voxels is created within the matter. Since both the algorithms imply random choices in pathway creation, foam architectures generated during their execution are never exactly identical.

After a matter pathway has been created (with the 1st route), a final scan over the entire domain is carried out to locate the empty voxels completely surrounded by matter (closed porosity) and to transform them into matter voxels. Conversely, once a pathway of empty voxels has been created (the 2nd route), a scan is carried out to locate the groups of matter voxels that are not connected to other matter voxels (loose particles) and to transform them into void voxels. After this scanning-correction procedure, the resulting open-cell pore volume fraction (PVF_{out}) may be slightly different than the targeted PVF_{in}, but the maximum difference between PVF_{in} and PVF_{out} would not exceed 0.015 (and this case occurred when $PVF_{in} = 0.5$ and $PVF_{out} \approx 0.485$). Finally, the generated foams contain only two distinct components: a macro-path of matter and a macro-path of voids, in which all the matter/void voxels are interconnected.

The following considerations were taken into account when justifying these two alternative routes. If, contrarily to the established procedure, the 2nd route (a void pathway in a matter domain) is employed when $PVF_{in} > 0.50$, the generated foam would contain a significant amount of loose matter, since the path of void voxels would repeatedly intersect itself; and the higher the PVF_{in}, the greater the risk. Similarly, if the 1st route (matter pathway in an empty domain) is followed when $PVF_{in} < 0.5$, there is the risk of generating a significant quantity of closed cells. As an example, the use of the 1st route for $PVF_{in} = 0.30$ resulted in an unacceptable level of 30% of closed pores ($PVF_{out} = 0$) (Maîtrejean, Terriault et Brailovski, 2013b).

For illustration purposes, Figure 2.3 presents the progression of matter voxels for $S_{RVE} = 12^3$ and $PVF_{in} = 0.75$, Figure 2.4 shows three different S_{RVE}-PVF_{in} combinations, and Figure 2.5 presents 2D-slices of three RVEs of the same size ($S_{RVE} = 40^3$) with porosities ranging from 0.25 to 0.70. If these 2D-slices are analyzed in conformity with the image-based morphology evaluation approach presented in Section 2.5, the metrics d_{10}, d_{50} d_{90}, c_{50}, r_{50} and N_p would be obtained. Adding these six metrics to the value of the resulting open-cell porosity (PVF_{out}) provides a complete set of seven output parameters that will be employed later in this work.

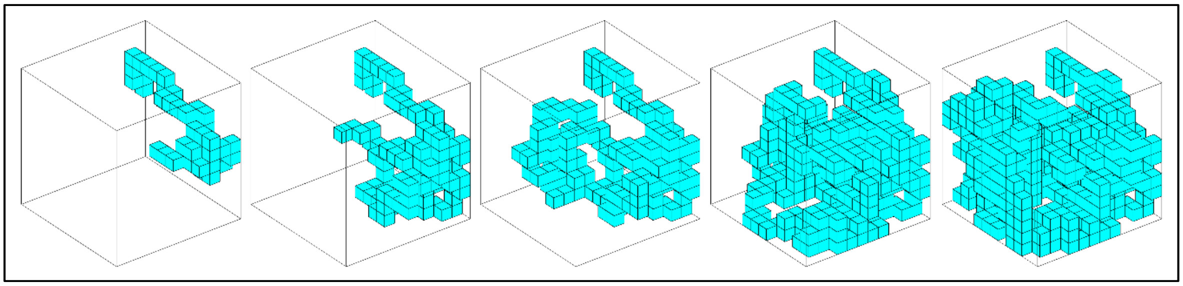

Figure 2.3 Evolution of the path of matter voxels ($S_{RVE} = 12^3$ and $PVF_{in} = 0.75$)

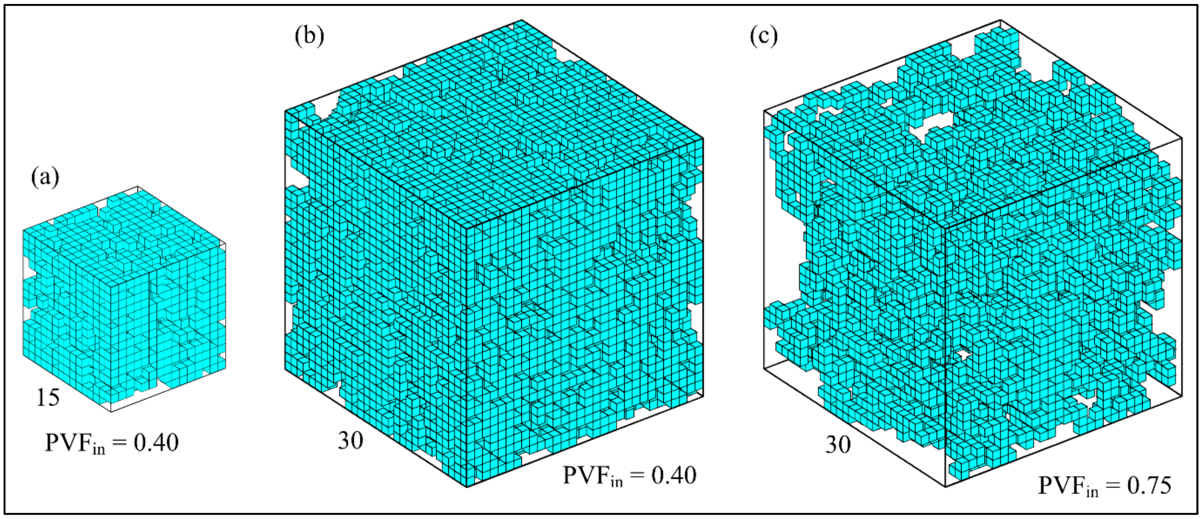

Figure 2.4 Typical RVEs for the following S_{RVE}-PVF_{in} combinations: (a) 15^3-0.40, (b) 30^3-0.40 and (c) 30^3-0.75

Figure 2.5 RVE slices for $S_{RVE} = 40^3$ with PVF_{in} of 0.25 (a), 0.40 (b) and 0.70 (c)

2.6.2 Minimum size of the RVE

The size of the smallest RVE capable of representing foam morphology is obtained from a convergence analysis where S_{RVE} is incremented until it satisfies some convergence criteria. It is expected that the minimum size of the RVE will depend on the pore volume fraction. To realize this analysis, for a PVF_{in} ranging from 0.05 to 0.95 by steps of 0.05, RVEs are generated by increasing their size from a minimum of 4^3 up to a maximum of 200^3 by steps of 2^3. Then, for each RVE, a total of $3 \times S_{RVE}$ slices are made. For example, with $S_{RVE} = 20^3$, three sets of 20 slices, for a total of 60, are realized in plans XY YZ and XZ (parallel to the RVE faces). Finally, for each RVE, each slice is analyzed using the built-in MATLAB function "RegionProps" and all the resulting pores are combined to calculate the seven metrics d_{10}, d_{50} d_{90}, c_{50}, r_{50}, N_p, and PVF_{out}.

A preliminary study (results are not presented here) showed that the greater the number of individual pores analyzed, the closer each metric is to its stabilized value. In this work, for a given RVE, we sum up all the 2D pore contours from the 3 × SRVE slices. We are aware that with this approach, each individual pore is intersected, and therefore analyzed, more than once. It has been verified, however, that these redundancies do not affect the results of the convergence analysis. Indeed, every pore analyzed is a cross-section of the same "macro-pore" since there is only a single path of empty voxels.

Figure 2.6 is a typical set of diagrams illustrating the evolution of the seven output parameters for a given $PVF_{in} = 0.45$ when S_{RVE} increases from 4^3 to 200^3. Figure 2.6a–c contain the following metrics: (a) PVF_{out}, N_p; (b) d_{10}, d_{50} and d_{90}; and (c) c_{50} and r_{50}. To compensate for the algorithm's randomness, the plots have been smoothed using a MATLAB curve-fitting function, LOESS, a "local regression using weighted linear least squares and a 2nd degree polynomial model".

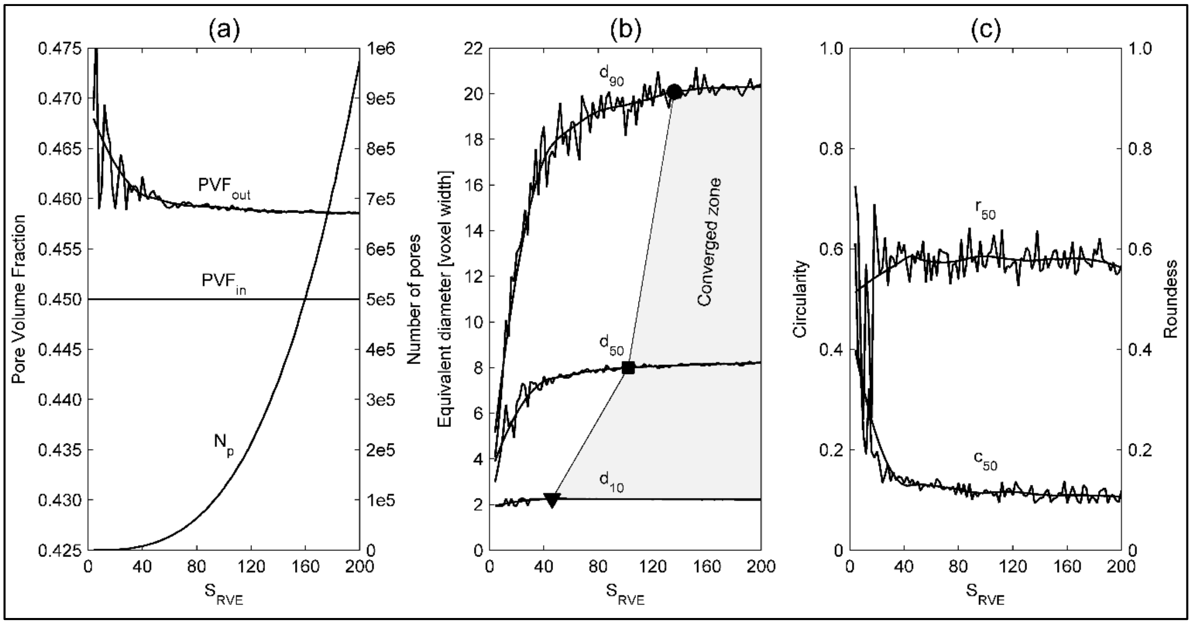

Figure 2.6 Convergence study for S_{RVE} varying from 4^3 to 200^3 ($PVF_{in} = 0.45$): (a) PVF_{out} and N_p, (b) d_{10}, d_{50} and d_{90}, and (c) c_{50} and r_{50}, as functions of the S_{RVE}

It can be observed that as S_{RVE} increases, all output parameters, except the constantly increasing N_p, converge to some stable values, but with different convergence rates. Indeed, convergence of the pore size metrics (d_{10}, d_{50} and, especially, d_{90}) is reached at higher RVEs than the foam porosity (PVF_{out}), or the pore shape metrics (c_{50} and r_{50}) convergences. The RVEs corresponding to the convergent values of each metric are called "the respective minimum Representative Volume Element", or S_{RVE}^{min}.

Convergence is considered to be reached when the deviation between six consecutive smoothed values of d_{10}, d_{50} or d_{90} becomes smaller than 0.1%. For example, when $PVF_{in} = 0.45$, values S_{RVE}^{min} for d_{10}, d_{50} and d_{90} correspond to 46^3 (triangle mark), 102^3 (square mark) and 136^3 (dot mark), respectively (Figure 2.6b).

This convergence study is applied to numerically-generated foams with target porosity ranging from 0.05 to 0.95 to determine at which S_{RVE} their metrics d_{10}, d_{50} and d_{90} become convergent. The results of this convergence study for the most restrictive pore size metric (d_{90}) as a function of S_{RVE} are illustrated in Figure 2.7. It can be seen that convergence is reached only for PVF_{out}

smaller than 0.49 (the converged d_{90} and the corresponding S_{RVE}^{min} are marked with dots, while the run-out (unconverged) plots end with arrows).

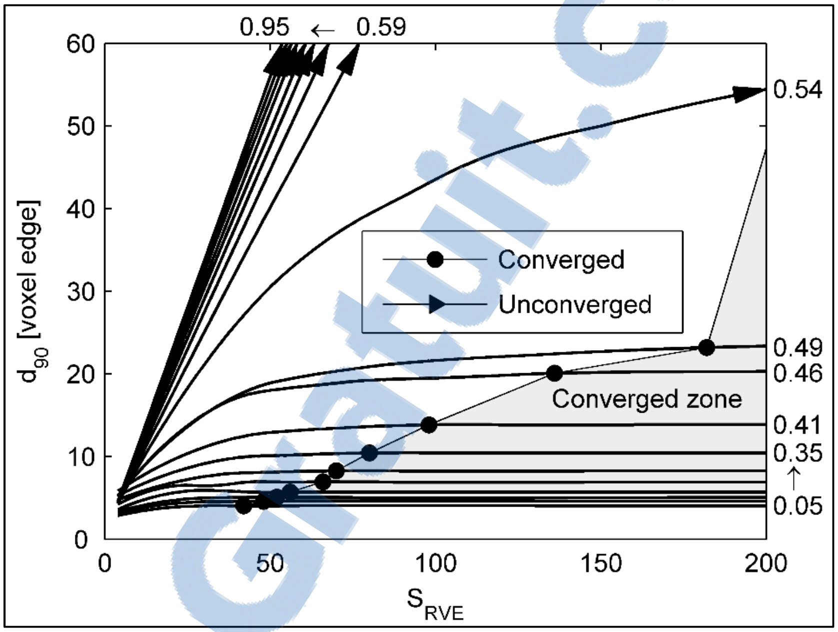

Figure 2.7 Convergence of d_{90} as a function of S_{RVE} for PVF_{out} values of 0.05 to 0.95.

To summarize, S_{RVE}^{min} for d_{10}, d_{50} and d_{90} are plotted as functions of PVF_{out} in Figure 2.8. These results are also in Table 2.1, where the corresponding PVF_{in} values are also specified. Thus, for a selected PVF_{out}, it is possible to determine the input parameters PVF_{in} and S_{RVE}^{min} leading to the smallest model size respecting one of the three convergence criteria: d_{10}, d_{50} or d_{90}. The evolution of the pore size to the minimum RVE size ratio (d_{90}/S_{RVE}^{min}) as a function of PVF_{out} is also plotted in Figure 2.8. The interrelations between the drastic increase of this ratio and the loss of convergence observed in the vicinity of $PVF_{out} \approx 0.49$ (Figure 2.7) are discussed in more detail in Section 2.8.

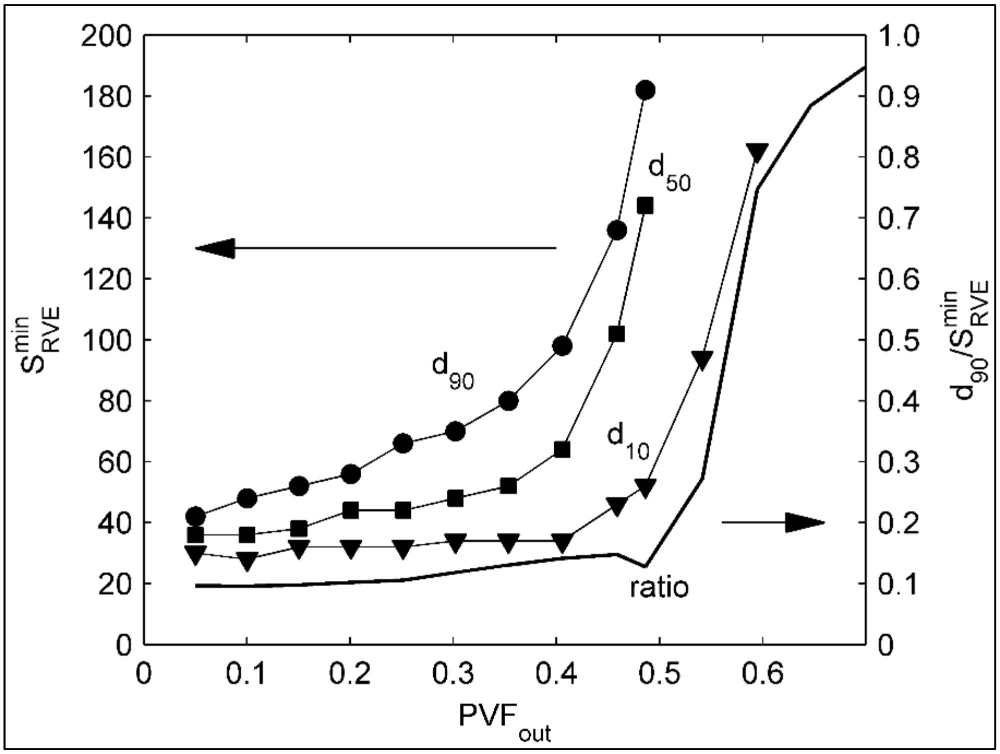

Figure 2.8 S_{RVE}^{min} for d_{10}, d_{50} and d_{90}, and d_{90}/S_{RVE}^{min} as functions of PVF_{out}

Table 2.1 Converged value of S_{RVE}^{min} for different values of PVF

PVF_{out}	PVF_{in}	S_{RVE}^{min} (d_{10})	S_{RVE}^{min} (d_{50})	S_{RVE}^{min} (d_{90})
0.05	0.05	30	36	42
0.10	0.10	28	36	48
0.15	0.10	32	38	52
0.20	0.20	32	44	56
0.25	0.25	32	44	66
0.30	0.30	34	48	70
0.35	0.35	34	52	80
0.41	0.40	34	64	98
0.46	0.45	46	102	136
0.49	0.50	52	144	182
0.54	0.55	94	-	-
0.60	0.60	162	-	-
0.65 to 0.95	0.65 to 0.95	-	-	-

In summary, this section describes how to establish the minimum sizes of the RVEs beyond which no further increases in size will result in noteworthy changes in foam morphology (pore size & shape metrics). Multiple values of S_{RVE}^{min} were calculated according to the different convergence criteria (d_{10}, d_{50} or d_{90}) valid for $PVF_{out} < 0.49$ (d_{50} and d_{90}) or $PVF_{out} < 0.60$ (d_{10}).

2.7 Validation

2.7.1 Foams manufacturing

The metallic foams produced in this study to validate the morphology generation algorithm are manufactured using the space holder method (Imwinkelried, 2007; Niu et al., 2009). The processing starts with two components in powder form: a metal and a spacer. The metal powder is commercially pure titanium grade 2 (TiCp) obtained from TLS Technik Spezialpulver (Germany). As received, the powder is composed of spherical particles smaller than 250 µm in diameter. The spacer is a polymethylmethacrylate (PMMA, Solarkote® PB, Arkema, USA). Both the metallic and PMMA powders are sieved to obtain an appropriate log-normal particle size distribution: $d_{10} = 18$ µm, $d_{50} = 36$ µm and $d_{90} = 60$ µm (metal) and $d_{10} = 51$ µm, $d_{50} = 120$ µm and $d_{90} = 228$ µm (spacer) (Laser diffraction Mastersizer 3000 system, Malvern Instr.). This distribution results in the highest compression resistance of the produced foams (testing results are not presented here).

The metal-spacer powder ratio is adjusted to obtain the desired pore volume fraction, and a custom-built rotating container equipped with blades is then used to ensure a homogeneous distribution of the constituents. The mixture is uniaxially compressed at 180 MPa in a hardened steel cylindrical mold to yield a 14 mm-diameter, 16 mm-height green product.

The green product is then introduced into the sintering furnace (WEBB 120) for spacer pyrolysis under 10^{-2} mbar vacuum atmosphere. The pyrolysis temperature (450 °C), heating rate (2 °C/min) and time were experimentally determined to allow the spacer material to progressively leave the metal matrix without provoking specimen collapse. The resulting brown product is sintered in the same furnace under vacuum (10^{-7} mbar) at 1300 °C for 3 h with subsequent furnace cooling. Note that in this work, the foams obtained from the space holder method present the same interconnected open-cell pore architecture as the numerically-generated foams, which makes their comparison appropriate. The architectural similarity also means that the numerical foam generation resembles at a certain extent their manufacturing process.

Five lots of foams with different open-cell pore volume fractions (0.18, 0.33, 0.38, 0.48 and 0.68) were manufactured and their morphology was analyzed using 12 cross-section optical micrographs per specimen. A typical Ti foam specimen and the binarized cross-section optical micrographs (25X) of foams with PVF of 0.18, 0.48 and 0.68 are shown in Figure 2.9. Table 2.2 contains the pore size metrics obtained from the micrographs using the “RegionProps” function from MATLAB software (Section 2.5).

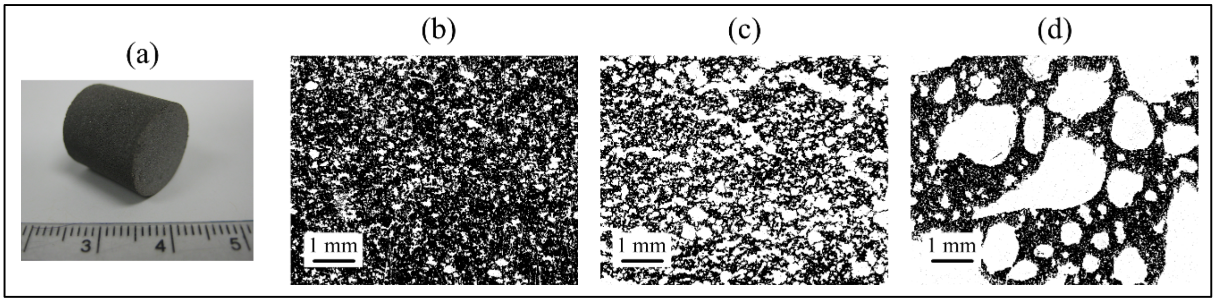

Figure 2.9 (a) Ti foam specimen (PVF = 0.39); binarized cross-section optical micrographs for PVF = 0.33 (b), 0.48 (c) and 0.68 (d)

Table 2.2 Pore size metrics for manufactured Ti foams

PVF	**d_{10} [μm]**	**d_{50} [μm]**	**d_{90} [μm]**
0.18	24	85	225
0.33	34	136	409
0.38	41	183	541
0.48	67	426	1634
0.68	163	1712	3024

2.7.2 Experimental validation

The final step prior to the validation of the morphology generation algorithm is to find a conversion factor (α) linking the image unity of the numerical model (voxel width) to that of the experimental foam length unit (μm). To perform such a mapping, 1 voxel width is first converted to 1 μm, and then to 2, 3 …, and, finally, to 50 μm; after each conversion, the resulted numerical pore size distribution is compared with the experimental data. The match is deemed to be successful when the sum of squared errors (*SSE*) between the numerical and experimental pore size metrics (d_{10}-d_{50}-d_{90}) for the whole range of PVFs reaches a minimum (Eq. (2.4)). Moreover, since the deviations between the numerical and the experimental values of three pore size metrics differ significantly ($d_{90} > d_{50} > d_{10}$), they have been normalized (relative to the numerical values) to compensate for such disparities (Eq. (2.5)). Also, note that since the PVFs of the numerical and experimental foams are not exactly identical (Table 2.1

and Table 2.2), $S_{\mathrm{RVE}}^{\mathrm{min}}$ values of the numerical foams with the same PVF as the experimental foams are found by linear interpolation, and the corresponding pore metrics subsequently calculated.

$$SSE = \sum_{PVF} \Delta d_{10}^2 + \Delta d_{50}^2 + \Delta d_{90}^2 \tag{2.4}$$

$$\Delta d_{xx} = \frac{d_{xx,num} - d_{xx,exp}}{d_{xx,num}} \tag{2.5}$$

Following this mapping (calibration) procedure, the conversion factor α = 36 μm/voxel width was found to lead to the best match of the numerical and experimental pore size metrics and their distribution. The comparisons of pore size and shape distributions for a specific PVF are shown in Figure 2.10. Figure 2.10a, b show the pore size distribution for the experimental (a) and the numerical (b) foams, while Figure 2.10c compares their cumulative distributions along with their best-fit log-normal distributions ($\mu = 10.11$ and $\sigma = 1.69$ for the experimental distribution and $\mu = 10.14$ and $\sigma = 1.39$ for the numerical distribution). Finally, Figure 2.10d superposes the numerical and the experimental pore shape distributions (circularity and roundness). Note also that since the Ti foam selected for this experimental–numerical comparison possesses a PVF of 0.38, the minimum RVE size has been determined with a linear interpolation from Table 2.1, it corresponds to $S_{\mathrm{RVE}}^{\mathrm{min}} = 90^3$ (d_{90}). The generated $S_{\mathrm{RVE}} = 90^3$ therefore has an apparent volume of $3.2 \times 3.2 \times 3.2$ mm^3.

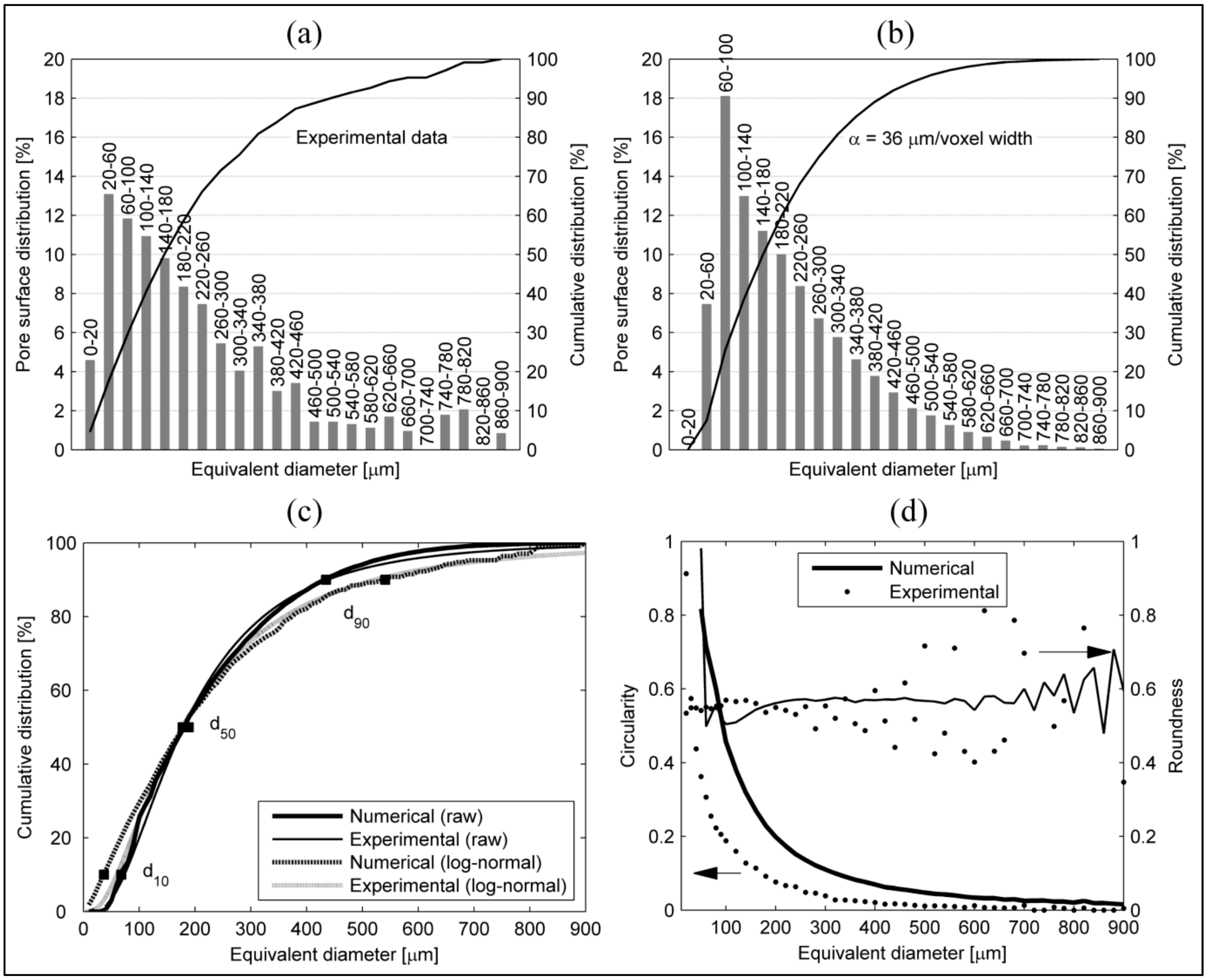

Figure 2.10 (a) Experimental pore size distribution, (b) numerical pore size distribution, (c) pore size cumulative distributions comparison including the best-fit log-normal distributions, and (d) pore shape distribution comparison (PVF = 0.38)

In Figure 2.11 , the d_{10}, d_{50} and d_{90} pore size metrics are superposed for the experimental (0.18 to 0.68) and the numerical (0.05 to 0.49) pore volume fraction ranges. This last comparison determines whether the RVE approach employed for modeling the metallic foam morphology is efficient. Note that in Figure 2.11, the numerical pore size metrics correspond to the values obtained from the convergence study of d_{50} (Table 2.1).

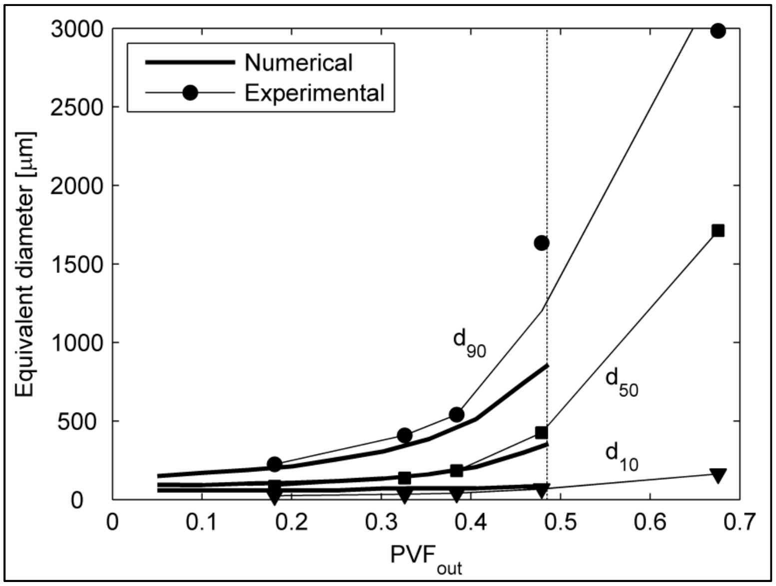

Figure 2.11 Comparison of experimental and numerical pore size metrics as a function of PVF_{out}

2.8 Discussion

2.8.1 Convergence of the RVE metrics

In Section 2.6.2, the convergence process fails for RVEs higher than $PVF_{out} = 0.60$ (d_{10}) and $PVF_{out} = 0.49$ (d_{50} and d_{90}), as observed in Figure 2.7 and Figure 2.8. Indeed, above these limits, it can be considered that each slice contains a unique macropore having an equivalent diameter that can be fairly estimated by Eq. (2.6). In other words, the size of pores in this case is as large as the size of the RVE.

$$d = \sqrt{\frac{4}{\pi} \cdot S_{RVE}^2 \cdot PVF} \tag{2.6}$$

Note also that when $PVF_{out} = 0.49$, $d_{90}/S_{RVE}^{min} \approx 0.15$, i.e., the equivalent diameter of larger pores (d_{90}) approaches 1/6 of the size of the RVE. When this threshold value is exceeded, d_{90}/S_{RVE}^{min} rapidly increases, tending to unity when $PVF_{out} > 0.7$ (Figure 2.8).

The observed effect is not related to the convergence criterion nor to the modeling algorithm, since foams with consistent morphology (matters elements interconnected by at least one face) are always obtained regardless of the target PVF. In fact, this should be interpreted as a limit of the use of the pore size metrics d_{10}, d_{50} and d_{90}. Indeed, for highly porous open-cell foams, the classical stereology approach may not be ideal for characterizing foam morphology (Schladitz et al., 2008). Furthermore, the concept of pore size relies on the fact that the pores must be well-defined isolated objects with a convex shape (Pabst et al., 2011), and such requirements are no longer met with RVE slices for $PVF_{out} \geq 0.49$ of (Figure 2.5). In other words, when $PVF_{out} > 0.49$, the foam morphology modeling algorithm is still relevant, but the foam morphology characterization method used in this work is no longer appropriate.

In such situations, other metrics such as a mean chord length for poorly-defined pores (Hilliard et Lawson, 2003), or edge thickness for foams with ordered morphology (Gibson et Ashby, 1999) should be applied. However, these new metrics or characterization methods will inevitably measure morphological features that are different from those quantified using stereology (Maire et al., 2007), such as interpore connections or pore throat size, for example (Otsuki et al., 2006).

2.8.2 Mapping of the RVE

From Figure 2.8 or Table 2.1, it is clear that convergence of d_{90} leads to larger S_{RVE}^{min} values than convergences of d_{50} and d_{10} and, consequently, to different pore size metrics (see Figure 2.6b for instance). On this last figure, it can be observed that when S_{RVE}^{min} (d_{10}) is reached (46^3), d_{50} and especially d_{90} pore size metrics are definitely not converged. However, when S_{RVE}^{min} (d_{50}) has reached (102^3), d_{90} is almost stabilized and d_{10} is converged. Finally, when S_{RVE}^{min} (d_{90}) reaches (136^3), the three pore size metrics are converged. This trend has been observed for the whole range of the porosities covered in this study.

For this work, S_{RVE}^{min} (d_{50}) has been defined as the smallest RVE size capable of representing the foam morphology, even if the sizes of larger pores have not yet completely stabilized. This choice was made in order to have a good compromise between morphological preciseness and the size of the RVE. Further details are given later regarding the S_{RVE} and its impact on computing time. This definition explains why Figure 2.11 has been plotted with data obtained from the convergence of d_{50}. However, the minimum sizes of the RVE obtained from the convergence of d_{90} might be useful for modeling the real impact that the foam morphology has on its mechanical behavior.

2.8.3 Experimental validation

In Figure 2.11, for PVF_{out} less than 0.40, good agreement is obtained between the numerical and the experimental pore size metrics. However, for PVF_{out} between 0.40 and 0.49 (where convergence was still reached), comparison of pore size metrics is only valid for d_{10} and d_{50}, while a significant deviation is observed for d_{90}. Considering that the morphology generation algorithm was executed without any modification and that the convergence of the numerical model was reached, this deviation could be attributed to the peculiarities of the manufacturing process.

Indeed, as Brailovski et al. (2011) encountered a similar situation when they manufactured Ti-Nb-Zr foams at 0.46 to 0.65 of PVF; and the emergence of large pores as PVF rises has been frequently observed during manufacturing (see Figure 2.9c and d in particular). This could be attributed to pressure increase in some regions of the foam during spacer pyrolysis (the foaming effect). In summary, the appearance of such large pores, which become prevalent as the PVF increases, is due to the specificity of the manufacturing process, and is not replicated in the actual modeling algorithm.

When comparing the pore circularity data of Figure 2.10d, both the experimental and numerical distributions follow an exponential law. However, an offset is clearly distinguishable between the two curves. This is in part due to the fact that the circularity of the smallest numerical pore observed in the RVE slices corresponds to that of a square ($c = 0.78$), while circularity of the experimental pore tends to 1. Still from Figure 2.10d, an analysis of the experimental pore roundness distribution for large pore size is difficult to realize, as the pores become strongly distorted. However, for both approaches, a mean roundness akin to r_{50} is a good metric to quantify this aspect of the pore shape. Finally, it should be mentioned that for medical applications, the influence of pore shape is not a high priority when compared to that of pore size (Turner et al., 1986).

2.8.4 Medical applications

Keeping in mind that these metallic foams will be used for medical implants, it must be mentioned that successful bone ingrowth into the foamed implant is strongly influenced by pore size. An efficient level of bone ingrowth will occur with interconnected pore size varying from 50 to 800 µm (Lefebvre, 2013).

The lower limit is generally established as the size of an osteoblast, which is about 50 µm. When PVF < 0.30, d_{10} < 60 µm (Figure 2.11), which means that the PVF smaller than 0.30 would inhibit efficient bone ingrowth. For the higher limit, it has been widely observed that the risk of fibrous tissue formation increases when pore size is larger than 1 mm (Bobyn et Miller, 1994). That means that the practical use of PVF > 0.49 is also limited, since the d_{90} metric of our numerical foams is higher than 850 µm in this porosity range (Figure 2.11).

In summary, the PVF_{out} of metallic foams should be within the range of 0.30 to 0.49, which corresponds to Shen et al. (2006). Note that this assumption is made from a strictly morphological point of view. Indeed, from the mechanical point of view, some compromises will need to be done in order to match the stiffness of the foam and that of bone.

2.8.5 RVE creation time

The computing time required by the algorithm for the foam morphology generation is proportional to the number of voxels created. This evolution can be seen in Figure 2.12 when S_{RVE} varies from 4^3 to 200^3, for a pore volume fraction of 0.46.

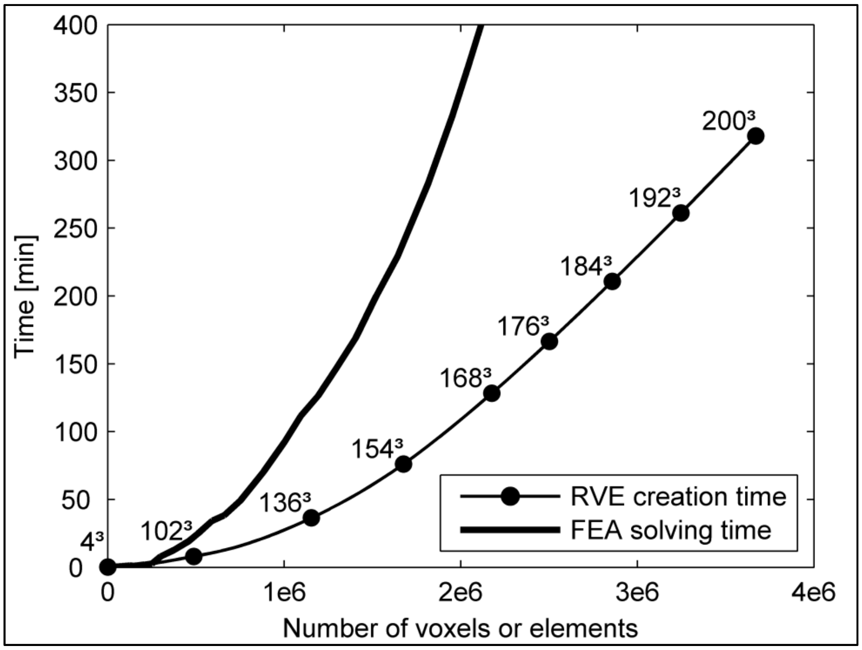

Figure 2.12 RVE creation and FEA solving time as functions of the number of voxels or elements (PVF = 0.46)

In this paper, where we have only studied the foam morphology, almost linear increase in computing time when the number of voxels exceeds $2 \cdot 10^6$ is not such disturbing. However, if a finite element analysis (FEA) needs to be performed on these foams, any increase in S_{RVE} will have a much more severe impact on the computing time. To illustrate this, we superimposed on the ”number of voxels-RVE creation time” plot of Figure 2.12, the solving time of a basic FEA as a function of number of elements (we consider one element per voxel). This simplified FEA consisted of a one-step, small-deflection, uniaxially-stretched, displacement-controlled, structural analysis of a cube. It is clear from Figure 2.12, that for the same number of elements (or voxels), the FEA solving time is always much higher than the RVE creation time, thus representing a strongest incentive to keep S_{RVE} as low as possible. All the RVE creation and FEA simulation routines were conducted in this study on a desktop computer: Intel® Core(TM) i7-3930 K CPU @ 3.20 GHz with 32 GB RAM.

2.9 Conclusions

The objective of this study is to experimentally validate an algorithm developed to generate the explicit morphology of foams with the Representative Volume Element (RVE) approach. Such an RVE creation algorithm is an alternative to the 3D reconstruction using X-ray tomography. The foam morphology was analyzed using stereology, a characterization method based on the direct observation of foam cross-sections, to quantify the pore size, shape and distribution. It has been shown that the morphology generation algorithm is capable of generating open-cell foams containing neither loose matter, nor close cells. Finally, the smallest sizes of the RVE that will preserve the essential morphological features of our foams in terms of their pore size, shape and distribution were determined and experimentally validated up to PVF ≈ 0.49.

For PVF > 0.49 however, the morphology characterization method used in this work (stereology) failed to provide detailed morphology data. However, such a limitation cannot be attributed to our foam-generation algorithm, since consistent foams were continually obtained up to PVFs as high as 0.95, but simply indicates to the inherent limitation of the stereology, as a foam characterization technique.

Finally, future works needs to be devoted to modeling and experimental validation of the mechanical behavior of such RVEs. Special attention should be taken when minimizing the RVEs so that they are not only morphologically but also mechanically representative of the real foam structures. Also, the quality of the morphology modeling algorithm could be improved by considering a higher order voxels connectivity (18- or 26-connectivity) instead of the 6-connectivity used in this study. Such an improvement could also positively affect the mechanical resistance of such porous structures.

2.10 Acknowledgments

The authors would like to credit the Fonds de Recherche du Québec Nature et Technologies (FRQNT) and the Natural Sciences and Engineering Research Council of Canada (NSERC) for their financial support.

CHAPITRE 3

DESIGN, MANUFACTURE AND TENSILE PROPERTIES OF STOCHASTIC POROUS METALLIC STRUCTURES

Charles Simoneau, Vladimir Brailovski, Patrick Terriault

Département de génie mécanique, École de technologie supérieure,
1100, rue Notre-Dame Ouest, Montréal, Québec, Canada H3C 1K3

Article publié dans la revue « Mechanics of Materials »,
vol. 94, p. 26-37, mars 2016

3.1 Avant-propos

La deuxième étape de ce projet consiste à déterminer les propriétés mécaniques des structures poreuses générées par l'algorithme. La caractérisation mécanique est faite à deux niveaux, soit numérique à l'aide de la méthode des éléments finis et expérimental à l'aide d'essais de traction sur des échantillons produits par fabrication additive. Il est à noter que les essais expérimentaux sont notamment réalisés pour la validation du modèle éléments finis. Une fois validés, le modèle numérique ainsi que les propriétés mécaniques des structures poreuses pourront être utilisés pour la suite du projet.

3.2 Résumé

Une approche méthodologique est développée pour concevoir, fabriquer et tester des structures poreuses stochastiques pour applications médicales. En premier lieu, la méthode des éléments finis et l'approche du volume élémentaire représentatif sont utilisées conjointement afin de déterminer les dimensions minimales de la section utile des échantillons de traction poreux. Un gradient de porosité est ensuite créé afin d'assurer une transition entre les sections poreuses et denses des échantillons situées respectivement au centre (section utile) et aux extrémités (serrage des mors). En deuxième lieu, le procédé de fusion sélective sur lit de poudre est utilisé pour la fabrication additive d'échantillons de traction en cobalt-chrome dont la porosité varie

de 30 à 50 %. En troisième lieu, les échantillons sont soumis à des essais de traction jusqu'à leur rupture permettant ainsi la caractérisation de leurs propriétés mécaniques. Le comportement élastique des échantillons de traction dans la section poreuse utile ainsi qu'au niveau du gradient de porosité est comparé avec succès aux résultats d'analyses numériques ainsi qu'avec la littérature.

3.3 Abstract

An original methodology was proposed to design, manufacture and test stochastic porous open-cell structures for medical applications. The first phase of the design procedure consisted in the numerical determination of the minimum representative size of the porous gauge section of testing specimens. Next, porosity gradients between the porous gauge section and the fully dense grip extremities of the specimens were created. The tensile specimens with porosities of 0.30, 0.40 and 0.50 were then produced using cobalt–chromium alloy powders and the Selective Laser Melting (SLM) technology. Finally, the specimens were subjected to uniaxial tension to failure to allow the determination of their stiffness and mechanical strength. The elastic response of these specimens in the central gauge section and the porosity gradient zones were in line with our numerical predictions and the literature data.

3.4 Introduction

In orthopedics, porous metals can be advantageously used for the replacement of damaged bones. To maximize the immediate and long-term success of orthopedic surgery, porous implants must fulfill specific biological and mechanical requirements. While biocompatibility and corrosion resistance are essential from a biological viewpoint (Lefebvre, 2013), it has been shown that a specific pore size range (50-800 μm) and an open-cell structure are two essential factors for a successful bone ingrowth (Bobyn et al., 1980). Furthermore, since the stiffness of porous implants can be adjusted to match that of bone, a stiffness mismatch between the implant and bone can be reduced, along with the risks of bone resorption and implant loosening. In addition to the mechanically biocompatible Young's modulus, the strength of porous implants must be higher than that of bone to prevent implant failure.

Generally speaking, the morphology of porous materials can be classified into two groups: stochastic (random) and ordered (regular, unit-cell), and it represents a fundamental aspect to take into account since it strongly impacts biomechanical compatibility requirements.

Despite the marked tendency to produce ordered structures for biomedical applications (see Campoli et al. (2013), Cansizoglu et al. (2008) and Horn et al. (2014)), numerous authors (Alkhader et Vural, 2008; Roberts et Garboczi, 2002; Sotomayor et Tippur, 2014; Tang et al., 2014) have raised the concern that these regular morphologies significantly differ from those of load-bearing natural cellular materials with strongly irregular interconnected-cell architectures. Moreover, Alkhader et Vural (2008) mentioned that random foams are more likely to have isotropic properties, as compared to the majority of regular lattice structures exhibiting a strong anisotropy. Random foam structures should therefore be favored over regular foams for such applications.

Two groups of manufacturing technologies are largely used to produce stochastic foams: (a) polymer-foam replication using deposition or infiltration-sintering techniques (Bobyn et al., 1999; Ryan, Pandit et Apatsidis, 2008), and (b) fugitive foaming or passive space-holder powder metallurgy techniques (Gauthier et al., 2004; Rivard et al., 2014). These methods have been widely reviewed by Banhart (2001) and Baumeister et Weise (2013) and many others. However, over the last two decades, additive manufacturing (AM) technologies have drawn the attention of the scientific community due to their capacity to produce complex customized parts and enable design optimization to meet specific application requirements.

Compared to traditional subtractive or formative manufacturing processes, AM technologies build near-net-shape parts directly from three-dimensional (3D) CAD models. Such a straightforward approach results in reduced energy consumption, carbon footprint, production time and cost (Frazier, 2014). In the biomedical domain, metal AM technologies are of particular interest since they can be used to create patient-specific implants which would exhibit porous morphology to promote bone ingrowth and therefore, solid fixation of the implant (Murr et al., 2011). Conventional subtractive or formative manufacturing processes can hardly combine these two advantages.

Although only a limited number of studies have so far been conducted on the AM-built stochastic open-cell metal foams, it is however possible to come up with a few. Among them, Cheng et al. (2014) and Murr et al. (2010a) successfully used computed tomography (CT), electron beam melting (EBM) AM technology and Ti–6Al–4V powder to replicate a biomimetic hip stem composed of an 81% porosity cylindrical core surrounded by a 76% porosity shell (Murr et al., 2010a), and the structure of a human femoral head (Cheng et al., 2014).

The advantages of producing stochastic foams for orthopedic implants using AM technologies being demonstrated, this paper focuses on the development of an original methodology for the design, manufacture and mechanical characterization of stochastic open-cell porous structures. Contrary to the majority of studies, in which these structures are characterized in compression, we orient our work toward their tensile characterization to prevent certain artifacts related to foam compression, such as cell densification or friction on the interface between the specimen and the platens of the testing machine. Moreover, the foam stiffness (E) and yield stress (S_Y) are identical when they are characterized in compression and in tension (Gibson et Ashby, 1999), and these two metrics are the most important mechanical properties to consider when developing load-bearing implant materials.

To reach this objective, a multiscale modeling approach and the random porosity morphology generation algorithm are used in this study (Section 3.5.1). The developed methodology is then presented in Section 3.5.2 through a step-by-step procedure. Next, Section 3.5.3 presents the determination of a minimum (or representative) size of the numerically-generated foams through finite elements-based simulations. This is followed by the design of tensile specimens with porosity gradients to allow an adequate connection between the porous gauge section and the fully dense grip extremities. The manufacture of these porous specimens using selective laser melting (SLM) AM technology is then presented in Section 3.5.4, while Section 3.5.5 is dedicated to the tensile characterization of the specimens. Finally, Sections 3.6 and 3.7 present the results and discussion, respectively.

3.5 Methodology of design, manufacture and testing of stochastic porous structures

3.5.1 Presentation of the multiscale modeling approach

The design procedure adopted in our work is based on a multiscale modeling approach involving a combination of micro-, meso- and macroscale models (Figure 3.1). Such an approach was adopted in our previous papers (Maîtrejean, Terriault et Brailovski, 2013b; Simoneau et al., 2014) considering the tremendous numerical cost associated with a direct finite element (FE) modeling of porous implant structures. A "macroscale" model is intended to simulate the global behavior of the implant. This model is homogeneous and makes abstraction of a complex structural organization of the implant. The mechanical properties of the macroscale model are equivalent to those of the porous material, and they are obtained with a "mesoscale" model. The morphology of the latter represents an assembly of interconnected matter voxels (or volumetric pixels) comprised within a cubic domain, called a Representative Volume Element (RVE). Finally, each finite element of an RVE is driven by a "microscale" model governed by the constitutive relations of a bulk (solid) material.

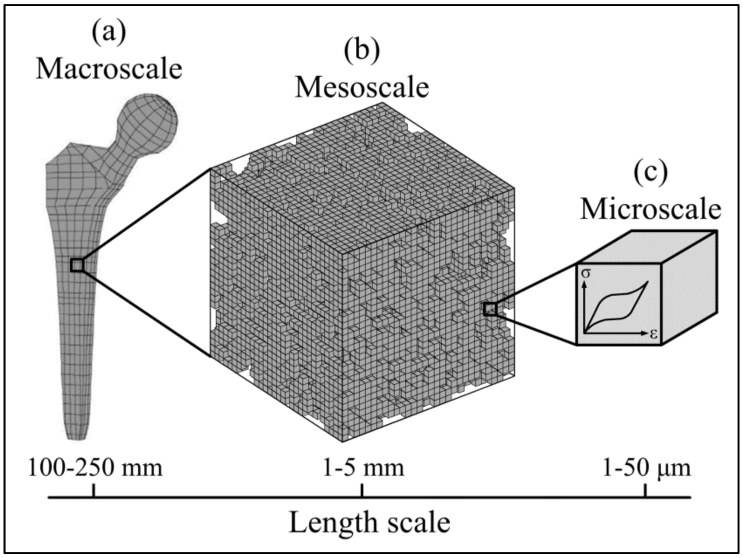

Figure 3.1 Schematization of the multiscale modeling approach adapted from Simoneau et al. (2014)

In this work, parallels can be drawn between each of the three modeling scales (macro-, meso-, and micro-) and a physical object, which in our case, is a tensile specimen. The macro- and mesoscale models are respectively associated with the tensile specimen as a whole, and with its Representative Volume Element (i.e., gauge section). The microscale model simulates the behavior of every matter voxel linked to the stress–strain diagram obtained through the testing of an entirely dense specimen produced from the same material (cobalt–chromium alloy) and by the same method (SLM) as its porous counterparts.

RVEs are created using an original morphology generation algorithm in the MATLAB 2013b environment (MathWorks, Natick, MA, USA) controlled by two parameters: the size of the cubic domain (S_{RVE}) and the pore volume fraction (PVF) (see Figure 3.2 for three different S_{RVE}-PVF combinations and refer to Simoneau et al. (2014) for details). This algorithm was developed in part to eliminate the need of using a CT-based digital reconstruction technique for foam geometry generation.

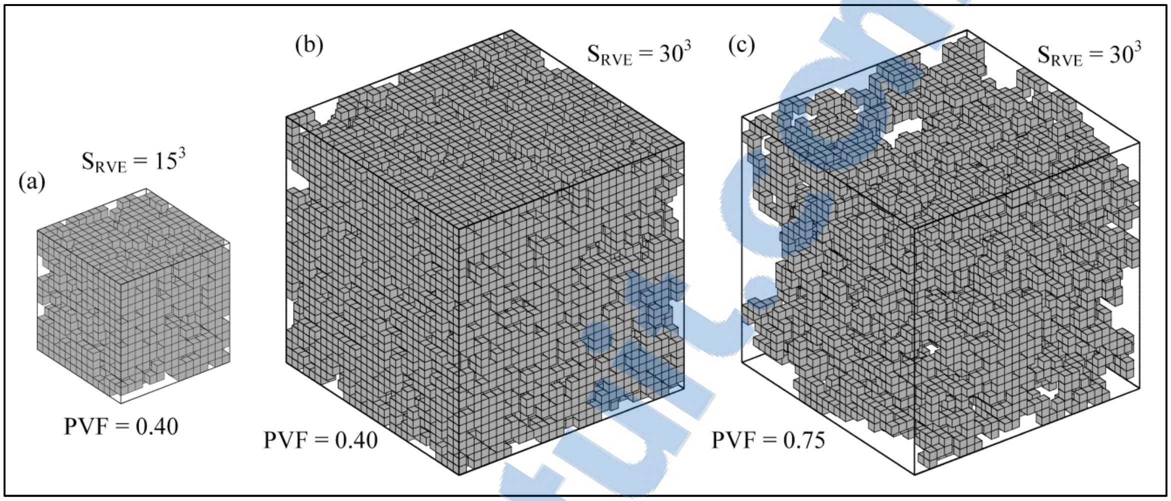

Figure 3.2 Typical RVEs for the following S_{RVE}-PVF combinations: (a) 15^3-0.40, (b) 30^3-0.40 and (c) 30^3-0.75 (adapted from Simoneau et al. (2014)).

3.5.2 Specimen design, manufacture and test process flow

Figure 3.3 presents the process flow depicting the design, manufacture and testing of the specimens, which is explained in detail below.

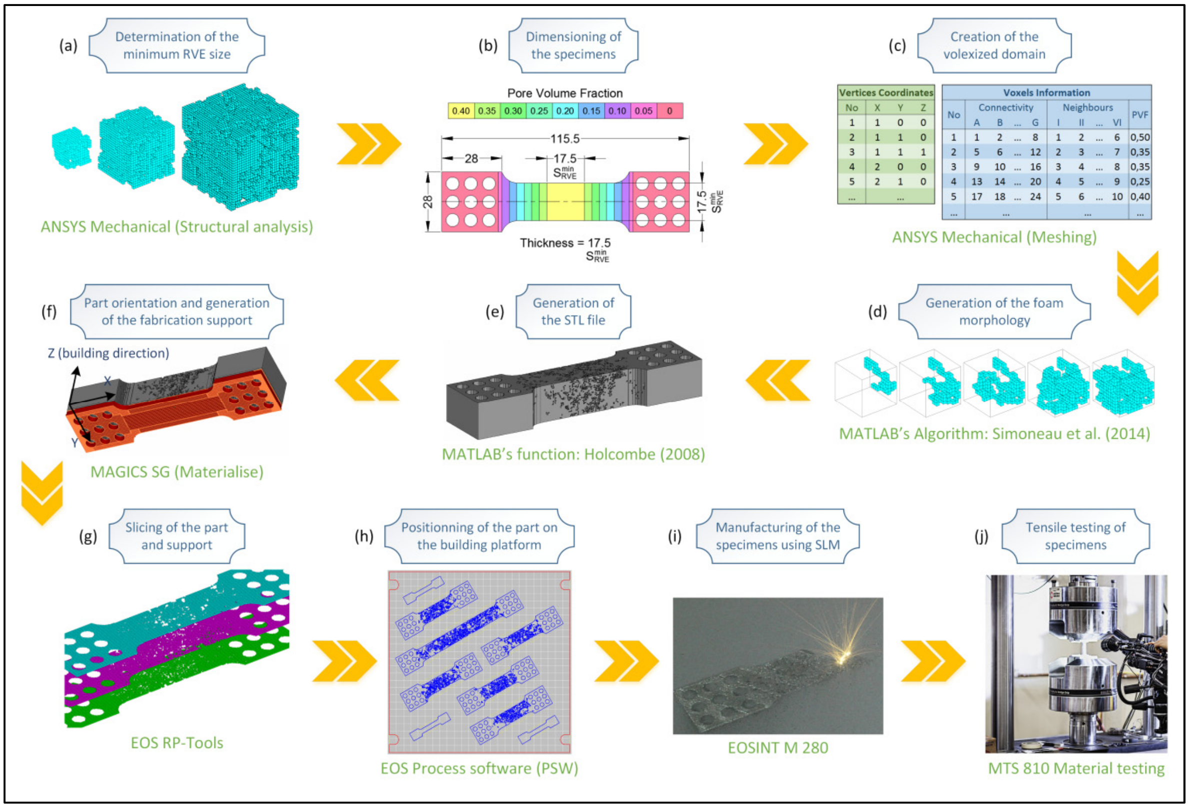

Figure 3.3 The step-by-step methodology from the specimens design to their testing

A. The design of tensile specimens (Figure 3.3a-d) is accomplished by the application of the multiscale modeling approach where the dimensioning of the specimen on the macroscale (Figure 3.1a) is fulfilled through the determination of the corresponding smallest mechanically-representative RVE at the mesoscale (Figure 3.1b). More specifically, the geometries of the specimen gauge section (length, width and thickness) for different levels of porosity are obtained using the minimum RVE sizes (Section 3.5.3.1 and Figure 3.3a). Furthermore, to avoid discontinuity at the interface between the porous (gauge) part of the specimens and their fully dense (grip) part, a porosity gradient is integrated into the specimen design (Section 3.5.3.2 and Figure 3.3b). This gradient provides a smooth transition between zones of different porosities, while preserving the interconnectivity of matter and void voxels, and it can be generated within an arbitrary irregular form, such as that of a dumbbell-shaped tensile specimen. Next, the creation of the voxelized domain of the tensile specimens (Figure 3.3c) is carried out with the ANSYS meshing module, where an FE mesh (i.e., a domain) composed of 8-node 3-D brick elements (i.e., voxels) replicates the geometry of the specimens from Figure 3.3b. The key domain-related information (nodal coordinates, neighboring element and connectivity) then serves as an input to the MATLAB algorithm to generate the specimen geometry (Figure 3.3d). (Note that the FE mesh of the fully dense domain allows the possibility of assigning a different porosity, and therefore, different equivalent material properties, to every element of the macroscale model.)

B. Next to the morphology generation, the specimens manufacture, including file processing and build preparation (Figure 3.3e-i) is firstly accomplished by generating the specimen's ASCII stereolithography (STL) file (Figure 3.3e) using a dedicated MATLAB function (Holcombe (2008), MATLAB Central File Exchange). The STL file is then transferred to the MAGICS 17.02 Support Generation Module (Materialise, Leuven, Belgium) to orient the part and generate the fabrication support structures linking the samples to the SLM machine building plate (Figure 3.3f). Next, both the supports and the parts are sliced (Figure 3.3g) and manually positioned on the building plate (Figure 3.3h) using RP TOOLS 6.1.8 and PSW 3.6 software, respectively (EOS GmbH, Munich, Germany). Finally, the specimens are manufactured (Section 3.5.4 and Figure 3.3i).

C. Section 3.5.5 presents the final step of the methodology consisting in the tensile testing of the specimen (Figure 3.3j).

3.5.3 Tensile specimens design

3.5.3.1 Minimum size of an RVE

To determine the smallest mechanically-representative RVE, a convergence study using displacement-controlled linear structural FE analysis of uniaxially-stretched RVEs with an incrementally-increased size is carried out. In detail, for each level of PVF ranging from 0.05 to 0.50, by steps of 0.05, the RVE size is increased from a minimum size of 4^3 up to a maximum size of 70^3, by steps of 2^3. Furthermore, for each studied RVE, a mesh sensitivity analysis based on the relative stiffness is also conducted by subsequently subdividing each voxel of the RVE into a cubic grid composed of $(1, 2, 3 \ldots n)^3$ 20-node 3D brick elements (Finite Elements per Voxel or FE_{VOXEL}).

The periodic boundary conditions are applied to each RVE to maintain the faces normal to the loading direction planar and parallel. These specific boundary conditions proposed by Shen et Brinson (2006) are not to be confused with symmetric boundary conditions. Since only small displacements are considered at this stage, the perfectly-elastic constitutive relation is used on the microscopic length scale (Figure 3.1c). Therefore, Young's modulus (E_S) and Poisson's ratio (ν_S) of the bulk (solid) material composing the foam (denoted with the "s" subscript) are the only two required material characteristics.

Following the application of the imposed displacements, the sum of the nodal forces along the loading direction on the restrained RVE face is divided by its apparent section. The calculated stress is subsequently divided by the imposed strain, and the apparent Young's modulus of the RVE (E) is thus obtained. This metric is finally expressed in terms of relative stiffness (E/E_S). Note that all the simulations are performed using the commercial FE software, ANSYS Mechanical APDL 15.0 (ANSYS, Canonsburg, PA, USA) on the McGill University Guillimin supercomputer (Montreal, Canada).

For a given porosity (PVF = 0.40) and size of an RVE ($S_{RVE} = 6^3$), typical mesh convergence results are presented in Figure 3.4, in which the evolution of the relative stiffness ratio (E/E_S) is plotted as a function of the number of finite elements per voxel (FE_{VOXEL}). For illustrative purposes, the corresponding meshes for FE_{VOXEL} of 1^3, 3^3, and 5^3 are also depicted. Based on these results, we can notice that $FE_{VOXEL} = 6^3$ ensures stable values of the relative stiffness, with less than 1% of deviation. Since similar observations were made for any porosity and size of an RVE, a resolution of $FE_{VOXEL} = 6^3$ is used for any PVF-S_{RVE} combination in this study.

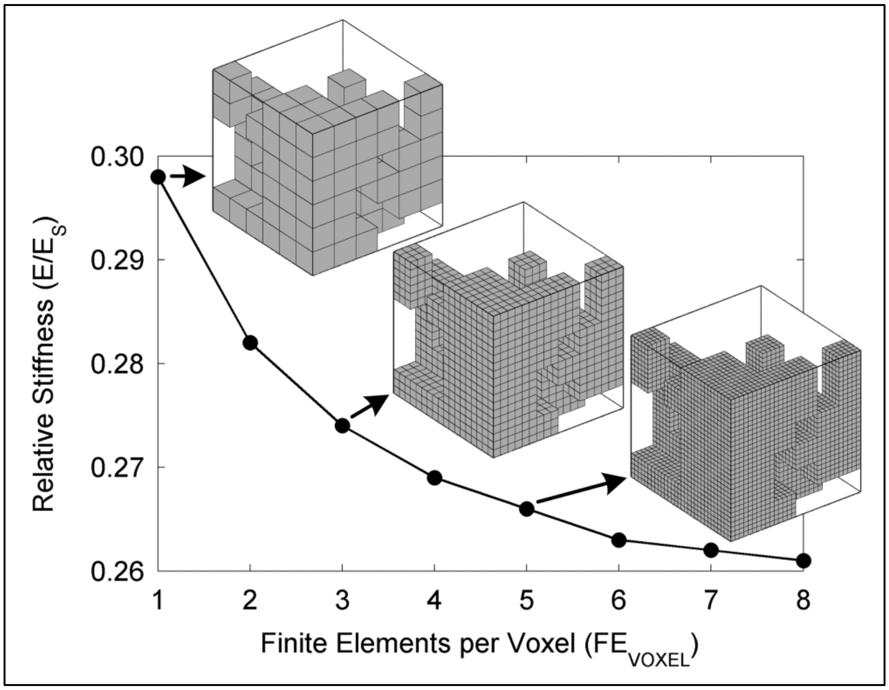

Figure 3.4 Influence of the number of finite elements per voxel (FE$_{VOXEL}$) on the relative stiffness (S$_{RVE}$ = 6^3 and PVF = 0.40)

Figure 3.5 presents the results of the convergence study, in which the relative stiffness (E/E$_S$) is plotted as a function of S$_{RVE}$ (4^3 to 70^3) for each level of porosity (PVF), ranging from 0.05 to 0.50. The relative stiffness data (thin lines) are then smoothed with the MATLAB curve-fitting function LOESS, a “local regression using weighted linear least squares and a 2nd degree polynomial model” (thick lines). Such a smoothing was carried out to compensate for the randomness of the porous structure generation algorithm. For each studied porosity, the converged, or minimum, size of an RVE (S_{RVE}^{min}, dot marks) is considered to be reached when the deviation between six consecutive smoothed values of E/E$_S$ becomes smaller than 1% (for example, $S_{RVE}^{min} = 38^3$ for PVF = 0.40). The converged zone is identified in Figure 3.5 by the shaded area.

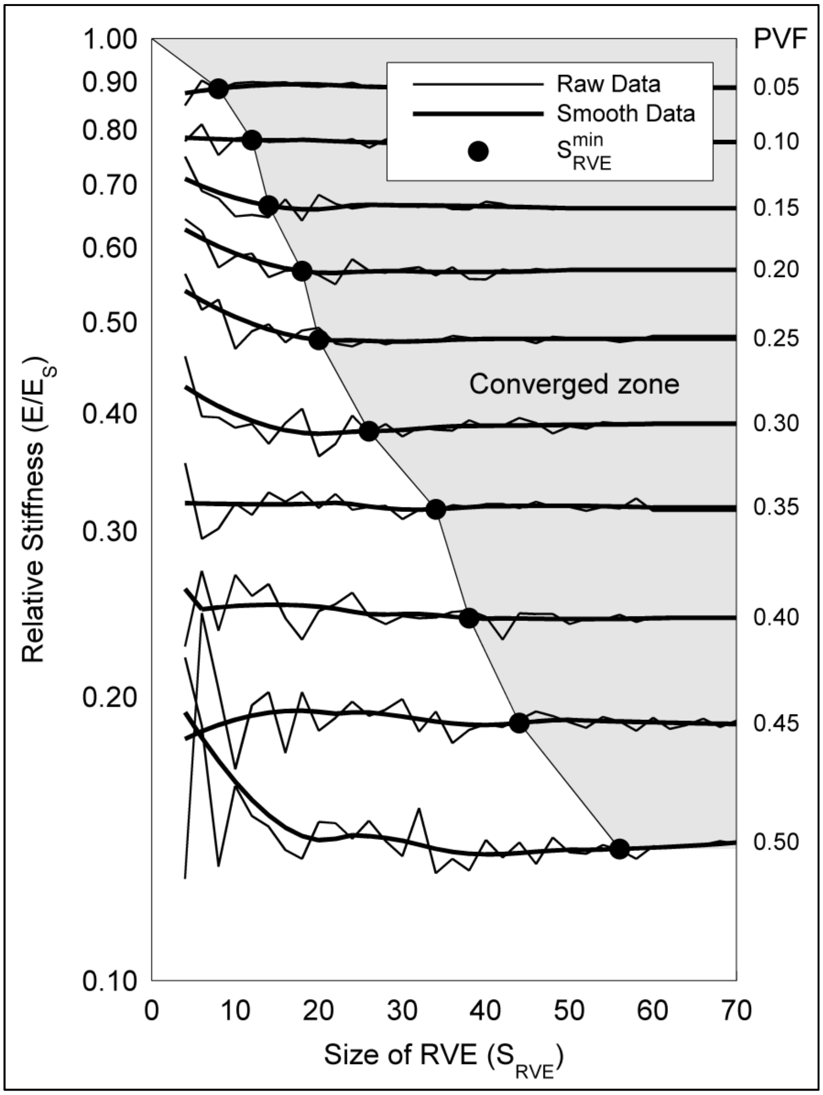

Figure 3.5 Convergence of the relative stiffness (E/E_S) as a function of S_{RVE} for a PVF ranging from 0.05 to 0.50.

Figure 3.6 plots the minimum size of an RVE (S_{RVE}^{min}, thick line) and the relative stiffness (E/E_S, dot marks) as functions of PVF. As expected, the higher the PVF, the lower the E/E_S, and the higher the S_{RVE}^{min}. Next, following the strategy adopted by Gibson et Ashby (1999), a scaling relation linking the pore volume fraction (PVF) to the relative stiffness (E/E_S) and based on a power law function, S_{RVE}^{min}, is also plotted in Figure 3.6 (thin line). The coefficients $C = 1.018$ and $n = 2.707$ ($R^2 = 0.999$) of the power-law function are determined using the non-linear least-square method (Maîtrejean, Terriault et Brailovski, 2013b). Such a scaling equation resulting from the mesoscale-level analysis (Figure 3.1b) allows us to establish a bridge between the mesoscale and macroscale levels, since it provides equivalent mechanical properties for the macroscale model (Figure 3.1a).

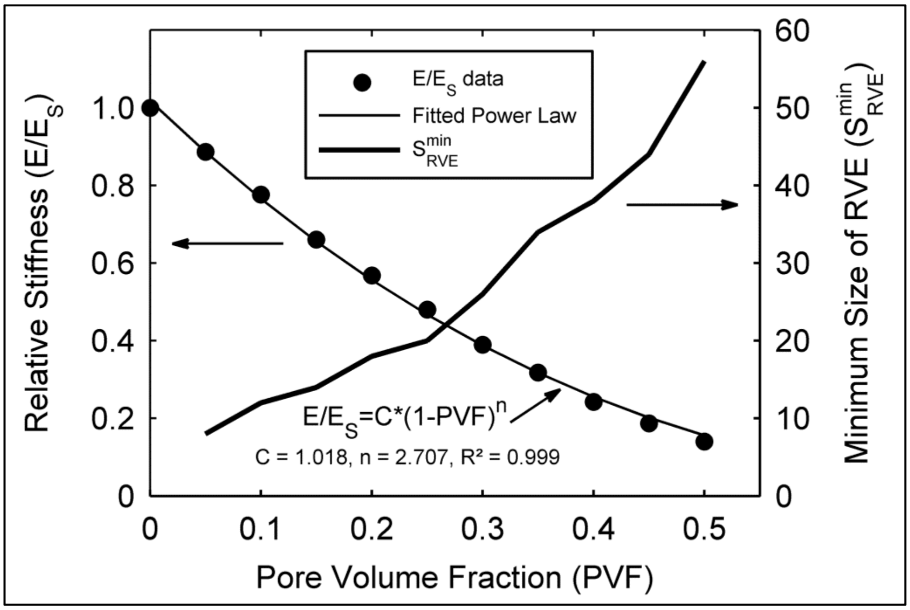

Figure 3.6 Evolution of the minimum size of an RVE (S_{RVE}^{min}) and of the relative stiffness (E/Es) as functions of porosity (PVF)

Note also that for manufacturing purposes, RVEs expressed in voxel should be converted into physical dimensions (millimeters), taking into account manufacturing-related limitations. In this work, this equivalence corresponds to 1 voxel = 0.35 mm (see detailed justification in Section 3.5.4).

To sum up, the results of these calculations are collected in Table 3.1, whose second and third columns contain values of S_{RVE}^{min} in voxels and mm. These physical dimensions are conservatively rounded up (last column of Table 3.1) to compensate for the randomness of the foam generation algorithm and are used to dimension the tensile specimens (see next section for more details). Note that a linear relation function of PVF was used when rounding: dimension (in mm) = 35 PVF + 1.75.

Table 3.1 Minimum size of RVE in voxel and millimeters

PVF	$\mathbf{S_{RVE}^{min}}$ **[voxel]**	**Conversion in [mm] (1 voxel = 0.35 mm)**	**Rounded up dimensions [mm]**
0.05	8	2.8	5.25
0.10	12	4.2	7.0
0.15	14	4.9	8.75
0.20	18	6.3	10.5
0.25	20	7.0	12.25
0.30	26	9.1	14.0
0.35	34	11.9	15.75
0.40	38	13.3	17.5
0.45	44	15.4	19.25
0.50	56	19.6	21.0

3.5.3.2 Specimens with target porosities and porosity gradient

For this work, three target porosities are selected, PVF = 0.30, 0.40 and 0.50, and two types of specimens, namely short (S) and long (L), are manufactured. These specimens (S30, S40, S50 and L40 in Figure 3.7) correspond to different PVFs (0.30, 0.40, 0.50 and 0.40, respectively), and therefore, possess different gauge dimensions: length = width = thickness = S_{RVE}^{min} (fourth column of Table 3.1). Their porosity decreases linearly by steps of 0.05 from the central porous gauge part to the fully dense grip part. The only difference between the short and the long specimens (S40 and L40) resides in the length of their porosity gradient zones. For the short specimens, this size is fixed at 10 voxels regardless of the porosity. For the long specimen, however, each part of an intermediate porosity (0.20, 0.25, 0.30 and 0.35) has a length corresponding to their respective Table 3.1.

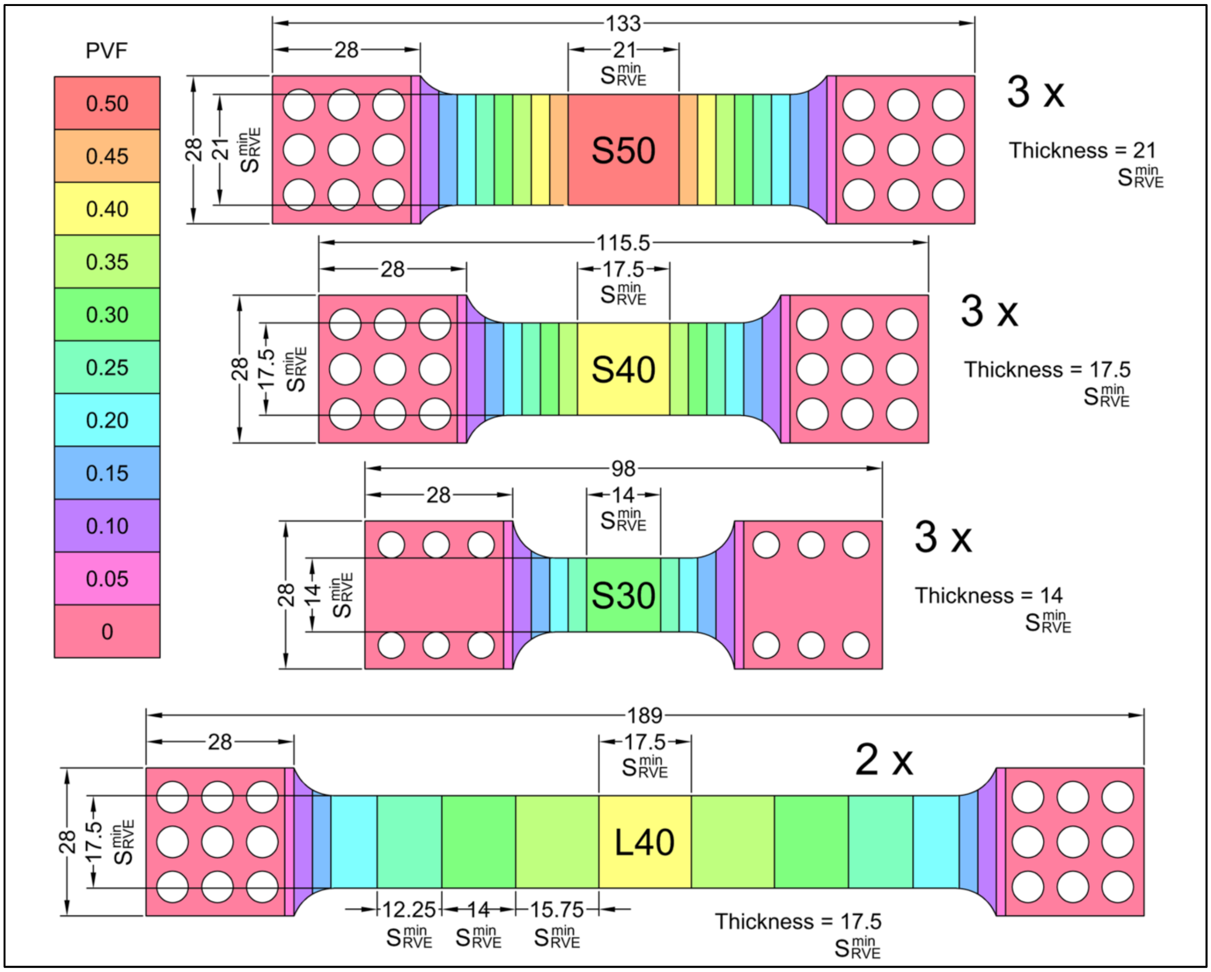

Figure 3.7 Dimension (mm) of the four specimens with the porosity gradient

To verify experimentally whether the randomness of the foam generation algorithm affects the results obtained with the RVE approach, three short specimens were generated for each porosity, by launching the morphology-generating algorithm three times. Given the randomness of the porosity generation algorithm, the morphology (structural organization) of each of the specimens of a given porosity was distinct. This procedure yielded specimens tagged S30(a,b,c) S40(a,b,c), and S50(a,b,c). Similarly, two randomly-generated, and therefore morphologically-distinct, long specimens were fabricated: L40(a,b). In addition, to characterize the bulk material, six fully dense 6 × 2 (mm) gauge cross-section, 25 mm-long specimens were produced.

3.5.4 Specimens manufacture

To manufacture tensile specimens, Selective Laser Melting (SLM) technology is used. This process is classified as a powder bed fusion additive manufacturing technology, where a laser beam selectively and fully melts metallic powder, thus generating layer-by-layer parts with complex thermal history due to the effects of rapid solidification, directional cooling and phase transformation (Frazier, 2014). Consequently, during their fabrication, the parts are built with thermally-induced residual stresses which may provoke warping (Kruth et al., 2004). Such effects are predominantly observed in large volume parts with high relative density (i.e., the fully dense grip sections of the specimens). In this work, to mitigate the risks of specimen warping, the fabrication supports at the specimen grip zones were reinforced, while their volumes were reduced by integrating in this specific zone a series of equally-distanced cylindrical holes (Figure 3.7).

In this study, SLM was performed using an EOSINT M 280 400 W Ytterbium fiber laser system, with EOS CobaltChrome (CoCr) MP1 powder (EOS GmbH, Munich, Germany). The fabrication parameter set supplied by EOS "MP1 Speed" was employed (50 μm layer thickness). Note that the tradename Direct Metal Laser Sintering (DMLS) is currently employed by EOS to describe their SLM process on an M 280 system.

Prior to the fabrication of the specimens, the minimum feasible physical size of an individual voxel was determined. To that end, RVEs with five different voxel sizes (1500, 1000, 500, 350 and 150 μm) were manufactured (Figure 3.8). From a simple visual inspection, it was possible to conclude that down-skin surfaces with a voxel size of 1500 μm collapsed (Figure 3.8a), while the pores were not clearly defined with a 150 μm voxel size (Figure 3.8e). Therefore, to minimize the specimen dimensions, an intermediate 1 voxel = 350 μm conversion factor was established (Figure 3.8d). Note that the fabrication parameter set provided by EOS and used to produce the parts included a specific exposure strategy for down-skin surfaces with a different hatching distance, scanning speed and laser power, in order to improve their surface finish.

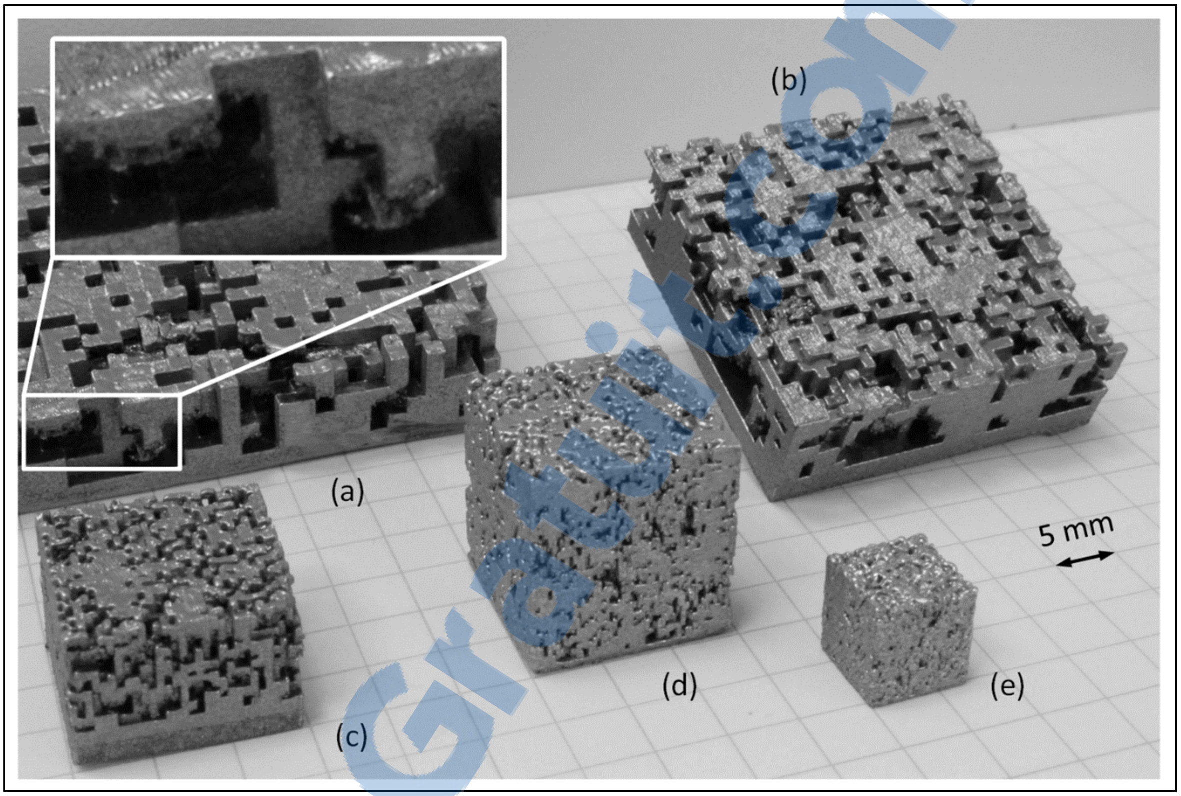

Figure 3.8 RVEs produced with different voxel sizes (in µm), PVF = 0.50: (a) 1500, (b) 1000, (c) 500, (d) 350 and (e) 150.

Figure 3.9a presents seven specimens (3 × S30, 3 × S50 and 1 × L40) built as part of this study. The build orientation (defined as the axis normal to the building platform) was kept perpendicular to the loading direction of the specimens (Figure 3.9a). For information purposes, the manufacture took approximately 50 h. Moreover, after the powder sieving-recycling process, a total of 5.4 kg of powder was estimated to be used, while the seven specimen weighted 2.4 kg, meaning that 55% of the powder was lost during SLM (machining allowances, fabrication supports, trapped powder, coarse and condensate particles, etc.).

To relieve the processing-induced residual stresses, an EOS-recommended heat treatment was carried out (1050 °C, 2 h, heating rate 10 °C/min) in the protective gas box of an N41/H furnace (Nabertherm GmbH, Lilienthal, Germany) with subsequent furnace cooling. The argon flow rates during preflush of the protective gas box, process and cooling were 25, 15 and

25 l/min, respectively. After heat treatment, the specimens were separated from the building plate by wire-cut electrical discharge machining (EDM) (Figure 3.9b).

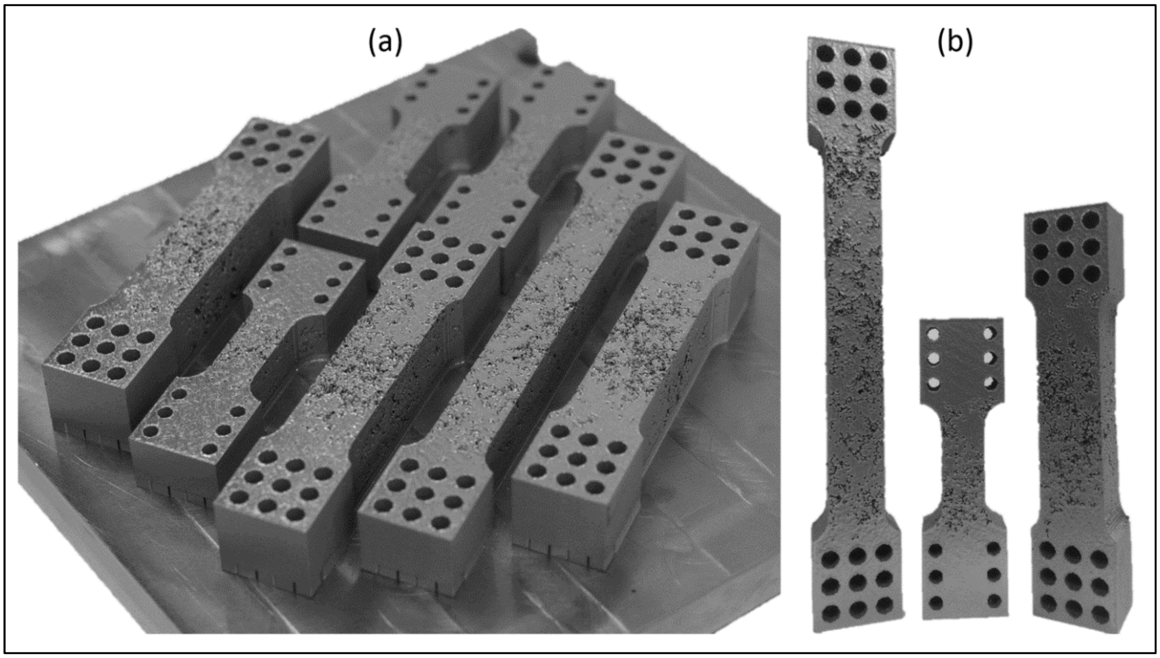

Figure 3.9 (a) Specimens on the building plate and (b) L40, S30 and S50 specimens, respectively.

3.5.5 Tensile testing

For tensile testing, an MTS 810 material testing system with a 500 kN load cell (Eden Prairie, MN, USA) was coupled with an ARAMIS 5M optical strain measurement system (GOM mbH, Braunschweig, Germany) (Figure 3.3j). ARAMIS 5M is a 3D digital image correlation (DIC) measuring system which uses a set of two cameras, but in this project, the system was employed in a 2D mode to measure a strain distribution on a plane face of a specimen. The system measuring area depends on the size of the calibration object. For short specimens, a 55 × 44 mm calibration object was selected. To maximize the measuring area in the case of long specimens, the field of view was doubled by placing two cameras side-by-side, with a certain overlap. Note that prior to testing, the surfaces of the specimens were prepared by applying a stochastic fine white spray pattern on a matte black background.

Testing at room temperature continued to the specimen failure, with a strain rate of $\dot{\varepsilon} = 0.001\ \text{s}^{-1}$. After testing, the “apparent stress-apparent strain” diagrams were built using forces measured by the MTS load cell (accuracy of ± 0.2 kN) and the longitudinal strains were measured by the ARAMIS 5M optical system (accuracy of ± 0.01%).

3.6 Results

The stress–strain responses taken from the central (gauge) section of 11 specimens are collected in Figure 3.10: (a) 3 × S30, (b) 3 × S40 and 2 × L40 (black- and grey-colored lines, respectively), and (c) 3 × S50. From each of these curves, four metrics are collected: Young's modulus (E), yield stress ($S_{Y\,0.1\%}$), ultimate strength (S_{UT}), and elongation at break (δ). A fifth metric, Poisson's ratio (ν), is additionally calculated using the DIC system. For a given specimen S30a, strain fields corresponding to an increasing apparent stress ($0.80S_Y$, S_Y and S_{UT}) are presented in Figure 3.10a. The strain fields taken from three distinct S50 specimens at their respective S_{UT} are compared in Figure 3.10c.

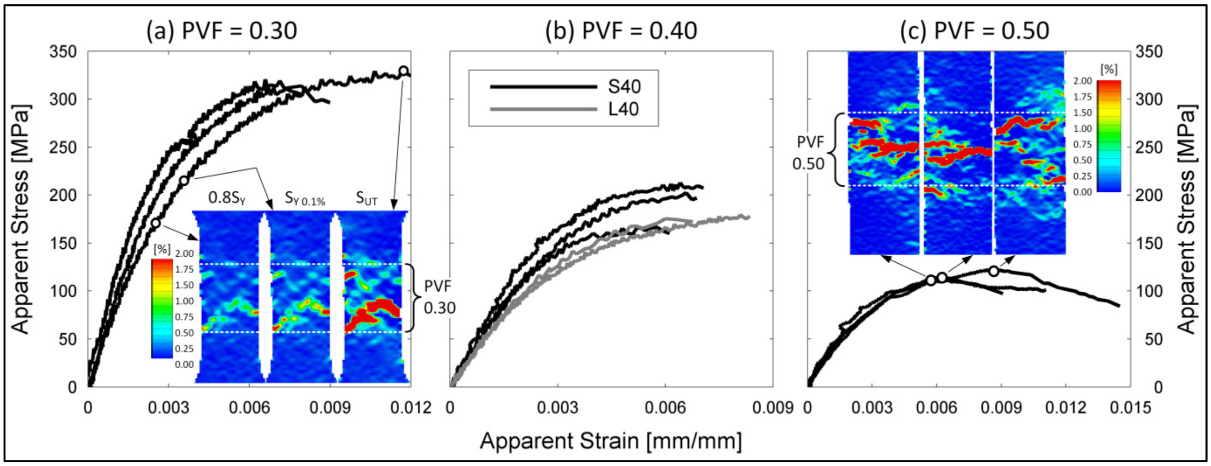

Figure 3.10 (a) Stress-strain diagrams for specimens S30a,b,c, and strain fields for specimen S30a at $0.80S_Y$, S_Y and S_{UT}, (b) stress-strain diagrams for specimens S40 and L40, and (c) stress-strain diagrams and strain fields at respective S_{UT} for specimens S50a,b,c

In addition to five metrics obtained from the gauge part of all the specimens, the long specimens allowed the measurement of Young's moduli and Poisson's ratios in their porosity gradient zones. Figure 3.11 presents the strain field of the L40 specimen at S_{UT} (a, b) and the stress-strain responses collected from the seven zones of the specimen (c), all tracked with ARAMIS. Note that the central gauge section was monitored with two overlapping cameras.

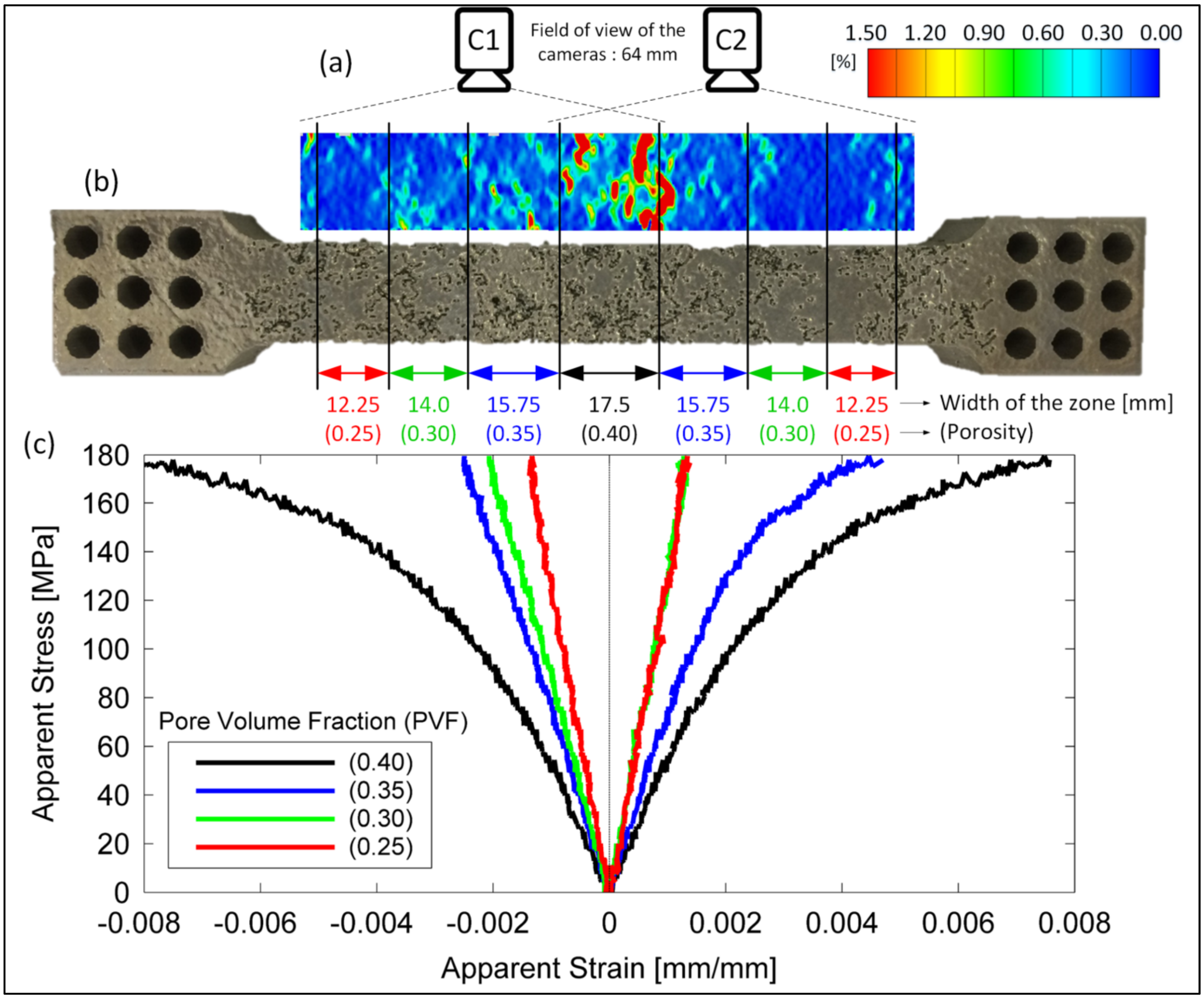

Figure 3.11 Specimen L40a: (a) geometry and camera setup, (b) strain field at S_{UT}, and (c) stress-strain diagrams plotted for each porous zone

Table 3.2 summarizes the metrics collected from the 11 porous and 6 fully dense (PVF = 0) tensile specimens, all manufactured and thermally treated using the same procedure. For each porosity, the total number of gauge sections combined from the short (S) and long (L) specimens is specified in Table 3.2. Note that it was not possible to determine S_Y and S_{UT}

values for PVF = 0.25 and 0.35 since these porosities were located in the porosity gradient zones, which did not fail during testing.

Table 3.2 Summary of the apparent mechanical properties

PVF	**Number of gauge sections**	**Young's modulus [GPa]**	**Poisson's ratio**	**Yield stress (Rp 0.10%) [MPa]**	**Ultimate tensile strength [MPa]**	**Elongation at break [mm/mm]**
0	6	219 ± 14 (E_S)	0.31 ± 0.02	741 ± 51	1121 ± 75	0.0318 ± 0.0083
0.25	4L	125 ± 9	0.29 ± 0.02			
0.30	4L + 3S	93 ± 7	0.27 ± 0.02	236 ± 20	322 ± 10	0.0098 ± 0.0024
0.35	4L	75 ± 6	0.23 ± 0.03			
0.40	2L + 3S	61 ± 6	0.23 ± 0.03	153 ± 20	187 ± 20	0.0070 ± 0.0009
0.50	3S	35 ± 2	0.23 ± 0.01	91 ± 3	116 ± 5	0.0115 ± 0.0027

By applying the scaling relation strategy to the results contained in Table 3.2, the experimental relative stiffness (E/E_S) is plotted in Figure 3.12a as a function of Pore Volume Fraction (PVF) (dot marks) and curve-fitted using the power law function with $C = 1.015$ and $n = 2.418$ (Figure 3.12a, thick line). The numerical E/E_S-PVF function taken from Table 3.1 is also plotted on Figure 3.12a (thin line) using an experimentally determined bulk Young's modulus of $E_S = 219$ GPa. In Figure 3.12b, the yield stress and the ultimate tensile strength taken from Table 3.2 are also drawn as functions of PVF.

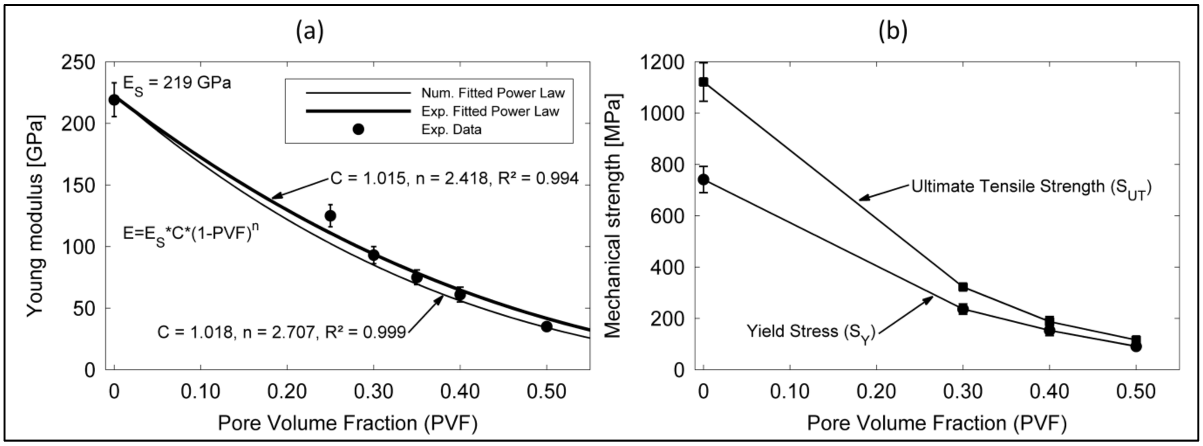

Figure 3.12 Metrics as a function of porosity: (a) experimental and numerical Young's moduli; (b) experimental yield stress and ultimate strength

3.7 Discussion

3.7.1 Scaling relations, experimental results and model validation

The power law-based scaling relation which links stiffness to the porosity of open-cell foams ($E/E_S = C(1\text{-}PVF)^n$) has been widely investigated (Campoli et al., 2013; Cheng et al., 2012; Horn et al., 2014; Murr et al., 2010a; Ramirez et al., 2011). In these works, where both stochastic and ordered porous metallic structures with medium-to-high porosity (PVF > 0.50) were produced by EBM, the porosity-related exponent coefficient “n” varied from 1.9 to 2.4. In our study, the experimental and numerical values of the artificially generated stochastic structures with low-to-medium porosity (PVF < 0.50) were slightly higher (2.42 and 2.71, respectively).

While the experimental and numerical results of this study correlate satisfactorily (Figure 3.12a), differences exist between the literature data and the results of the present work, and this discrepancy may be due to the difference in the studied porosities. This assertion is supported by the observations by Maîtrejean et al. (2014) that the lower the range of porosity, the higher the value of the exponent coefficient. Moreover, Ramirez et al. (2011) found that stochastic foams led to higher values of the exponent coefficient, as compared to unit-cell structures.

According to Gibson et Ashby (1999), Poisson's ratio (ν) of foams is independent of porosity, and ranges around 0.30. However, in this work, we noticed a slight decrease of ν as the PVF increased (Table 3.2). To clarify the causes of this phenomenon, a more in-depth study will be conducted in a separate work.

For the majority of experimental studies conducted on tensile (Aly, 2010; Imwinkelried, 2007; Maskery et al., 2015; Michailidis et al., 2008) and flexural (Horn et al., 2014) tests of open-cell porous metallic structures, an elastic-brittle behavior which can be associated with morphology-related stress concentrations (Gibson et Ashby, 1999) was observed. In this study, however, an apparent plastic yield precedes the non-ductile fracture of the specimens (Figure 3.10), which represents a positive feature since it can prevent drastic failure.

Another cause of a significant brittle foam behavior observed in this study ($\delta \sim 0.01$ regardless of the porosity) can be attributed to a relatively low ductility of their similarly-processed bulk counterparts ($\delta_S \sim 0.03$). In this respect, on the margin of our study, an additional EOS-recommended softening heat treatment (6 h at 1150 °C) was carried out on the SLM-built bulk tensile specimens resulting in a five-fold ductility increase ($\delta_S \sim 0.15$ compared to ~ 0.03). It is reasonable to assume that the application of such a thermal treatment might mitigate, to a certain extent, the negative impact of morphology-related stress concentrations on the mechanical behavior of our structures (hypothesis to be verified). Moreover, according to EOS, this heat treatment has a homogenizing effect reducing specimens' anisotropy.

3.7.2 Morphology-generation algorithm and porosity gradient

For the 0.30-0.50 porosity range, the minimum gauge sizes of the specimens (S_{RVE}^{min}) were numerically established, and the stress-strain diagrams collected from these gauge sections were found repeatable (Figure 3.10). Moreover, although the strain fields of three S50 specimens at S_{UT} differed (Figure 3.10c), the average strain distributions along the specimens' longitudinal axes were very close. On the other hand, stress-strain diagrams obtained from the left and right sides of the central porous gauge zone of the long specimens were not identical

(Figure 3.11). Such a disparity can be caused by two main factors: the randomness of the porosity generation algorithm and the variation in the material properties and experimental conditions. The second factor can be predominant since the standard deviations of the metrics of Table 3.2 are in the same range of values, for both the porous and the fully dense specimens.

The porosity gradients used in the specimen design improved the study outcome on two levels: manufacturing and testing. From a manufacturing perspective, without the porosity gradient (i.e., in the case of a direct connection of the porous gauge section to the fully dense grip section), high thermal stresses induced by SLM could have resulted in cracks between zones with radically different relative densities, as was already mentioned by Hazlehurst (2014). From a testing perspective, the tensile characterization of long specimens with porosity-gradient zones of representative length ($\mathrm{S}_{\mathrm{RVE}}^{\mathrm{min}}$) allowed the collection of elastic constants (Young's modulus and Poisson's ratio) not only from the central (gauge) zone, but also from the neighboring gradient porosity zones that connects the gauge and the grip parts of the specimens. As well, for both the short and the long specimens, the porosity gradient ensured that the specimens systematically failed within the gauge zone.

We also noted that the stiffness and the mechanical strength of the long specimens were systematically lower than those of the short specimens (S40 and L40 in Figure 3.10b). Since both short and long specimens contained the same mechanically-representative gauge sections, the observed differences can be attributed solely to the differences in their porosity gradient zones. In fact, we observed that the stiffnesses of the narrow porosity gradient zones of the S40 specimens were slightly higher than those of the representative-length porosity gradient zones of the L40 specimens (results not shown). Such a tendency was also observed during our numerical study: as can be seen in Figure 3.5, for a given porosity, the higher the $\mathrm{S}_{\mathrm{RVE}}$, the lower the $\mathrm{E}/\mathrm{E}_{\mathrm{S}}$ all throughout the convergence study. Therefore, the stiffer porosity gradient zones of the short specimens might create edge effects leading to stiffening of their neighboring gauge sections.

3.7.3 Medical applications

In our previous study (Simoneau et al., 2014), we established that the optimum pore size for bone ingrowth (50-800 µm) was reached when the porosity varied between 0.30 and 0.50 with a voxel size of 36 µm. However, this voxel size is one order of magnitude smaller than the minimum achievable by SLM (350 µm). Such a technological limitation was also raised by Horn et al. (2014) and may narrow the field of application of metal AM in the biomedical domain.

Furthermore, the CoCr foams characterized in this work can hardly meet the mechanical requirements of the application, given that the stiffness of human cortical bone ranges between 5 and 30 GPa (Currey, 2012), and that for a stiffness of 18 GPa, the bone yields at about 150 MPa (Hansen et al., 2008). In fact, for a PVF < 0.40, the mechanical strength of our foams is sufficiently high (S_Y > 150 MPa), but the corresponding stiffness is too high (E > 60 MPa), whereas for a PVF of 0.50, the foam stiffness is closer to that of cortical bone (E = 35 MPa), but the corresponding mechanical resistance becomes dangerously low (S_Y = 90 MPa). The use of titanium alloys, such as Ti-6Al-4V, or near-beta metastable Ti-based shape memory alloys (Brailovski et al., 2011), would enable much better biomechanical compatibility, since for the same level of mechanical resistance as CoCr alloys, titanium alloys provide much greater compliance.

A vibrating table and compressed air were employed to remove powder from the porous specimens. Although it was not possible to confirm that no powder was left, we can assert that the testing results were not impacted by this factor due to the nature of the mechanical test (uniaxial tension). However, a computed tomography inspection would be relevant to provide insights about the internal morphology of the porous structure (ongoing work).

Considering that the hip joint should withstand around 1.1 million gait cycles every year (Morlock et al., 2001), the fatigue behavior of such additively-manufactured porous metallic structures intended for orthopedic application must be inevitably analyzed. However, only few studies have been conducted on this topic (Amin Yavari et al., 2015; Brenne, Niendorf et Maier, 2013; Lipinski, Barbas et Bonnet, 2013; Mullen et al., 2010). In these studies, the fatigue strength has been found to decrease with increasing porosity, following the same trend observed in static tests. On the other hand, when normalizing the fatigue stress amplitude to the yield or ultimate stress of foams, no significant influence of the porosity was noticed (Amin Yavari et al., 2015; Ashby et al., 2000). The post-processing of SLM porous structures, namely heat treatment (Brenne, Niendorf et Maier, 2013) and surface finish (Lipinski, Barbas et Bonnet, 2013), can also impact on fatigue life. Finally, Mullen et al. (2010), who studied the fatigue resistance of stochastic SLM-manufactured porous titanium, demonstrated that stochastic architecture of porous materials, which mimics the random architecture of trabecular bone, could be beneficial from the fatigue resistance point of view. This last conclusion allows us to hypothesize that our stochastic voxel-based porous structures could be suitable for the load-bearing implant applications: validation of this hypothesis is part of our current work.

3.8 Conclusion

The objective of this work was to develop a methodology for the design, manufacture and tensile testing of stochastic porous open-cell structures for biomedical applications. First, the morphology of the porous tensile specimens was generated using an original algorithm. Then, the dimensioning of the tensile specimens was accomplished by combining the Representative Volume Element (RVE) approach with the Finite Element (FE) methods. As expected, higher porosities led to larger porous gauge sections. Moreover, a decreasing porosity gradient was employed to avoid discontinuities between the porous gauge section and the fully dense grips of the tensile specimen.

Following their design, a total of 11 tensile specimens with different lengths and gauge porosities (0.30, 0.40 and 0.50) were produced using the Selective Laser Melting (SLM) Additive Manufacturing (AM) technology, and mechanically characterized in tension up to failure. Compared to the short specimens, the long specimens possessed porosity gradient zones of representative size ($\mathrm{S}_{\mathrm{RVE}}^{\mathrm{min}}$), allowing the collection of their elastic constants (Young's modulus and Poisson's ratio). The experimental apparent Young's moduli correlated with these values obtained numerically (FE), as well as with the power law scaling relations found in the literature. Numerical studies are currently ongoing to evaluate the foam's behavior beyond the elastic limit since the numerical model of this study was limited to small deflections. Finally, since medical applications are the main focus of such porous structures, the use of titanium alloys with lower stiffness should be considered to enhance their biomechanical compatibility.

3.9 Acknowledgments

The authors would like to credit the Fonds de développement de l'ÉTS (FDETS), Fonds de recherche du Québec – Nature et Technologies (FRQ-NT) and the Natural Sciences and Engineering Research Council of Canada (NSERC) for their financial support.

Computations were conducted on the Guillimin supercomputer from McGill University, managed by Calcul Québec and Compute Canada. The operation of this supercomputer is funded by the Canada Foundation for Innovation (CFI), NanoQuébec, RMGA and the Fonds de recherche du Québec – Nature et Technologies (FRQ-NT).

Furthermore, the authors express their gratitude to V. Urlea for its assistance in laboratory experiments and to T. Zhang for its support the development of the numerical models.

CHAPITRE 4

DEVELOPMENT OF A POROUS METALLIC FEMORAL STEM: DESIGN, SIMULATION, MANUFACTURE AND MECHANICAL TESTING

Charles Simoneau, Patrick Terriault, Bruno Jetté, Mathieu Dumas, Vladimir Brailovski

Département de génie mécanique, École de technologie supérieure,
1100, rue Notre-Dame Ouest, Montréal, Québec, Canada H3C 1K3

Article accepté dans la revue « Materials & Design » le 19 octobre 2016

4.1 Avant-propos

Les deux premières parties du projet ont permis d'obtenir respectivement les propriétés morphologiques et mécaniques des mousses générées par l'algorithme de génération en plus de développer un modèle éléments finis. Dans la troisième et dernière partie du projet, ces résultats sont utilisés pour développer une tige fémorale intégrant une structure poreuse métallique créée par l'algorithme de génération. Encore une fois, une approche fondée sur le développement d'un modèle numérique et suivie d'une validation expérimentale est présentée.

4.2 Résumé

Cet article présente les travaux qui ont mené au développement d'une tige fémorale biomimétique poreuse conçue pour réduire le phénomène de déviation de contrainte et pour offrir une meilleure stabilisation initiale de l'implant au moyen de la croissance osseuse. La conception de la tige commence par la construction d'un diagramme permettant d'établir une relation entre les exigences fonctionnelles pour la croissance osseuse et les limitations technologiques de la fusion sélective sur lit de poudre. Ce diagramme est ensuite utilisé pour déterminer le niveau de porosité optimale (33 %) de la structure poreuse constituant la tige fémorale. Ensuite, la fabrication additive métallique est utilisée pour la mise en forme de la tige poreuse ainsi que d'une autre tige complètement dense. La méthode des éléments finis et une approche d'homogénéisation numérique sont utilisées afin de prédire la réponse

mécanique de la tige fémorale. Des conditions de chargement statique fondé sur la norme ISO 7206-4 (2010) sont ensuite adoptées afin d'évaluer le comportement mécanique de chaque tige. Puis, la technique de corrélation d'image numérique est employée pour obtenir les champs de déplacement et de déformation durant les essais mécaniques ainsi que pour la validation du modèle éléments finis. Dans un premier temps, une réduction de la rigidité d'environ 40 % est observée entre la tige dense et poreuse et dans un deuxième temps, les résultats associés au modèle numérique de la tige dense et poreuse surestiment les résultats expérimentaux de 6 et 37 % respectivement. La divergence des résultats au niveau de la tige poreuse a été attribuée à l'écart entre la porosité ciblée par le modèle numérique (33 %) et la porosité réellement obtenue suite à la fabrication (42 %).

4.3 Abstract

This paper focuses on the development of a porous metallic biomimetic femoral stem designed to reduce stress shielding and to provide firm implant fixation through bone ingrowth. The design of this stem starts with the creation of the diagram allowing the establishment of a relationship between the bone ingrowth requirements and the metal additive manufacturing technology limitations. This diagram is then used to determine the optimum porosity (33%) that should compose the porous part of the stem. Afterward, selective laser melting is used to manufacture the porous stem altogether with its fully dense replica. Finite element analysis and numerical homogenization methods are then employed to predict the mechanical behavior of the stem. Both stems are finally tested following the ISO 7206-4 (2010) requirements under static loading conditions. The digital image correlation technique is employed to obtain the displacement and strain fields during the tests, and to validate the finite element model. While the finite element model of the dense stem has been successfully validated, that of the porous stem has shown ~40% higher stiffness than that measured experimentally. It has been proven that this discrepancy is due to the difference between the experimentally-measured (42%) and the numerically-targeted (33%) porosities.

4.4 Introduction

In orthopedics, porous metallic biomimetic implants are of particular interest since they can advantageously be used for the replacement of damaged bones. Stress shielding resulting from the stiffness mismatch between the implant and bone tissues can be reduced with these implants, since their stiffness can be adjusted to match that of bone by controlling the implant porosity. Bone resorption leading to risks of implant aseptic loosening or bone failure may then be reduced (Gibson, Ashby et Harley, 2010). The possibility of bone ingrowth also constitutes a promising feature of such porous constructs since it ensures their firm fixation in the implantation site (Fujibayashi et al., 2004).

Specific mechanical and biological requirements must be fulfilled for employing porous materials as orthopedic implants. From the biological point of view, an open-cell porous structure with pore sizes ranging from 50 to 800 μm should be targeted to favor bone ingrowth (Bobyn et al., 1980; Bragdon et al., 2004; Lefebvre, 2013). Furthermore, based on the human bone data, porosity of the porous structure should range between 30 and 50%, to maximize the surface-to-volume ratio of the porous structure, and, therefore, to promote bone remodeling (Beaupré, Orr et Carter, 1990; Coelho et al., 2009; Martin, 1984). A high surface-to-volume ratio will also enhance cell attachment, growth, and migration (Leong, Cheah et Chua, 2003; Min et al., 2004). From the mechanical point of view, the stiffness and strength of porous metallic implants should respectively be similar and higher than those of surrounding bone. A reduced stiffness mismatch will alleviate the stress shielding effect, while a higher mechanical resistance of the implant will prevent its failure before that of bone. However, increasing the implant porosity to enhance its compliance may negatively impact its mechanical resistance, and thus its fatigue life (Li et al., 2012; Spoerke et al., 2005). Such a concern is of an extreme importance for load-bearing implants: a hip implant, for example, should withstand over 1 million gait cycles every year (Morlock et al., 2001).

In recent years, advances in metal additive manufacturing (AM) technologies have led to the development of numerous porous metallic constructs for orthopedic applications (Ahmadi et al., 2015; Campoli et al., 2013; Hazlehurst, Wang et Stanford, 2013; Hedayati et al., 2016; Heinl et al., 2008; Horn et al., 2014; Khanoki et al., 2016; Parthasarathy, Starly et Raman, 2011; Petit et al., 2016; Roy et al., 2016; Yan et al., 2015). In these studies, as in many others, electron beam melting (EBM), laser engineered net shaping (LENS^{TM}) and selective laser melting (SLM) technologies were used to manufacture complex porous structures from biocompatible metals and their alloys (CoCrMo, Ti-6Al-4V and TiCp). Modeling and characterization of these porous structures revealed that, depending on the specimen porosity, their stiffness can be adjusted to match that of either trabecular or cortical bone. Moreover, various numerical models of such porous structures have been developed to solve a multi-objective optimization problem originating from the previously mentioned concurrent biomechanical requirements (Ahmadi et al., 2015).

While in the majority of the above-mentioned publications, the external shape of the studied porous structures was limited to cuboid or cylinder, a limited number of research groups targeted complex orthopedics implants, thus trying to take full advantage of additive manufacturing technologies (Bandyopadhyay et al., 2008; Harrysson et al., 2008; Hazlehurst, Wang et Stanford, 2014; Murr et al., 2010b). Among these, Harrysson et al. (2008) and Hazlehurst, Wang et Stanford (2014) used EBM/Ti-6Al-4V and SLM/CoCrMo, respectively, to produce porous femoral stems and their fully dense replicas. The mechanical response of the stems was evaluated using flexural testing. While a rhombic dodecahedron lattice structure with a cell size of 3 mm was selected by Harrysson et al. (2008) to fill the body of the porous stem, the stem concept of Hazlehurst, Wang et Stanford (2014) contained a porous body based on a cubic lattice structure surrounded by a dense outer shell.

Both above-mentioned stems showed reduced weight (44-48%) and flexural stiffness (57-60%), when compared to their dense counterparts. The limitation of the first concept (Harrysson et al., 2008) resides in the fact that the proposed 3 mm cell size lattice structure offers a pore size that by far exceeds the maximum 800 μm recommended for bone ingrowth. On the other hand, the second concept (Hazlehurst, Wang et Stanford, 2014) does not offer bone ingrowth capabilities at all since its porous structure is entirely surrounded by a dense outer shell. In both cases, the amplitude and direction of the load applied to the stems during their flexural testing were not biomechanically representative of service conditions of such implants, which undermine the validity of these testing protocols.

The main objective of this study is to design, manufacture, simulate and test a porous metallic biomimetic femoral stem with the potential of reduced stress shielding and improved bone ingrowth. To provide representative and reproducible biomechanical testing conditions, the biomechanically-representative ex-vivo testing methodology of this study is based on the ISO 7206-4 (2010) guidelines.

The design methodology of this study is established in Section 4.5.1, where bone ingrowth requirements, limitations of AM technology and porosity-dependent mechanical properties are concurrently considered to define the characteristics of the porous zone of the stem. Then, the AM of the porous and dense femoral stems is discussed in Section 4.5.2. Based on a common testing protocol, the numerical and experimental testing strategies are presented in Section 4.5.3. Finally, the numerical and experimental results are presented in Sections 4.6, and then discussed in Section 4.7.

4.5 Methodology of the porous stem development

Figure 4.1 depicts a process workflow detailing the methodological approach used in this work for porous stem development. It begins with the design of the porous stem followed by its additive manufacturing. Numerical and experimental tests are then carried out to assess the mechanical performances of the stem. Finally, the numerical model of the stem is validated.

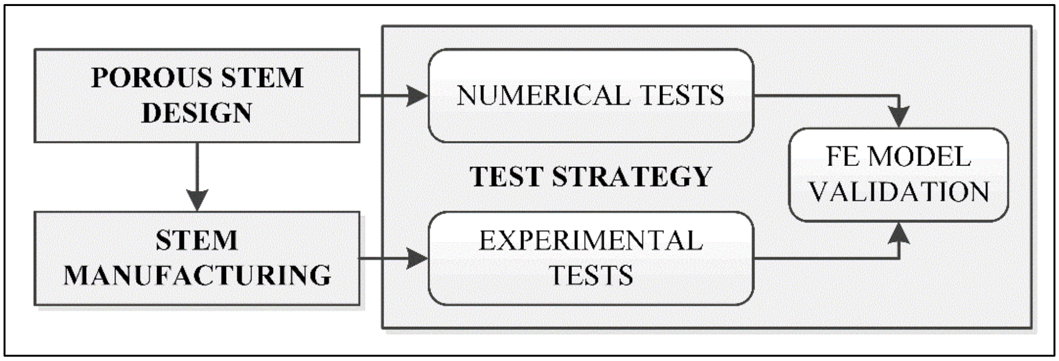

Figure 4.1 Process workflow depicting the complete methodological approach

4.5.1 Design of the porous stem

4.5.1.1 Identification of the dense and porous zones of the stem

The design of the porous stem starts with a Stryker “SECUR-FIT™ Max” femoral stem - model 6052 0830A (Stryker Corporation, MI, USA) (Figure 4.2a). Reverse engineering methods are then employed to obtain the CAD model of this stem, as well as its specific design features, such as a threaded hole for installation/extraction purposes, and a smooth tapered distal tip for insertion into the medullary cavity of the femur. A femoral head is also added to the stem design (Figure 4.2b).

In this study, this reverse-engineered fully dense stem replica will be used for reference purposes (benchmark testing), while providing a geometrical envelope for the design of the new porous stem. To maximise the volume occupied by the porous structure in the new stem design, the distal tip is hollowed out to form a dense shell, and only a thin wall is kept around the threaded hole. Moreover, the head and neck regions of the stem are also kept dense to ensure an adequate load transfer during testing (Harrysson et al., 2008). Additionally, two dense strips joining the distal shell and the neck region are added on the medial and lateral planes of the stem, leaving two openings on its dorsal and ventral planes, where a porous structure will be accessible for bone ingrowth (Figure 4.2c). While these strips increase the global stiffness of the stem, they are required to reduce stress concentration at the interface of the porous structure with the dense distal shell, and, therefore, reduce the risk of premature stem failure (preliminary results validated with FE simulations). Finally, the remaining volume is filled with a porous structure (Figure 4.2c). In the framework of this project, a custom MATLAB 2015b (MathWorks Inc., Natick, MA, USA) routine is used to generate stochastic open-cell porous structure of a specific porosity within a voxelized domain, corresponding to the porous zone of the stem design (refer to Appendix A (Section 4.10) for more details about the algorithm).

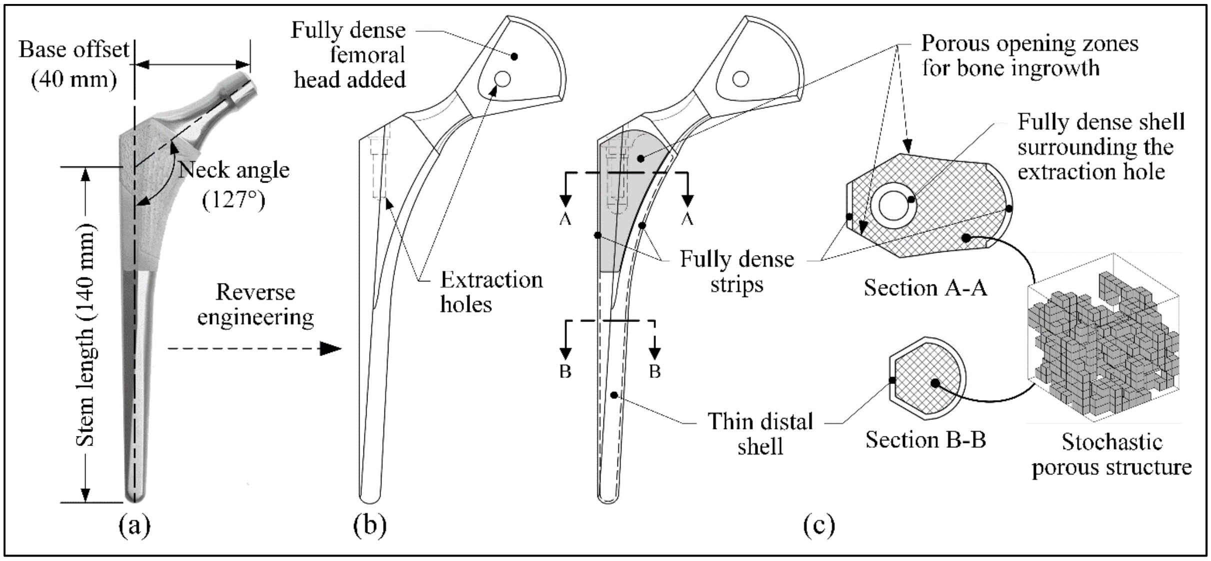

Figure 4.2 (a) Commercial dense stem, (b) Reverse-engineered dense stem, and (c) Porous stem (dense and porous material zones identification)

4.5.1.2 Structural requirements for bone ingrowth, manufacturing limitations and porosity-dependent mechanical properties

The realization of porous structures shown in Figure 4.2c may be difficult to achieve, when trying to fulfill the conflicting structural requirements for bone ingrowth in terms of pore size and porosity, and the technology limitation in terms of physical size of a smallest individual voxel that can be practically manufactured (Simoneau, Brailovski et Terriault, 2016). To assist in the selection of an adequate porosity value, Khanoki et al. (2016) proposed an intuitive chart for the design of ordered porous structures respecting simultaneously the bone ingrowth requirements (i.e. pore size and porosity) and the SLM manufacturing limitations (i.e. strut size). (Note also that the selected structure should also be capable of supporting service loading, without failure).

In this work, a similar chart is presented to provide the design space diagram combining the biological and technological requirements for the voxel-based stochastic porous structures generated by the morphology modeling algorithm. In this context, the evolution of a median equivalent pore size (d_{50}) as a function of pore volume fraction (PVF or porosity) for a voxel size (α) varying from 50 to 350 µm is presented in Figure 4.3a (see Appendix A (Section 4.10) and Simoneau et al. (2014) for more details about the morphology of the porous structures). Then, the delimitation of the optimum pore size for bone ingrowth is represented by two horizontal lines at $d = 50$ and 800 µm. Since it was previously demonstrated that the minimum voxel size achievable with SLM (EOSINT M 280, Ti64 powder) is ~200 µm, the design space is established (see hatched area in Figure 4.3a) within which a design point corresponding to the maximum achievable porosity is selected (~33% see dot mark in Figure 4.3a).

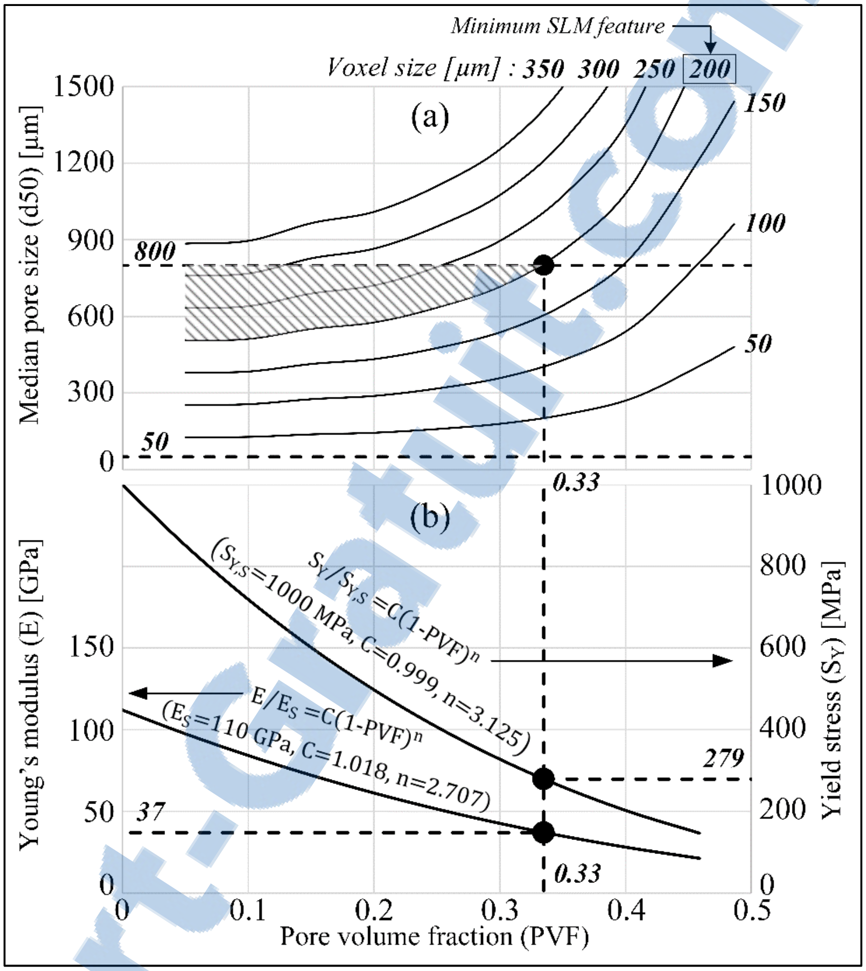

Figure 4.3 (a) Design space diagram based on a combination of bone ingrowth requirements and SLM limitations, and (b) Young's modulus and yield strength of a given porous structure as a function of pore volume fraction (PVF)

Scaling relations based on the $P/P_S = C(1\text{-}PVF)^n$ power law are frequently used to calculate an apparent property (P) of a porous body characterized by a given pore volume fraction (PVF), starting from its fully dense (solid) property (P_S) (Gibson et Ashby, 1999). In this equation, C and n are the coefficients to be determined analytically, experimentally or numerically.

In this work, such scaling relations for the Young's modulus (E) and yield stress (S_Y) were adapted from the previous study (Simoneau, Brailovski et Terriault, 2016) and plotted in Figure 4.3b (refer to Appendix A (Section 4.10) for more details). The bulk Young's modulus

($E_S = 110$ GPa) and yield stress ($S_{Y,S} = 1000$ MPa) were experimentally measured for Ti-6Al-4V for the benefit of this study. From this graph, a 33% porous structure should manifest an apparent Young's modulus of $E = 37$ GPa and an apparent yield stress of $S_Y = 279$ MPa.

Note that this level of material properties globally respects the aforementioned biomechanical requirements for a metallic implant material, since the Young's modulus of human cortical bone ranges from 5 to 30 GPa (Currey, 2012) and the yield stress of human femoral cortical bone is close to 150 MPa (Hansen et al., 2008). Consequently, the femoral stem of this study will be filled with a 33% porous structure having a voxel size of 200 µm.

4.5.2 Fabrication of the porous stem

4.5.2.1 Data preparation for selective laser melting additive manufacturing

Data preparation for SLM starts from the voxelization of the porous zone of the stem (Figure 4.2c), with a voxel size of 200 µm (MATLAB function (Aitkenhead, 2013), MATLAB Central File Exchange). A porosity of 33% is then imposed on the morphology modeling algorithm (Section 4.5.1.1) in order to generate the porous structure of the femoral stem. Afterward, the resulting geometry is converted into an STL file (MATLAB function (Holcombe, 2008), MATLAB Central File Exchange). Then, a Boolean union operation is performed in MAGICS 17.02 (Materialise, Leuven, Belgium) to merge the porous and the dense bodies and to create a single STL file. Note that the dense part of the stem comprises the thin distal shell, femoral neck and head, and strips (Figure 4.2b). Next, the Support Generation Module of MAGICS is used to orient the part and to generate the fabrication support structures linking the samples to the SLM machine building plate. The build orientation, defined as the axis normal to the building platform, is kept perpendicular to the flat surface located on the lateral plane of the stem (Figure 4.4a).

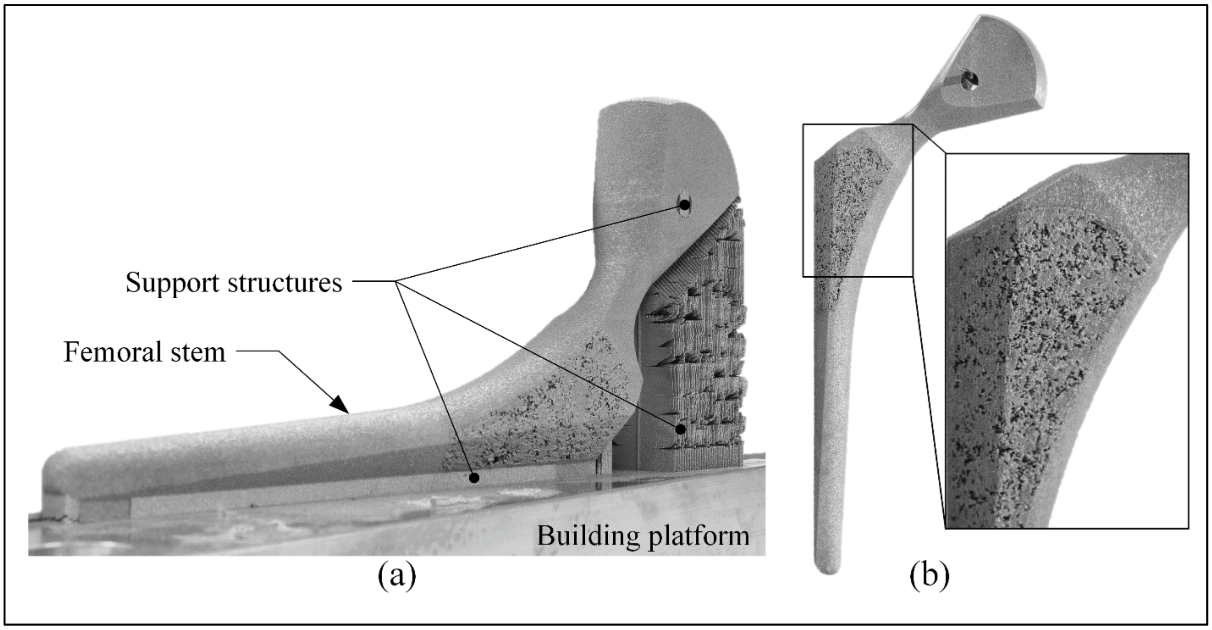

Figure 4.4 (a) Porous femoral stem on the building platform, (b) Post-processed femoral stem

4.5.2.2 Manufacturing and post-processing of the stems

One porous femoral stem and one dense replica were manufactured using an EOSINT M 280 400 W Ytterbium fiber laser system, with EOS Titanium Ti64 powder (EOS GmbH, Munich, Germany). The fabrication parameter set supplied by EOS "Ti64 performance" was employed (30 µm layer thickness).

To relieve the processing-induced residual stresses, the EOS-recommended heat treatment was carried out (800 °C, 4 h, 10 °C/min heating rate) in the protective gas box of an N41/H furnace (Nabertherm GmbH, Lilienthal, Germany), with subsequent furnace cooling. The argon flow rates during preflush of the protective gas box, process and cooling were 25, 15 and 25 l/min, respectively. Before heat treatment, a vibrating table and compressed air were employed to remove powder from the specimens. Then, the stems were separated from the building plate using a band saw and micro-blasted in a Peenmatic 750 S cabinet with aluminum oxide media (IEPCO AG, Höri, Switzerland). Figure 4.4a presents the porous stem immediately after SLM (a) and post-treatments (b). Note that the fully dense tensile specimens employed to characterize the material properties of the bulk alloy were also selectively laser-melted using the same protocol.

4.5.3 Numerical analysis and experimental testing

4.5.3.1 Testing guidelines

In this study, a standard ex vivo testing methodology based on the ISO 7206-4 (2010) guidelines was adopted to evaluate the mechanical response of the stems from numerical and experimental points of view. The standard describes a test method for determining the endurance properties of femoral stems partially embedded in a solid medium. Although only static testing is realized in the framework of this project, the ISO standard provides specific testing information and requirements, such as the solid medium, the length of the free end, the stem ventral and lateral plane orientations with respect to the global reference system of the testing bench, etc. (Figure 4.5).

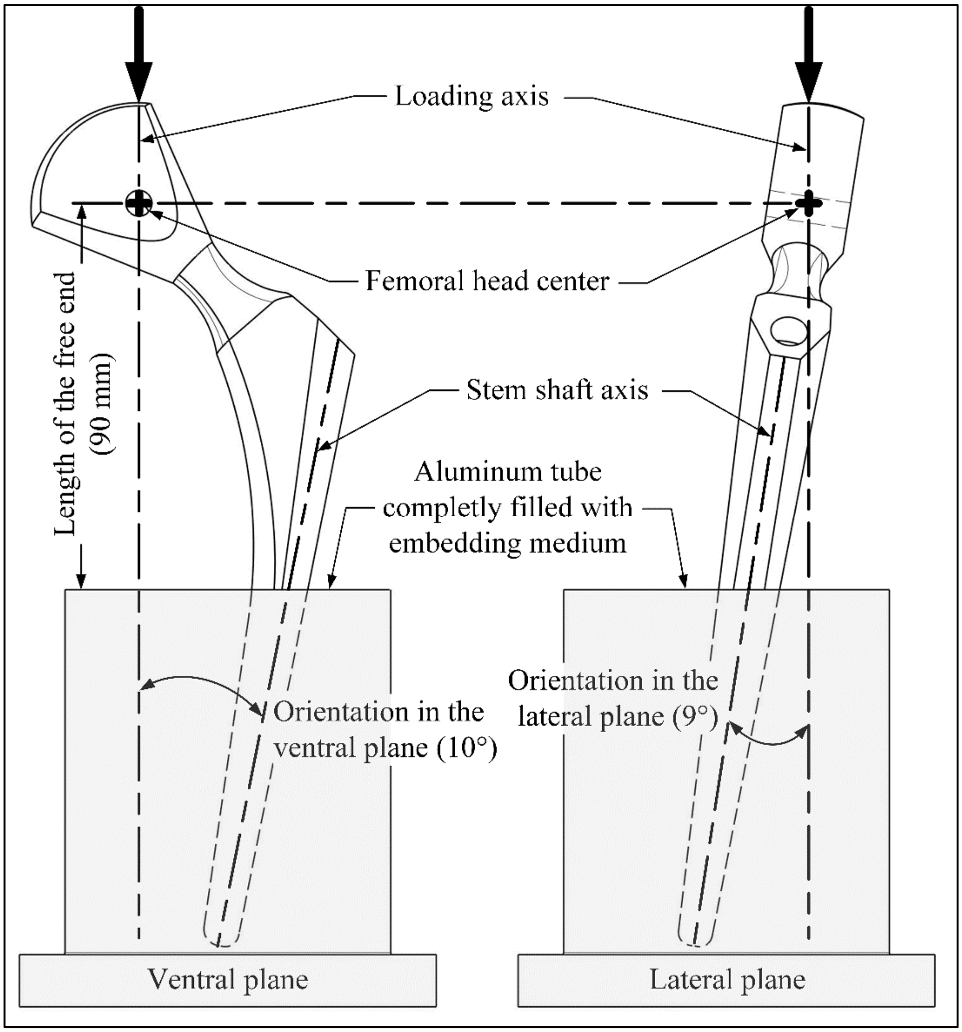

Figure 4.5 Testing setup respecting the ISO 7206-4 (2010) guidelines

4.5.3.2 Numerical analysis

A three-dimensional (3D) finite element model is built to predict the mechanical response of the porous stem. However, the explicit representation of the morphology of the porous structure in such simulation is prohibitive from computational memory and time viewpoints. The reason for this difficulty is the presence of a large gap between the length scale of an implant (mm) and that of a pore (µm) (Maîtrejean, Terriault et Brailovski, 2013b). One of the approaches used to alleviate this problem consists in representing the porous body as a fully dense material with mechanical properties equivalent to those of the porous structure, with the equivalent properties being obtained using the FE-based homogenisation approach and the scaling relations (Maîtrejean, Terriault et Brailovski, 2013b; Simoneau, Brailovski et Terriault, 2016) (refer to Appendix A (Section 4.10) for more details about the homogenisation approach).

Using this homogenisation approach, the femoral stem FE model comprises dense (E = 110 GPa) and equivalent porous (E = 37 GPa) zones made of Ti-6Al-4V. (To model an entirely dense stem replica, the equivalent Young's modulus of the porous zone is simply made equal to the Young's modulus of its dense part.) The distal tip of the stem is embedded in the epoxy resin medium: E = 3.7 GPa, AdTech Marine Systems ProBuild Epoxy Resin (Axson technologies, Madison Heights, MI, USA). All the materials are assumed to be perfectly elastic, with a Poisson's ratio of 0.3. Ten-node tetrahedral structural solid elements are used to mesh the model. The loading conditions (force-controlled mode) are identified in accordance with the ISO guidelines. Fully bonded conditions are assumed at the stem-resin interface and the nodes of the resin in contact with the potting tube are fixed (i.e. the potting tube (not modeled) is supposed infinitely rigid). Finally, large-deflection effects are assumed and all the simulations are carried out with ANSYS Mechanical APDL 15.0 (ANSYS, Canonsburg, PA, USA).

4.5.3.3 Experimental testing

Prior to experimental testing, the distal section of the femoral stems is potted in an aluminum tube using epoxy resin. 3D printed jigs are used to provide the proper length of embedment and orientation of the stem according to the ISO standard. Tests are performed at room temperature on an MTS Alliance RF/200 material testing system with a 10 kN load cell (Eden Prairie, MN, USA) and a 2 mm/min crosshead speed. A compression load is applied via a custom-made planar bearing system to ensure a uniaxial loading and to prevent any bending moment on the load cell (Figure 4.6a).

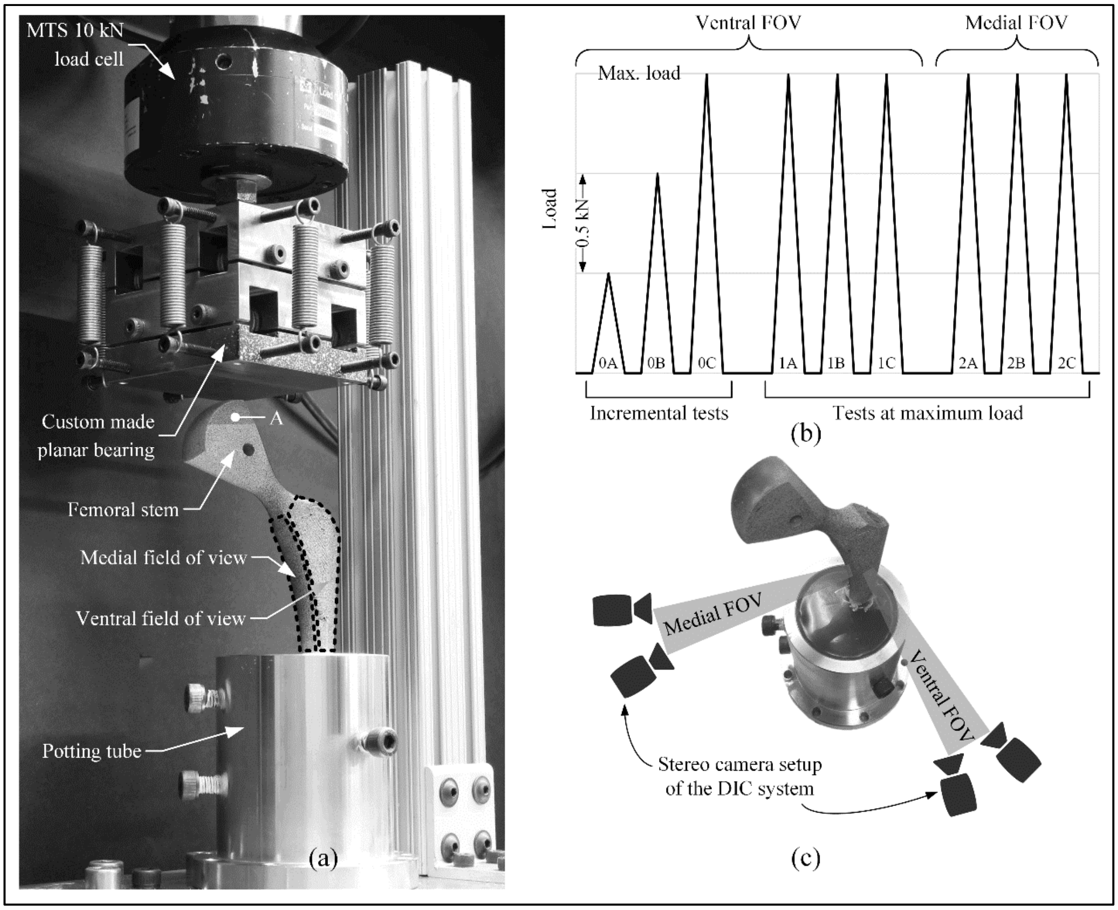

Figure 4.6 (a) Testing setup, (b) Testing protocol and (c) Camera setup for the medial and ventral FOVs

During testing, digital image correlation (DIC) is performed with an ARAMIS 5M v6.3 non-contact optical strain measurement system (GOM mbH, Braunschweig, Germany) to evaluate the displacement and strain fields on the external surfaces of the femoral stem. Note that such a measuring system is frequently used for validation of biomechanical FE models (Chanda et al., 2015; Grassi et al., 2013); DIC fundamental information are given by Kahn-Jetter et Chu (1990). Prior to testing, hot glue is applied to partially fill the pores and to provide an as-smooth-as-possible surface for image acquisition. Afterward, a stochastic fine black spray pattern on a matte white background was applied on all the open surfaces of the specimens.

The testing protocol is depicted in Figure 4.6b. First, it consists in loading the porous and the dense stems up to 1.5 and 3 kN, respectively, in 0.5 kN increments (Tests #0, Figure 4.6b).

During these incremental tests, the cameras of the DIC system are positioned to provide a field of view (FOV) on the ventral side of the stem (hereafter called “ventral FOV”) (Figure 4.6). Three consecutive tests are then performed at the maximum load (Tests #1 of Figure 4.6b). Afterward, the cameras are moved to provide a second FOV on the medial side of the stem (hereafter called “medial FOV”), and three consecutive tests at the maximum load are performed again (Tests #2 of Figure 4.6b). Such a protocol allows evaluating the repeatability of the tests and increasing the amount of data available for the FE model validation.

4.5.3.4 FE model validation: comparison of the numerical and experimental data

Prior to the FE model validation, the data measured with DIC are transformed into the coordinate system of the FE model using the best-fit registration tool of SVIEW v6.3 (GOM mbH, Braunschweig, Germany). Afterward, the surface mesh of the FE model is registered to that of the DIC (MATLAB function (Fang, 2008), SourceForge.net). Moreover, the field of views obtained with the DIC system are slightly cropped to eliminate high strain measurements near the boundaries of the surface meshes. Such an issue was also raised by Dickinson et al. (2011) and Grassi et al. (2013). Furthermore, considering that the level of strain measured during the experiments is close to the theoretical precision of the system (100 μstrain according to the manufacturer (GOM mbH, 2007)), the facet parameters of the DIC software are adjusted and a post-processed filter is applied to achieve reliable strain measurements without noise at low strain amplitude. Note that a facet is defined as an image detail containing individual gray level structures associated with the stochastic spray pattern (GOM mbH, 2007).

Validation of the FE model starts with comparing the numerical and experimental load-displacement diagrams of point A in Figure 4.6a for the porous and dense stems (experimental displacement is measured using DIC). In this study, these diagrams provide only preliminary insight into the validity of the FE model, since they compare displacements of a single point of the numerical model with those of the physical object. To take advantage of the full potential of DIC measurements, displacement and strain field measurements are also carried out and compared with those calculated numerically. Therefore, for each stem (dense and porous) and field of view (ventral and medial), a linear regression analysis is performed between two experimental and numerical metrics, namely, the vector sum of displacements (u_{TOT}) and the equivalent Mises strain (ε_{EQV}). The linear regression coefficient (slope and intercept) and the coefficient of determination (R^2) are calculated for each analysis with 95% confidence bounds.

4.6 Results

4.6.1 Load-displacement diagram

Figure 4.7 superimposes the numerical and experimental load-displacement curves of the dense and porous femoral stems, and indicates their respective flexural stiffnesses. Despite the fact that several tests were performed at the maximum load prescribed by the testing protocol, only one test result is presented in Figure 4.7 since no significant deviations were noticed between the tests. Note that during the incremental loading of the porous stem up to 1.5 kN (refer to Figure 4.6b for the testing protocol), three sharp instantaneous sounds were heard, meaning that some local failure events occurred during loading. Such peaked sounds were not heard subsequently during the tests at the maximum load of 1.5 kN.

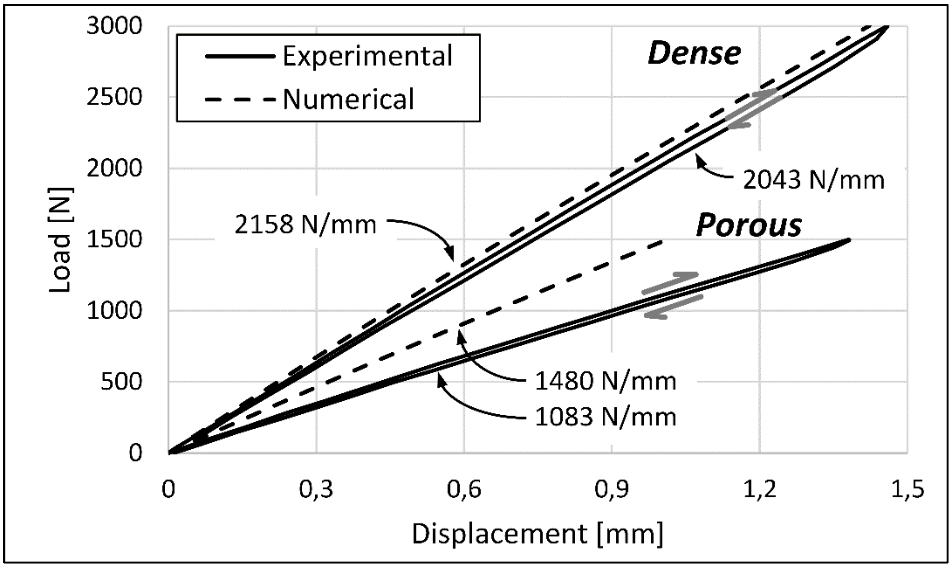

Figure 4.7 Load-displacement diagrams: numerical vs experimental tests, and dense vs porous stem concept

Based on Figure 4.7, the experimentally-measured and calculated flexural stiffness reductions of femoral stems due to the added porosity are 47 and 31%, respectively. Moreover, the numerical flexural stiffness of the dense stem slightly overestimates that of the experiment by 6% and this overestimation is much more pronounced for the porous stem concept (37% deviation).

4.6.2 Displacement and strain field

Figure 4.8 depicts the equivalent Mises strain field of the dense stem for the medial (a) and ventral (b) FOVs. Figure 4.9 presents the results of the numerical-experimental validation for the ventral FOV of the dense (a, b) and porous (c, d) stem. The vector sum displacement (a, c) and equivalent Mises strain (b, d) fields are both analysed. The left part of Figure 4.9 provides a more detailed comparison of the experimental and numerical fields, while the right part presents the results of the linear regression analysis. All the results are presented at the maximum load of 1.5 and 3.0 kN for the porous and dense stems, respectively. Complete linear regression results (slope, intersect, coefficient of determination and number of data points) for each field of view (ventral and medial) and metrics (equivalent Mises strain and vector sum displacement) are summarized in Table 4.1 and in Table 4.2 for the dense and porous stems, respectively. Note that although it appears that no data points are provided for the displacement curves on Figure 4.9a-c, it should be clarified that almost all the data point are coincident with the regression curve (i.e. $R^2 = 100\%$). Note also that a figure analogous to Figure 4.9 is provided as supplementary information for the medial FOV (Figure 4.12).

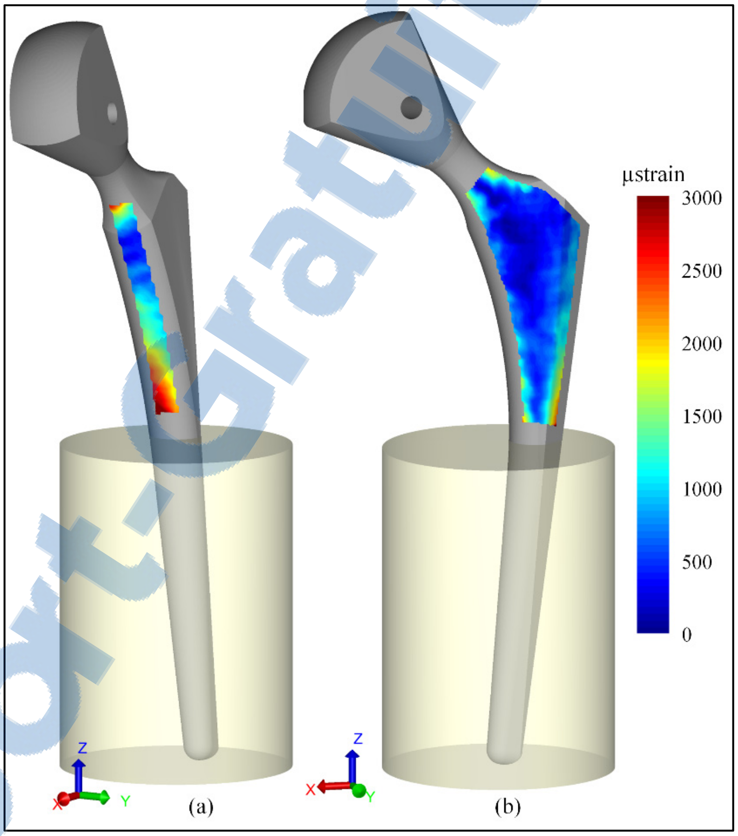

Figure 4.8 Equivalent strain field of the dense stem: (a) medial FOV and (b) ventral FOV

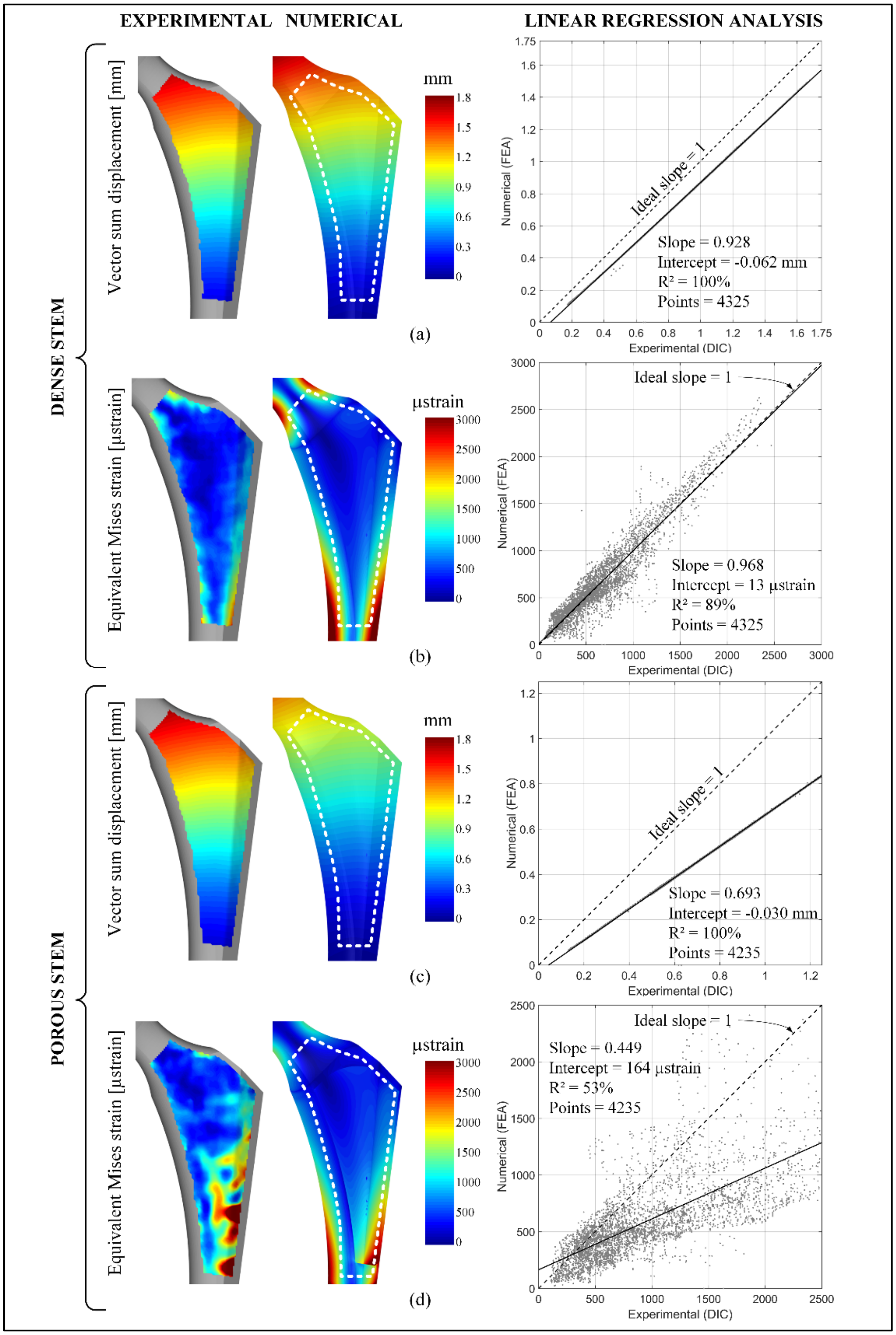

Figure 4.9 Analysis of the vector sum displacement (a, c) and equivalent Mises strain (b, d) fields for the ventral FOV of the dense (a, b) and porous (c, d) stems: the left part compares the experimental and numerical fields, and the right part presents the linear regression analysis

Table 4.1 Results of the linear regression analysis for the dense stem: displacement and strain fields

	Dense stem			
	Ventral FOV (4325 points)		Medial FOV (653 points)	
	u_{TOT}	ε_{EQV}	u_{TOT}	ε_{EQV}
Slope	0.93 ± 0	0.95 ± 0.02	0.94 ± 0.02	1.06 ± 0.07
Intersect [µstrain or mm]	-0.06 ± 0.01	29 ± 21	-0.04 ± 0.03	-29 ± 126
R² [%]	100 ± 0	90 ± 1	100 ± 0	94 ± 3

Table 4.2 Results of the linear regression analysis for the porous stem: displacement and strain fields

	Porous stem			
	Ventral FOV (4235 points)		Medial FOV (649 points)	
	u_{TOT}	ε_{EQV}	u_{TOT}	ε_{EQV}
Slope	0.70 ± 0	0.44 ± 0.01	0.70 ± 0.01	0.82 ± 0.06
Intersect [µstrain or mm]	-0.03 ± 0	180 ± 8	-0.03 ± 0.01	-67 ± 107
R² [%]	100 ± 0	51 ± 1	100 ± 0	85 ± 4

Similarly to the load-displacement diagrams of Figure 4.7, the comparison between the numerical and experimental vector sum displacement fields for each FOV shows that the FE model overestimates the experimentally-observed displacements for both stems, this overestimation being small for the dense stem (slope = 0.93 in Figure 4.9a and Table 4.1), while significant for its porous counterpart (slope = 0.70 in Figure 4.9c and Table 4.2).

As far as it concerns the equivalent Mises strain field of the dense stem, the FE model is still in good agreement with the experiments for each FOV, with a slope varying between 0.95 and 1.06 (Figure 4.9b and Table 4.1). However, when analyzing the equivalent Mises strain field of the porous stem, poor regression results are obtained for the ventral FOV (slope = 0.44 in

Figure 4.9d and Table 4.2). On the other hand, better regression results, still characterized by the constant overestimation of the FE model, are observed for the medial FOV (slope = 0.82 in Table 4.2).

4.7 Discussion

Harrysson et al. (2008) and Hazlehurst, Wang et Stanford (2014) both achieved a higher stiffness reduction (57-60%) than that reached in this study (31-47%), which is mainly attributed to a higher level of porosity (59-65%) adopted in their works. On the other hand, Yamako et al. (2014) achieved flexural stiffness reduction similar to that reached in this study (44%) using a fully-dense femoral stem made of low-modulus (E = 55 GPa) β-type Ti-33.6Nb-4Sn alloy. This similarity can be explained by the fact that dense medial and lateral strips of our design increase the global stiffness of the stem despite its porous core.

Despite the fact that the methodology adopted in this study to validate the numerical model has not been published elsewhere in the literature (to the best of our knowledge), it is still possible to find a certain number of baseline studies that have undertaken a similar work in the biomedical field: the use of DIC to characterize the mechanical behavior of porous structures (Simoneau, Brailovski et Terriault, 2016), or biological tissues (Zhang et Arola, 2004), from a global point of view (i.e. determination of their apparent properties), and the combination of DIC and linear regression analysis to validate FE model using the whole field of view of DIC measurements (Chanda et al., 2015; Dickinson et al., 2011).

Based on the very low experimental hysteresis, the linear behavior of the load-displacement diagrams (Figure 4.7) and the repeatability of the tests, it is reasonable to assume that the aforementioned localized failure events did not impact the results at the macroscale. It is however obvious that fatigue testing should be carried out to evaluate the long-term performance of such stems (ongoing work).

4.7.1 Experimental validation

To summarize, based on the results of the load-displacement diagrams of Figure 4.7 and the linear regression analyses of Figure 4.9 and Table 4.1 and Table 4.2, the FE model of the dense stem model is successfully validated, while an overestimation of the porous stem model is systematically observed. To investigate the causes of such a mismatch, the impact of the voxel size on the porosity of the porous structure has been quantified. To this end, a single porous cubic sample with a PVF of 0.33 was numerically generated, and then fabricated using different voxel sizes of 200, 250, 300 and 350 µm, while the same fabrication protocol (EOSINT M 280 400 W selective laser melting machine, EOS Ti64 performance fabrication parameters (layer thickness of 30 µm) and EOS Titanium Ti64 feedstock powder) (Figure 4.10).

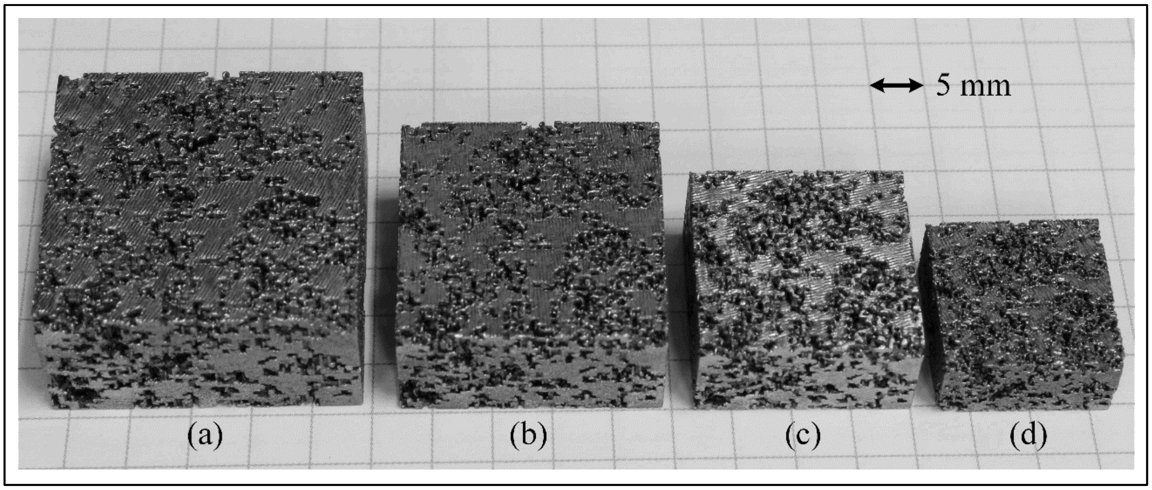

Figure 4.10 33% porous cubic samples produced with different voxel sizes (in µm): (a) 350, (b) 300, (c) 250 and (d) 200

Micro X-ray computed tomography (CT) was used to experimentally measure the PVFs of the samples: for voxel size of 200, 250, 300 and 350 µm, PVFs of 0.43, 0.38, 0.38, and 0.39 were obtained, respectively. All the micro X-Ray CT scans were performed with a Nikon XT H 225 CT system (Nikon metrology, Brighton, MI, USA), using a tube voltage and current of 225 kV and 195 µA respectively, and voxel size of 10.7, 15.5, 18.8 and 19.6 µm for the fabricated voxel size of 200, 250, 300 and 350 µm, respectively. 3D reconstruction was performed with the VG Studio Max 2.2 commercial software (Volume Graphics GmbH, Heidelberg, Germany).

When comparing the numerically-targeted porosity to the experimental measurements for various voxel sizes, an upward experimental offset was constantly observed. Furthermore, while this offset (~5%) remained constant for a voxel size of 250, 300 and 350 µm, a higher offset (~10%) was observed for a voxel size of 200 µm. Note that such a porosity offset is frequently observed for additively manufactured porous structure and that both upward and downward offsets over than 20% have been previously observed (Horn et al., 2014; Parthasarathy et al., 2010). Since a voxel size of 200 µm was adopted in this study to manufacture the porous femoral stem, it can be assumed that the targeted numerical porosity of the porous body of the stem was also offset by 10%. Therefore, considering that the apparent Young's modulus of the porous structure is strongly influenced by porosity, it becomes clear that the predicted apparent Young's modulus of the porous structure was overestimated in the FE model (37 GPa). In fact, based on the scaling relation of Figure 4.3b, an apparent Young's modulus of 24 GPa should have been considered in the FE model.

To verify this hypothesis, Table 4.3 compares the FE model validation results before and after such a porosity adjustment (refers to the supplementary information (Figure 4.13) for the illustrations of the results analogous to Figure 4.9 for the ventral and medial FOVs). While a general improvement can be observed, poor regression results similar to Figure 4.9d are still obtained for the equivalent Mises strain for the ventral FOV. Such a mismatch is mainly attributable to the fact that the smoothly-graded numerical strain field does not adequately represent the highly heterogeneous experimental strain fields (Figure 4.9d). In the light of these results, it can be suggested that a homogenization approach based on modeling the porous structure as a dense material with mechanical properties determined from scaling relations is not suitable for local strain measurement. On the other hand, such a homogenization method can still be recommended for displacement field measurement on a porous structure (Figure 4.9c), strain field measurement on a fully dense section surrounding a porous structure (i.e. medial FOV) or 2D macro strain measurement on a porous structure (Simoneau, Brailovski et

Terriault, 2016). Furthermore, considering that the strain measured on the ventral FOV is close to the precision of the DIC measuring system (~100 µm), the use of the medial FOV seems to be more appropriate.

Table 4.3 FE model validation results when considering the experimentally-measured porosity

Porosity		33% numerically-targeted	43% experimentally-measured
Young’s modulus [GPa]		37	24
Flexural stiffness [N/mm]	**Experimental**	1083	
	Modeling	1480	1253
Slope (ventral FOV)	**Displacement**	0.70	0.85
	Strain	0.44	0.69
Slope (medial FOV)	**Displacement**	0.70	0.85
	Strain	0.82	0.98

Note that a better fulfillment of the mechanical requirements is achieved with 43% porosity: there is a better match of the implant stiffness with that of bone, while still providing adequate mechanical resistance. On the other hand, the resulting pore size may be slightly too large (over 1000 µm) and could possibly increase the risk of fibrous tissue formation (Bobyn et Miller, 1994). The next design of such a porous femoral stem should certainly integrate a porosity gradient in order to provide an outer porous structure with an appropriate pore size for bone ingrowth and an inner porous structure with mechanical properties mimicking those of human bone. Moreover, the medial and lateral dense strips could be offset inward in order to provide space for adding a stochastic porous coating for bone ingrowth. Finally, a CT scan performed on the porous implant revealed a certain quantity of trapped powder in the distal region surrounded by the solid shell. To allow circulation of compressed air during powder removal, the next stem design should integrate a hole at the distal tip (Hazlehurst, Wang et Stanford, 2014). However, this fact did not influence the experimental results since the distal portion of the stem was entirely embedded in epoxy resin during mechanical testing.

4.7.2 Manufacturing limitation

According to Figure 4.3a, the maximum porosity available in the design space (33%) was limited by the minimum voxel size achievable with our additive manufacturing protocol. Consequently, the minimum voxel size should be lowered in order to provide a greater design space and to reach higher porosities in the design space. To do so, the use of other feedstock material combined with finer fabrication parameters (e.g. the EOS CobaltChrome SP2 alloy for dental application works with a layer thickness of 20 µm while the EOS Titanium Ti64 alloy works with a layer thickness of 30 µm (EOS GmbH Electro Optical Systems)) or other SLM systems using a smaller beam focus diameter (e.g. the M1 cusing system of Concept Laser offers a focus diameter of 50 µm (Concept Laser GmbH) while the EOSINT M280 system offers a variable focus diameter of 100-500 µm (EOS GmbH Electro Optical Systems)) could possibly improve the accuracy of the AM protocol, and therefore achieve better results. Moreover, such considerations could also possibly reduce the offset between the numerically-targeted and experimentally-measured porosity.

4.7.3 Surface-to-volume ratio

The bone surface-to-volume ratio (Sv) significantly contributes to bone remodeling when maximized. Based on the literature data, the Sv of bone tissue is strongly influenced by the bone pore volume fraction (PVF), and reaches its maximum value with an intermediate PVF (Beaupré, Orr et Carter, 1990; Coelho et al., 2009; Martin, 1984) (Figure 4.11). In this study, the surface-to-volume ratio (Sv) of the porous structures (defined as the open area of solid surface per unit of apparent volume) has been numerically evaluated for PVF ranging from 5 to 95% for a voxel size of 200 µm. When compared with the Sv of bone (Figure 4.11), it can be concluded that the 33% porosity proposed in this study offers an interesting potential for bone remodeling.

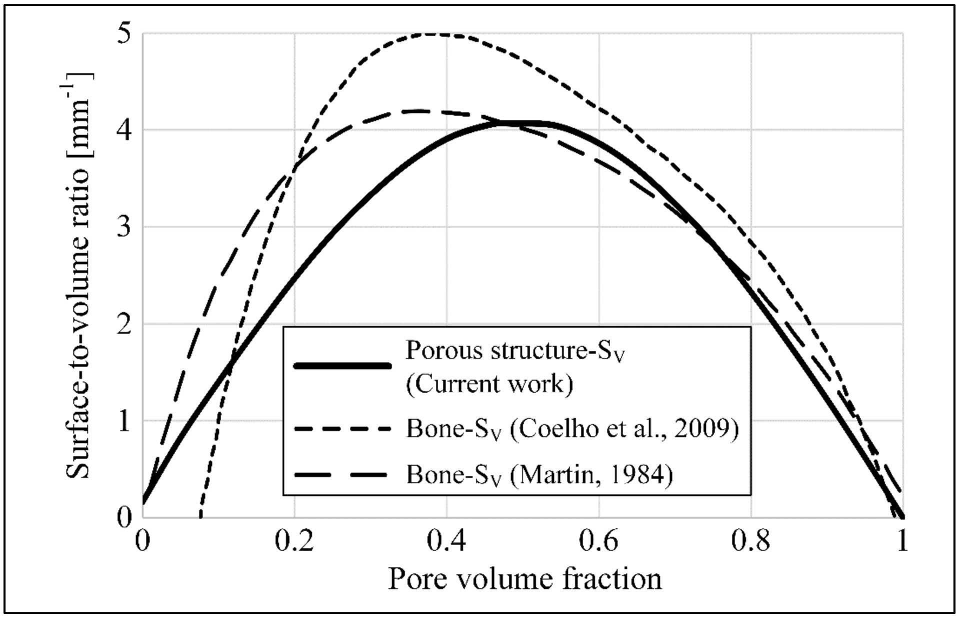

Figure 4.11 Surface-to-volume ratio (Sv) as a function of pore volume fraction (PVF) for human bone and the stochastic porous structure

4.7.4 Future work

Although flexural testing carried out in this study, and in those of Harrysson et al. (2008) and Hazlehurst, Wang et Stanford (2014), has given comprehensive results regarding the mechanical response of porous femoral stems, biomechanical testing still remains unavoidable in order to evaluate the possible reduction of the stress shielding effect. To this end, the composite femur model commercialized by Pacific Research Laboratories (Vashon Island, WA, USA) has been widely used for years since it can adequately replace cadaveric specimens for reasons of availability, variability and preservation techniques (Ke et al., 1999).

On one hand, several in vitro experimental studies were found, in which stress the shielding effect was evaluated on composite femur implanted with fully dense metallic stems (Chanda et al., 2015; Grassi et al., 2013; Tayton, Evans et O'Doherty, 2010; Yamako et al., 2014). On the other hand, several numerical in vitro studies could be found, where composite bone implanted with porous femoral stem is used to evaluate the effect of implant porosity on bone remodeling (Yan, Berthe et Wen, 2011) or to optimize the implant porosity distribution in order to enhance bone-implant interface stability (Khanoki et Pasini, 2012). However, these numerical models were not experimentally validated. In fact, no published studies have experimentally evaluated the biomechanical performance of porous femoral stem in vitro (to the best of our knowledge).

This lack of experimental validation will be addressed in our future works, where the following three-step test strategy is adopted: 1) test and compare the behavior of porous and dense femoral stems of same geometry (this study), 2) test an intact composite femur, and 3) compare the behavior of the intact femur with that of the femurs implanted with porous and dense femoral stems (refer to Brailovski et al. (2016) for the description of the methodological approach employed for this test strategy).

4.8 Conclusion

The objective of this work was to develop a porous biomimetic femoral stem with enhanced biomechanical compatibility. A design space diagram was firstly proposed to understand the relationship between bone ingrowth requirements and the selective laser melting limitations. The optimal porosity identified in the diagram (33%) was thereafter applied to the porous material composing the femoral stem. The freeform manufacturing potential of SLM was then used to produce the porous femoral stem and a fully dense replica with Ti-6Al-4V powder. Flexural testing of the stems was carried out according to the ISO 7206-4 standard, and a flexural stiffness reduction of 47% was obtained when comparing the porous stem to its dense counterpart. In parallel an FE model was developed to predict the mechanical response of the stem. Fields of equivalent Mises strain and vector sum displacement were both tracked in the course of loading using digital image correlation and finite element analysis. Linear regression analyses were thereafter performed to validate the finite element results. While the FE model of the dense stem was in line with the experiment, poor correlation with the experiment was obtained for the porous stem model. This mismatch was partially attributed to the fact that the porosity of the manufactured porous stem was 10% higher than that of the original STL file. The subsequent adjustment of the FE model to consider this porosity offset has significantly, but not entirely, decreased the discrepancy between the modeling and the experiment. Future works will be devoted to the biomechanical in-vitro testing of artificial femurs implanted with the porous and dense stems to evaluate the reduction of the stress shielding.

4.9 Acknowledgments

The authors would like to credit the Fonds de développement de l'ÉTS (FDETS), Fonds de recherche du Québec - Nature et Technologies (FRQ-NT) and the Natural Sciences and Engineering Research Council of Canada (NSERC) for their financial support.

4.10 Appendix A

This appendix gives complementary information on the numerical generation, morphological and mechanical characterization and finite element modeling of the porous structures.

An in-house voxel-based MATLAB 2015b (MathWorks Inc., Natick, MA, USA) routine has been developed to generate the morphology of stochastic open-cell porous structures. The algorithm starts by defining and voxelizing a domain within which a porous structure will be generated. Afterward, the domain is filled with randomly picked matter voxels sharing at least one common face (6-connectivity). Domain filling is performed until reaching a targeted porosity or pore volume fraction (PVF). Execution of the algorithm results in an assembly of interconnected matter voxels ensuring the structural integrity of the porous structure, and in an assembly of interconnected void voxels ensuring its fully open porosity. The porosity and the size of the voxelized domain are the two input parameters of the algorithm and both parameters have a direct influence on the pore size, shape and distribution. Such output parameters are evaluated using stereology (a direct observation of the porous structure cross-sections) based on the built-in MATLAB function “RegionProps”. Consequently, the size of a pore corresponds to the equivalent diameter of a cross-section pore. Following stereology analysis, it was founded that the pore size follows a log-normal distribution analogous to that of titanium foams produced with the space-holder method (i.e. experimental validation of the numerical morphology).

Setting up of the scaling relation linking the porosity to the apparent Young's modulus of the porous structure was performed using a finite element-based homogenisation approach. More precisely, displacement-controlled linear FEA has been performed on representative volume elements of the porous structure (generated by the morphology modeling algorithm) under periodic boundary conditions. In parallel, the same porous structures were fabricated using SLM and CoCrMo powder, and then subjected to uniaxial tension. The apparent Young's moduli were thus collected and successfully compared to the numerical results.

Note that because of the intrinsic stochastic behavior of the morphology modeling algorithm, a minimum size of the domain (i.e. a representative volume element) beyond which any further increases in size has an insignificant influence on the morphological and mechanical properties of the porous structure was determined prior to the experimental validation of the numerical results. For this study, the smallest representative cubic RVE can be calculated as follows: for a given porosity of 33%, 50^3 voxels are needed to allow the adequate representation of the morphological (d_{50} pore size) and mechanical (Young's modulus) features of the porous structure. With a voxel size of 200 µm, a 50^3-voxel domain corresponds to a cube of 1 cm^3. Since this physical RVE is smaller than the volume of the porous zone of the stem, the randomness of the morphology generation algorithm should not impact the FE modeling results.

4.11 Supplementary information

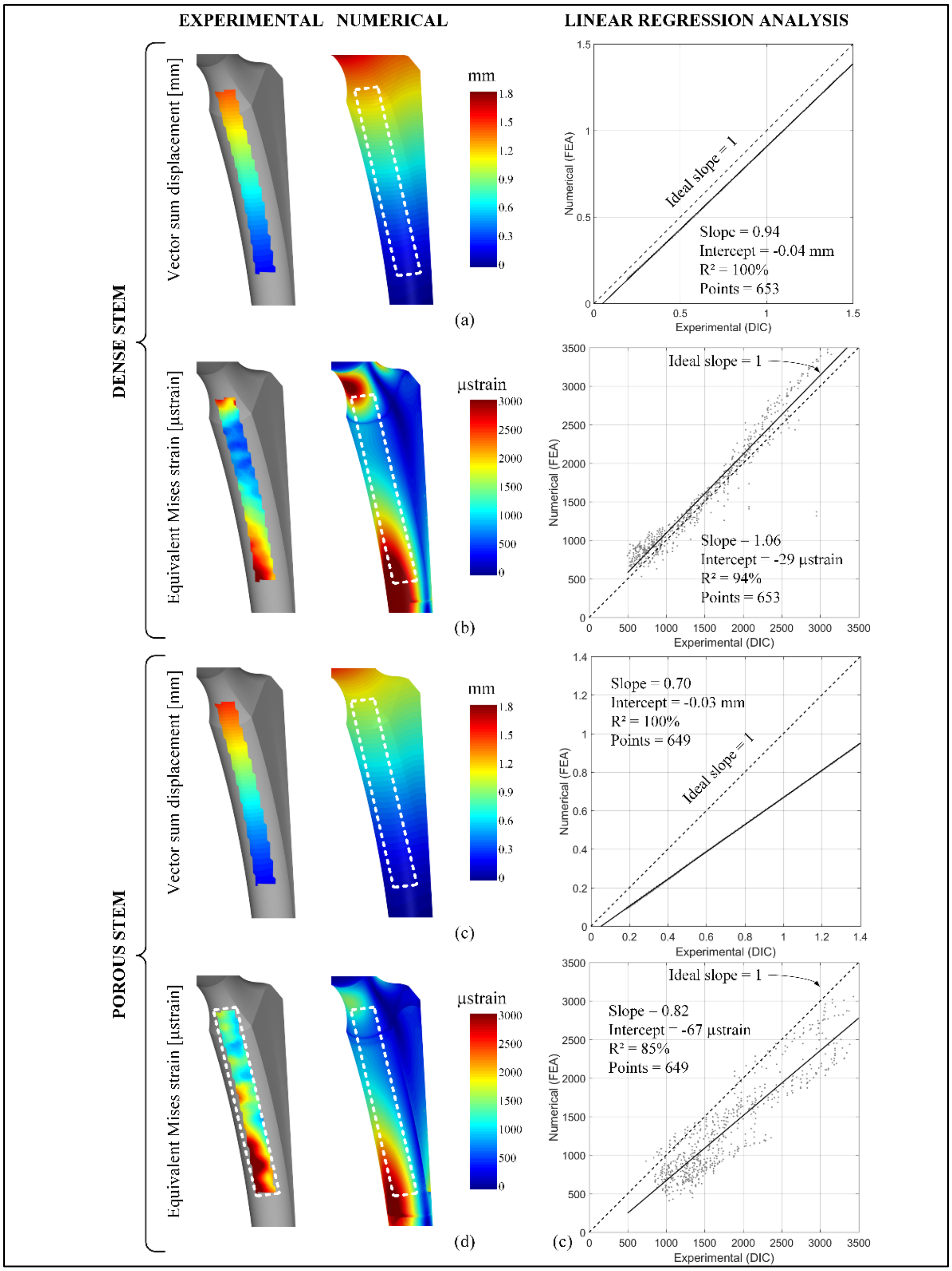

Figure 4.12 Analysis of the vector sum displacement (a, c) and equivalent Mises strain (b, d) fields for the medial FOV of the dense (a, b) and porous (c, d) stems: the left part compares the experimental and numerical fields, and the right part presents the linear regression analysis

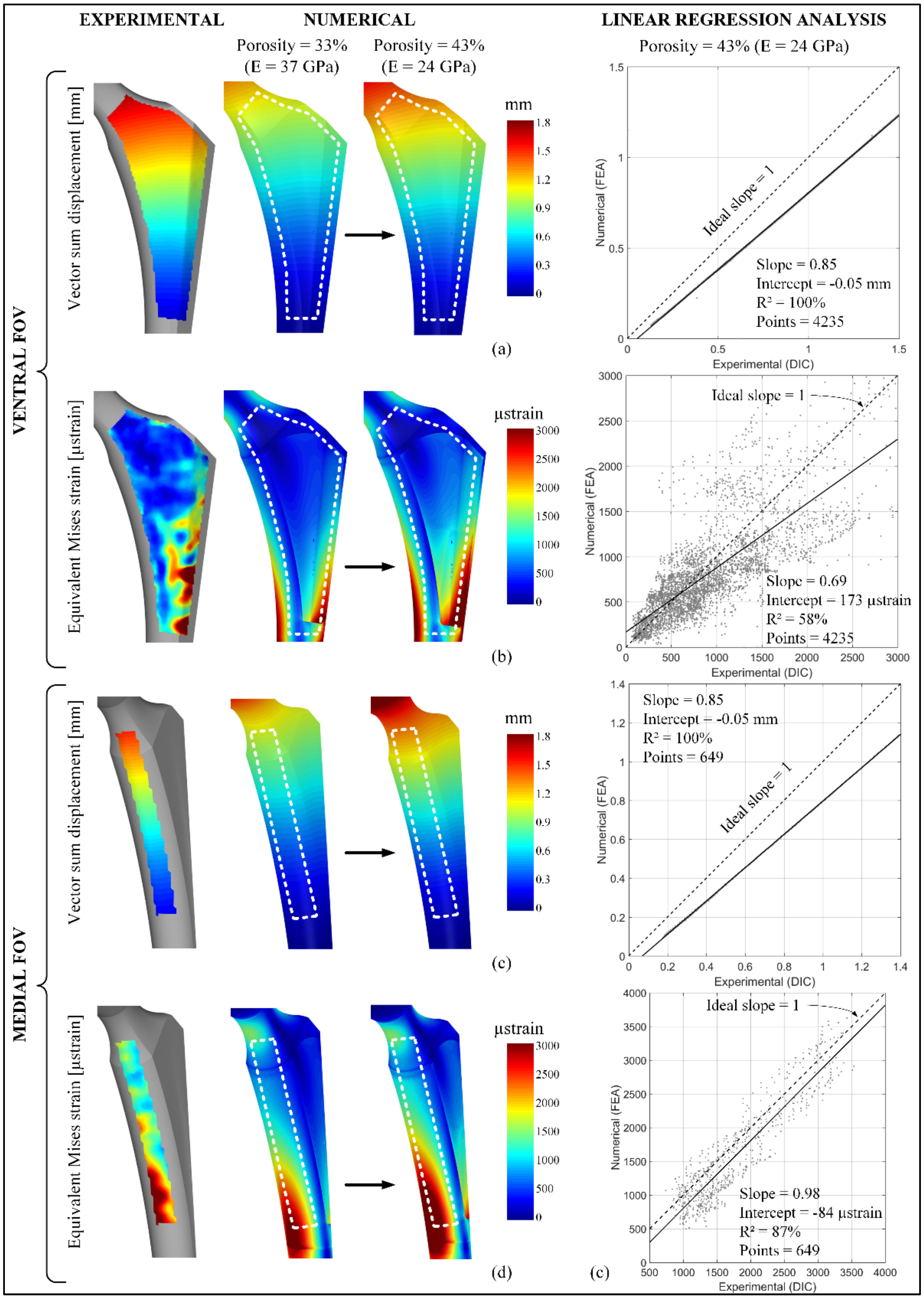

Figure 4.13 Analysis of the vector sum displacement (a, c) and equivalent Mises strain (b, d) fields for the porous stem for the ventral (a, b) and medial (c, d) FOVs: the left part compares the experimental and numerical fields after and before the porosity adjustment, and the right part presents the linear regression analysis after the porosity adjustment

To pursue the investigation of the deviation between the experimentally-measured (42%) and the numerically-targeted (33%) porosities, the morphology of the porous cubic samples shown in Figure 4.10 was analyzed using the cross-sections obtained with the micro-CT scans (image analysis), and then compared to that of the numerical model. Figure 4.14a-b compares a typical cross-section of the porous sample fabricated with a 200 µm voxel size to its numerical counterpart, and Figure 4.14c-d compares their resulting pore size distributions based on the best-fit ellipses with the same area, orientation and centroid of the pores. The image analysis resulted in experimental and numerical porosities of 49.2 and 38.9%, respectively which were similar to the overall porosity measurements. The experimental pore size distribution (Figure 4.14c) revealed the presence of a greater number of large pores when compared to that of the numerical distribution (Figure 4.14d). Such results correlate with the upward experimental porosity offset and may be attributed to the limitation of the SLM technology to reproduce the sharp details of the numerical model.

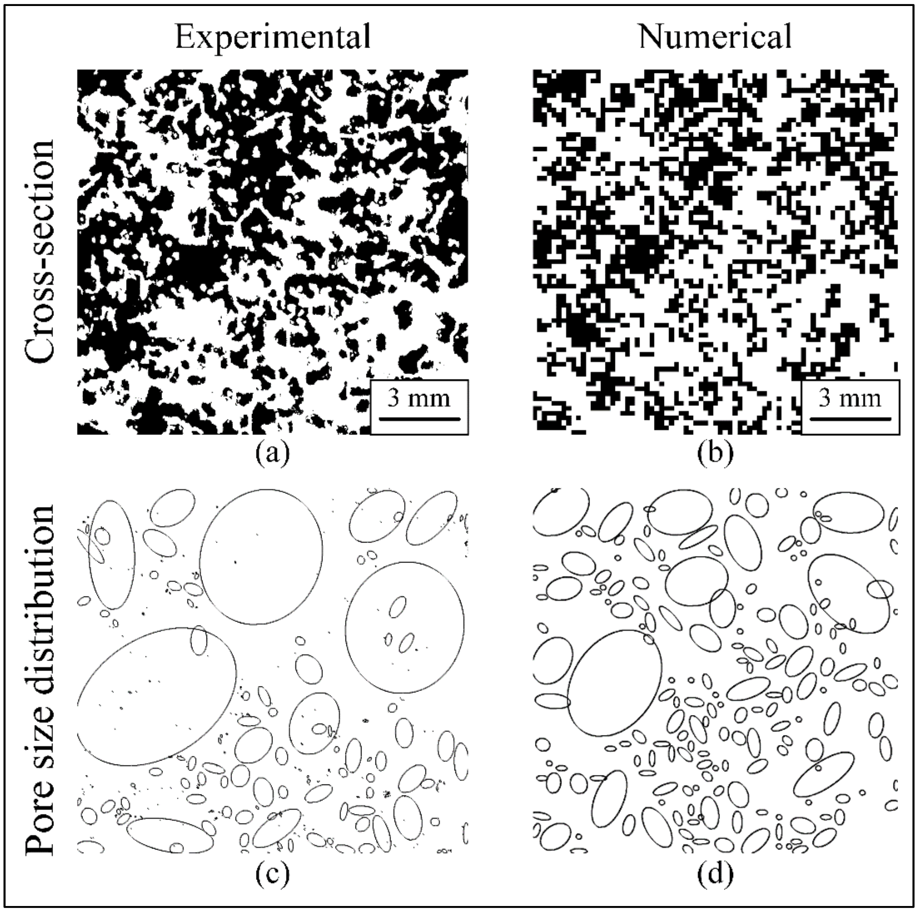

Figure 4.14 Cross-sections (a, b) and pore size distribution (c, d) of the porous sample fabricated with a voxel size of 200 µm (a, c) and generated with the modeling algorithm (b, d)

DISCUSSION GÉNÉRALE ET CONTRIBUTIONS SCIENTIFIQUES

Respect des exigences fonctionnelles du cahier des charges

En considérant une taille de voxel de 36 µm, la morphologie des structures poreuses générées par l'algorithme répond adéquatement aux exigences biologiques du cahier des charges (interconnectivité et taille des pores) en plus de bien se comparer à celle de mousses de titane produites par frittage de poudre avec matériau espaceur. En contrepartie, contrairement aux technologies fabrication additive (FA), le procédé de frittage ne permet pas la mise en forme directe d'un implant orthopédique intégrant une structure poreuse. Toutefois, la taille des pores des structures poreuses obtenues par la FA, plus particulièrement par la fusion sélective par laser sur lit de poudre, est très proche et excède même les limites fixées pour une saine ostéo-intégration en raison du manque de finesse des équipements de FA utilisés dans le cadre de ce projet. En effet, la plus petite taille de voxel atteinte par FA est d'environ 200 µm (taille 5 à 6 fois plus élevée que le procédé de frittage). Un des palliatifs à cette problématique réside dans l'utilisation d'équipements de FA permettant d'aller chercher plus de finesse au niveau de l'épaisseur des couches, la taille des particules et le diamètre du faisceau laser.

Le matériau de base constituant la structure poreuse joue un rôle prépondérant sur son comportement mécanique. En utilisant un alliage de cobalt-chrome dont la rigidité est d'environ 220 GPa, les exigences mécaniques du cahier des charges (rigidité et contrainte d'écoulement) ne sont pas respectées, peu importe le niveau de porosité choisi. Cette problématique peut être toutefois contournée en adoptant l'alliage de titane Ti-6Al-4V possédant une rigidité deux fois plus basse ou encore un alliage de titane bêta métastable possédant des propriétés superélastiques et une rigidité environ quatre fois plus basse. De ce fait, la compatibilité mécanique de telles structures poreuses est grandement améliorée.

Tige fémorale poreuse

Présentement, la surface externe des tiges fémorales disponibles sur le marché est uniquement composée d'un revêtement poreux et d'hydroxyapatite. De ce fait, l'ostéo-intégration au sein du corps de l'implant n'est pas possible : on parle plutôt d'une croissance osseuse par apposition. Cette approche est actuellement adoptée afin de faciliter l'extraction de la tige si jamais certaines complications causées par le phénomène de déviation de contrainte sont observées.

La contribution scientifique principale de ces travaux se situe au niveau du développement de la tige fémorale poreuse. En effet, cet implant a été conçu afin de répondre le mieux possible aux diverses exigences biomécaniques du cahier des charges tout en considérant les limitations technologiques de la fusion sélective par laser sur lit de poudre. Ce nouveau type d'implant orthopédique devrait permettre d'éliminer les chirurgies de reprise grâce à sa structure poreuse offrant une rigidité réduite et morphologie favorisant la croissance osseuse. En effet, en considérant que tous les problèmes liés au phénomène de déviation de contrainte sont résolus, il ne devient plus essentiel de concevoir la tige selon l'approche traditionnelle voulant qu'on puisse la retirer facilement.

Il est toutefois important de mentionner que beaucoup de travaux doivent être réalisés avant que cette nouvelle approche ne soit adoptée par la communauté scientifique et médicale. Afin de poursuivre cet essor, certaines recommandations sont émises à la fin du présent document.

Simulation du comportement mécanique des structures poreuses

La simulation par éléments finis du comportement mécanique de structures poreuses stochastiques requiert une très grande quantité de ressources informatiques et un temps de calcul élevé. Par exemple, l'analyse structurale statique en petit déplacement d'une structure poreuse cubique de 50% de porosité composée 60 x 60 x 60 voxels ($S_{RVE} = 60^3$) où chaque voxel est discrétisé en 6 x 6 x 6 éléments finis hexaédriques à interpolation quadratique à

20 nœuds ($FE_{VOXEL} = 6^3$) a mené à un maillage d'environ 23 000 000 d'éléments. Cette simulation a nécessité la parallélisation de 32 cœurs (Intel® Xeon® CPU E5-2670 @ 2.60GHz) et 550 Go de mémoire vive (RAM) et s'est effectuée sur le superordinateur Guillimin de l'Université McGill. Considérant que le maillage requis pour effectuer une simulation sur la tige fémorale poreuse est estimé à plus de 421 000 000 d'éléments, il devient tout simplement inconvenable de poursuivre avec une telle approche de simulation directe.

Pour pallier à cette problématique, une technique de modélisation multiéchelle basée sur l'approche du volume élémentaire représentatif a été développée dans le cadre de ce projet. En évitant la simulation directe du comportement mécanique de la tige fémorale poreuse à l'aide de l'échelle macroscopique, un modèle éléments finis d'environ 100 000 éléments est suffisant pour l'obtention de résultats représentatifs. En combinant cette technique avec les relations de mise à l'échelle pouvant être utilisées pour estimer les propriétés apparentes d'une structure poreuse en fonction de sa porosité, des outils de conception numérique dotés d'un fort potentiel ont été développés. De tels développements font également partie des contributions scientifiques de ces travaux.

Il est toutefois important de signaler que certaines limitations liées à l'approche de modélisation multiéchelle ont été observées. Parmi ces dernières, il est possible de mentionner que l'échelle macroscopique ne permet pas de simuler localement le comportement mécanique de la structure poreuse en termes de déformation et contrainte. Ceci est attribuable au fait que la structure poreuse est constituée d'un matériau dense possédant des propriétés de matériau fictives. Cette hypothèse s'est confirmée lors de la validation expérimentale du modèle où la corrélation d'images numériques a été utilisée pour caractériser le comportement mécanique de la structure poreuse. En effet, tandis qu'une distribution fortement désordonnée des déformations est observée d'un point de vue expérimental, une distribution de nature très homogène est observée d'un point de vue numérique.

CONCLUSION GÉNÉRALE

L'objectif principal de ce projet était de modéliser, fabriquer et caractériser mécaniquement et morphologiquement des structures poreuses pour applications médiales. Plus précisément, ces structures poreuses se devaient de présenter un excellent potentiel de biocompatibilité caractérisé par un comportement mécanique similaire à celui des tissus osseux ainsi que par une morphologie à porosité ouverte favorisant l'ostéo-intégration. De plus, une attention particulière a été portée sur le développement d'un modèle numérique permettant de simuler le comportement mécanique des structures poreuses.

Dans un premier temps, un algorithme de génération a été développé afin de pouvoir générer la morphologique stochastique de structure poreuse à porosité ouverte. Cet algorithme permet notamment de créer des structures poreuses de n'importe quelle forme, dimension et porosité. Une analyse stéréologique effectuée sur les mousses générées par l'algorithme a révélé une morphologie similaire à celle de mousses de titane produites par le frittage de poudres métalliques avec matériau espaceur. Il est à noter qu'au préalable, l'approche du volume élémentaire représentatif avait été utilisée afin de déterminer les tailles minimales des mousses permettant d'avoir une morphologie représentative.

Dans un deuxième temps, suite à la caractérisation des propriétés morphologiques, les propriétés mécaniques des mousses ont été déterminées de façon numérique et expérimentale. L'approche numérique était fondée sur la méthode des éléments finis et l'approche du volume élémentaire représentatif permettant de déterminer les tailles minimales des mousses menant à un comportement mécaniquement représentatif. L'approche expérimentale était fondée sur des essais de traction effectués sur des échantillons poreux produits par fabrication additive dont la taille était mécaniquement représentative. Les essais de traction ont notamment pu être utilisés pour la validation du modèle numérique.

Dans un troisième temps, ayant en main les propriétés morphologiques et mécaniques des mousses, une porosité optimale menant à des propriétés mécaniques similaires à celle de l'os et favorisant la croissance osseuse a été adoptée pour la conception d'une tige fémorale poreuse métallique. Ensuite, la fusion sélective sur lit de poudre a été utilisée pour la fabrication additive d'une tige fémorale poreuse ainsi que d'une autre complètement dense. Puis, selon des conditions normalisées de chargement, un modèle éléments finis ainsi qu'un montage expérimental ont été développés en parallèle afin d'évaluer la rigidité de la tige poreuse par rapport à celle de la tige dense. Malgré certains écarts entre les résultats numériques et expérimentaux, la même tendance a été observée, soit une réduction significative de la rigidité de la tige fémorale poreuse en comparaison avec celle complètement dense.

Finalement, bien que les structures poreuses développées dans le cadre de cette thèse fussent destinées à des applications médicales, il est important de souligner que de telles structures pourraient être utilisées pour d'autres applications comme l'aérospatiale où l'aspect de la légèreté d'un composant par rapport à sa rigidité est primordial. À cet effet, le cahier des charges n'aurait qu'à être révisé et ce faisant, la même méthodologie (algorithme de génération, analyse structurale par éléments finis, fabrication additive, caractérisation mécanique et morphologique) pourrait être réutilisée afin de répondre aux nouvelles exigences fonctionnelles.

RECOMMANDATIONS

Les travaux de ce projet doctoral avaient pour but de démontrer que la compatibilité biomécanique des implants orthopédiques présentement commercialisés pouvait être grandement améliorée grâce au développement de structures métalliques poreuses. Cet aspect a été particulièrement mis en valeur lors du développement de la tige fémorale poreuse. Cependant, afin de poursuivre ce projet, plusieurs recommandations peuvent être émises :

- En ce moment, le modèle numérique est uniquement valide dans le domaine élastique de la structure poreuse. Afin de poursuivre le développement du modèle, ce dernier devrait être en mesure de simuler l'endommagement de la structure poreuse au cours de son chargement. Cet aspect serait fort utile lors de la conception puisqu'il est impératif que la limite d'écoulement de l'implant soit supérieure à celle des tissus osseux. La caractérisation numérique de la résistance mécanique des structures poreuses permettrait également l'obtention d'une nouvelle métrique comme le ratio résistance mécanique/masse volumique (*specific strength* en anglais).
- Lors de la conception de la tige fémorale poreuse, plutôt que d'adopter un seul niveau global porosité, la porosité dans la tige pourrait variée localement de façon à optimiser la distribution des chargements mécaniques afin de diminuer au maximum le phénomène de déviation des contraintes. Pour ce faire, les algorithmes d'optimisation topologique pourraient être mis à contribution. Enfin, il est à noter que l'algorithme de génération possède déjà les fonctionnalités lui permettant de créer des gradients de porosité, mais pourrait être amélioré de façon à générer une structure poreuse biomimétique semblable aux tissus osseux humains.
- Le comportement en fatigue est un des aspects les plus importants à considérer en ce qui concerne l'utilisation des structures poreuses pour applications médicales. Puisque cet aspect n'a pas été abordé dans cette thèse, il devient inévitable qu'une telle étude soit réalisée. À cet effet, tel que discuté dans la littérature, le développement de traitement thermique peut aider à améliorer la durée de vie en fatigue.

- Les essais mécaniques réalisés sur la tige fémorale poreuse ont été effectués selon des conditions normalisées de chargement. Ces dernières ne sont toutefois pas représentatives du point de vue de la biomécanique. Par conséquent, il est impératif de réaliser des essais *in-vitro* afin de poursuivre le développement de tels implants. Pour ce faire, il est possible de considérer l'utilisation de fémurs artificiels et la stratégie d'essai suivante : la comparaison du comportement mécanique d'un fémur intact (le spécimen de contrôle) à celui d'un fémur implanté d'une tige fémorale dense et d'un autre fémur implanté d'une tige poreuse. Ce faisant, le phénomène de déviation de contrainte devrait pouvoir être clairement identifié sur le fémur implanté de la tige dense tandis qu'une meilleure distribution des contraintes devrait pouvoir être observée sur le fémur implanté de la tige poreuse (Brailovski et al., 2016).
- Ce projet s'est uniquement orienté autour des structures poreuses à morphologie stochastique fondée sur la génération aléatoire et successive de voxels. Cependant, il n'est pas dit que ce type de structure poreuse est le plus approprié pour l'application visée. Afin d'optimiser les performances de telles structures pour les applications médicales, il sera nécessaire d'investiguer d'autres approches pour la génération des structures poreuses. De ce fait, l'étude des structures poreuses à morphologie ordonnée devient inévitable puisqu'une grande quantité de cellules unitaires existe dans la littérature. Les méthodes et outils développés durant ce projet pourraient être aisément repris afin d'effectuer une telle étude comparative. Un des principaux avantages des structures poreuses ordonnées par rapport aux structures stochastiques est la taille du volume élémentaire représentatif : environ sept cellules unitaires sont requises pour avoir des résultats représentatifs. De ce fait, la taille des modèles numériques est considérablement réduite par rapport à l'approche stochastique.

LISTE DE RÉFÉRENCES BIBLIOGRAPHIQUES

Abell, A. B., K. L. Willis et D. A. Lange. 1999. « Mercury Intrusion Porosimetry and Image Analysis of Cement-Based Materials ». *Journal of Colloid and Interface Science,* vol. 211, nº 1, p. 39-44.

Ahmadi, Seyed Mohammad, Saber Amin Yavari, Ruebn Wauthle, Behdad Pouran, Jan Schrooten, Harrie Weinans et Amir A Zadpoor. 2015. « Additively manufactured open-cell porous biomaterials made from six different space-filling unit cells: The mechanical and morphological properties ». *Materials,* vol. 8, nº 4, p. 1871-1896.

Aitkenhead, Adam H. 2013. *Mesh voxelisation - Voxelise a triangular-polygon mesh.* < http://www.mathworks.com/matlabcentral/fileexchange/27390-mesh-voxelisation/content/Mesh_voxelisation/VOXELISE.m >. Consulté le July 11, 2016.

Alkhader, Maen, et Murat Vural. 2008. « Mechanical response of cellular solids: Role of cellular topology and microstructural irregularity ». *International Journal of Engineering Science,* vol. 46, nº 10, p. 1035-1051.

Aly, Mohamed Shehata. 2010. « Effect of pore size on the tensile behavior of open-cell Ti foams: Experimental results ». *Materials Letters,* vol. 64, nº 8, p. 935-937.

Amin Yavari, S., S. M. Ahmadi, R. Wauthle, B. Pouran, J. Schrooten, H. Weinans et A. A. Zadpoor. 2015. « Relationship between unit cell type and porosity and the fatigue behavior of selective laser melted meta-biomaterials ». *Journal of the Mechanical Behavior of Biomedical Materials,* vol. 43, p. 91-100.

ANSYS ®. 2011. *ANSYS Academic Research, Release 14.0, Help System, Mechanical APDL, Structural Analysis Guide*.

Arabnejad, Sajad, Burnett Johnston, Michael Tanzer et Damiano Pasini. 2016. « Fully porous 3D printed titanium femoral stem to reduce stress-shielding following total hip arthroplasty ». *Journal of Orthopaedic Research*, p. n/a-n/a.

Ashby, M. F., A. G. Evans, N. A. Fleck, L. J. Gibson, J. W. Hutchinson et H. N. G. Wadley (27-29). 2000. *Metal Foams: A Design Guide*, 1st. Burlington: Butterworth-Heinemann Limited, 251 p.

ASTM B962-15. 2015. *Standard Test Methods for Density of Compacted or Sintered Powder Metallurgy (PM) Products Using Archimedes' Principle*. ASTM International.

ASTM C20-00. 2015. *Standard Test Methods for Apparent Porosity, Water Absorption, Apparent Specific Gravity, and Bulk Density of Burned Refractory Brick and Shapes by Boiling Water*. ASTM International. Consulté le 30 Apr 2016.

ASTM F2792-12a. 2015. *Standard Terminology for Additive Manufacturing Technologies*. West Conshohocken, PA: ASTM International. Consulté le 2016-10-06.

Bandyopadhyay, Amit, B. V. Krishna, Weichang Xue et Susmita Bose. 2008. « Application of Laser Engineered Net Shaping (LENS) to manufacture porous and functionally graded structures for load bearing implants ». *Journal of Materials Science: Materials in Medicine,* vol. 20, n° 1, p. 29-34.

Banhart, John. 2001. « Manufacture, characterisation and application of cellular metals and metal foams ». *Progress in materials Science,* vol. 46, n° 6, p. 559-632.

Bansiddhi, A., T. D. Sargeant, S. I. Stupp et D. C. Dunand. 2008. « Porous NiTi for bone implants: a review ». *Acta Biomaterialia,* vol. 4, n° 4, p. 773-82.

Baumeister, Joachim, et Jörg Weise. 2013. « Manufacturing Processes for Metal Foams ». In *Metal Foams: Fundamentals and Applications*, sous la dir. de Dukhan, N., p. 131-216. Lancaster: DEStech Publications, Inc. < http://books.google.ca/books?id=xZRG1EyBbzsC >.

Beaupré, G. S., T. E. Orr et D. R. Carter. 1990. « An approach for time-dependent bone modeling and remodeling—theoretical development ». *Journal of Orthopaedic Research,* vol. 8, n° 5, p. 651-661.

Belsky, V., M. W. Beall, J. Fish, M. S. Shephard et S. Gomaa. 1995. « Computer-aided multiscale modeling tools for composite materials and structures ». *Computing Systems in Engineering,* vol. 6, n° 3, p. 213-23.

Bobyn, J. D., R. M. Pilliar, H. U. Cameron et G. C. Weatherly. 1980. « The Optimum Pore Size for the Fixation of Porous-Surfaced Metal Implants by the Ingrowth of Bone ». *Clinical Orthopaedics and Related Research,* vol. 150, p. 263-270.

Bobyn, J. D., G. J. Stackpool, S. A. Hacking, M. Tanzer et J. J. Krygier. 1999. « Characteristics of bone ingrowth and interface mechanics of a new porous tantalum biomaterial ». *Journal of Bone & Joint Surgery, British Volume,* vol. 81, n° 5, p. 907-914.

Bobyn, J., et J. Miller. 1994. « Features of biologically fixed devices ». In *Orthopaedic basic science*, sous la dir. de Simon, S.R., p. 704. Chicago: American Academy of Orthopaedic Surgeons. < http://books.google.ca/books?id=d8JsAAAAMAAJ >.

Bragdon, Charles R., Murali Jasty, Meridith Greene, Harry E. Rubash et William H. Harris. 2004. « Biologic Fixation of Total Hip Implants ». *Insights Gained from a Series of Canine Studies,* vol. 86, n° suppl 2, p. 105-117.

Brailovski, V., S. Prokoshkin, M. Gauthier, K. Inaekyan, S. Dubinskiy, M. Petrzhik et M. Filonov. 2011. « Bulk and porous metastable beta Ti–Nb–Zr (Ta) alloys for biomedical applications ». *Materials Science and Engineering: C,* vol. 31, n° 3, p. 643-657.

Brailovski, V., et P. Terriault. 2016. « Metallic Porous Materials for Orthopedic Implants: Functional Requirements, Manufacture, Characterization, and Modeling ». In *Reference Module in Materials Science and Materials Engineering*. Elsevier. < http://www.sciencedirect.com/science/article/pii/B9780128035818038923 >.

Brailovski, V., P. Terriault, C. Simoneau, M. Dumas et B. Jetté. 2016. « Development of a biomimetic metallic femoral stem: methodological approach ». In *THERMEC 2016*. (Graz, Autria, May 29-June 3).

Brenne, F., T. Niendorf et H. J. Maier. 2013. « Additively manufactured cellular structures: Impact of microstructure and local strains on the monotonic and cyclic behavior under uniaxial and bending load ». *Journal of Materials Processing Technology,* vol. 213, n° 9, p. 1558-1564.

Cameron, HU, I Macnab et RM Pilliar. 1978. « A porous metal system for joint replacement surgery ». *The International journal of artificial organs,* vol. 1, n° 2, p. 104-109.

Campoli, Gianni, M. S. Borleffs, S. Amin Yavari, R. Wauthle, Harrie Weinans et Amir Abbas Zadpoor. 2013. « Mechanical properties of open-cell metallic biomaterials manufactured using additive manufacturing ». *Materials & Design,* vol. 49, p. 957-965.

Cansizoglu, O., Ola L. A. Harrysson, D. Cormier, H. West et T. Mahale. 2008. « Properties of Ti–6Al–4V non-stochastic lattice structures fabricated via electron beam melting ». *Materials Science and Engineering: A,* vol. 492, n° 1, p. 468-474.

Chan, Kwai S., Marie Koike, Robert L. Mason et Toru Okabe. 2013. « Fatigue Life of Titanium Alloys Fabricated by Additive Layer Manufacturing Techniques for Dental Implants ». *Metallurgical and Materials Transactions A,* vol. 44, n° 2, p. 1010-1022.

Chanda, S., A. Dickinson, S. Gupta et M. Browne. 2015. « Full-field in vitro measurements and in silico predictions of strain shielding in the implanted femur after total hip arthroplasty ». *Proceedings of the Institution of Mechanical Engineers. Part H, Journal of engineering in medicine,* vol. 229, n° 8, p. 549-59.

Cheng, Alice, Aiza Humayun, David J. Cohen, Barbara D. Boyan et Zvi Schwartz. 2014. « Additively manufactured 3D porous Ti-6Al-4V constructs mimic trabecular bone structure and regulate osteoblast proliferation, differentiation and local factor production in a porosity and surface roughness dependent manner ». *Biofabrication,* vol. 6, n° 4, p. 045007.

Cheng, X. Y., S. J. Li, L. E. Murr, Z. B. Zhang, Y. L. Hao, R. Yang, F. Medina et R. B. Wicker. 2012. « Compression deformation behavior of Ti–6Al–4V alloy with cellular structures fabricated by electron beam melting ». *Journal of the Mechanical Behavior of Biomedical Materials,* vol. 16, nº 0, p. 153-162.

Coelho, P. G., P. R. Fernandes, H. C. Rodrigues, J. B. Cardoso et J. M. Guedes. 2009. « Numerical modeling of bone tissue adaptation—A hierarchical approach for bone apparent density and trabecular structure ». *Journal of Biomechanics,* vol. 42, nº 7, p. 830-837.

Concept Laser GmbH. < http://www.concept-laser.de/ >. Consulté le 2016-09-25.

Cook, Stephen D, Nisra Thongpreda, Ronald C Anderson et Ray J Haddad. 1988. « The effect of post-sintering heat treatments on the fatigue properties of porous coated Ti-6Al-4V Alloy ». *Journal of biomedical materials research,* vol. 22, nº 4, p. 287-302.

Currey, John D. 2012. « The structure and mechanics of bone ». *Journal of Materials Science,* vol. 47, nº 1, p. 41-54.

Davis, NG, J Teisen, C Schuh et DC Dunand. 2001. « Solid-state foaming of titanium by superplastic expansion of argon-filled pores ». *Journal of Materials Research,* vol. 16, nº 05, p. 1508-1519.

Daxner, T. 2002. « Multi-scale Modeling and Simulation of Metallic Foams ». VDI-Verlag.

de Pablo, Juan J, et William A Curtin. 2007. « Multiscale modeling in advanced materials research: challenges, novel methods, and emerging applications ». *MRS Bulletin,* vol. 32, nº 11, p. 905-911.

DeGiorgi, V. G., et M. A. Qidqai. 2002. « A computational mesoscale evaluation of material characteristics of porous shape memory alloys ». *Smart Materials and Structures,* vol. 11, nº 3, p. 435-43.

Dickinson, A. S., A. C. Taylor, H. Ozturk et M. Browne. 2011. « Experimental Validation of a Finite Element Model of the Proximal Femur Using Digital Image Correlation and a Composite Bone Model ». *Journal of Biomechanical Engineering,* vol. 133, nº 1, p. 014504-014504.

Dukhan, N. 2013. *Metal Foams: Fundamentals and Applications*. Lancaster, Illinois, USA: Destech Publications.

Elahinia, Mohammad, Narges Shayesteh Moghaddam, Mohsen Taheri Andani, Amirhesam Amerinatanzi, Beth A. Bimber et Reginald F. Hamilton. 2016. « Fabrication of NiTi through additive manufacturing: A review ». *Progress in Materials Science,* vol. 83, p. 630-663.

Elliott, JA. 2011. « Novel approaches to multiscale modelling in materials science ». *International Materials Reviews,* vol. 56, n° 4, p. 207-225.

EOS GmbH Electro Optical Systems. < http://www.eos.info/ >. Consulté le 2016-09-25.

Fang, Qianqian. 2008. *A registration toolbox for FEM surface meshes.* < http://iso2mesh.sourceforge.net/ >. Consulté le July 11, 2016.

Frazier, William E. 2014. « Metal additive manufacturing: A review ». *Journal of Materials Engineering and Performance,* vol. 23, n° 6, p. 1917-1928.

Fujibayashi, Shunsuke, Masashi Neo, Hyun-Min Kim, Tadashi Kokubo et Takashi Nakamura. 2004. « Osteoinduction of porous bioactive titanium metal ». *Biomaterials,* vol. 25, n° 3, p. 443-450.

Gauthier, Maxime, Louis-Philippe Lefebvre, Yannig Thomas et Martin N. Bureau. 2004. « Production of metallic foams having open porosity using a powder metallurgy approach ». *Materials and manufacturing processes,* vol. 19, n° 5, p. 793-811.

Gibson, L. J., et M. F. Ashby (183-189). 1999. *Cellular Solids: Structure and properties*, 2nd. Cambridge: Cambridge University Press, 510 p.

Gibson, L.J., M.F. Ashby et B.A. Harley. 2010. *Cellular Materials in Nature and Medicine*, 1st. Cambridge University Press, 309 p.

Gibson, Lorna J. 2005. « Biomechanics of cellular solids ». *Journal of Biomechanics,* vol. 38, n° 3, p. 377-399.

GOM mbH. 2007. *ARAMIS v6.3 User Manual Software*.

Grassi, Lorenzo, Sami P. Väänänen, Saber Amin Yavari, Harrie Weinans, Jukka S. Jurvelin, Amir A. Zadpoor et Hanna Isaksson. 2013. « Experimental validation of finite element model for proximal composite femur using optical measurements ». *Journal of the Mechanical Behavior of Biomedical Materials,* vol. 21, p. 86-94.

Hansen, Ulrich, Peter Zioupos, Rebecca Simpson, John D. Currey et David Hynd. 2008. « The Effect of Strain Rate on the Mechanical Properties of Human Cortical Bone ». *Journal of Biomechanical Engineering-Transaction of the ASME,* vol. 130, n° 1, p. 011011-011011.

Hao, Yu-Lin, Shu-Jun Li et Rui Yang. 2016. « Biomedical titanium alloys and their additive manufacturing ». *Rare Metals*, p. 1-11.

Harrysson, Ola L. A., Omer Cansizoglu, Denis J. Marcellin-Little, Denis R. Cormier et Harvey A. West Ii. 2008. « Direct metal fabrication of titanium implants with tailored materials and mechanical properties using electron beam melting technology ». *Materials Science and Engineering: C,* vol. 28, n° 3, p. 366-373.

Hazlehurst, Kevin Brian. 2014. « The adoption of laser melting technology for the manufacture of functionally graded cobalt chrome alloy femoral stems ». University of Wolverhampton. < http://hdl.handle.net/2436/332114 >. Consulté le 2014-10-06t14:15:07z.

Hazlehurst, Kevin Brian, Chang Jiang Wang et Mark Stanford. 2014. « An investigation into the flexural characteristics of functionally graded cobalt chrome femoral stems manufactured using selective laser melting ». *Materials & Design,* vol. 60, p. 177-183.

Hazlehurst, Kevin, Chang Jiang Wang et Mark Stanford. 2013. « Evaluation of the stiffness characteristics of square pore CoCrMo cellular structures manufactured using laser melting technology for potential orthopaedic applications ». *Materials & Design,* vol. 51, p. 949-955.

Hedayati, R., M. Sadighi, M. Mohammadi-Aghdam et A. A. Zadpoor. 2016. « Mechanical properties of regular porous biomaterials made from truncated cube repeating unit cells: Analytical solutions and computational models ». *Materials Science and Engineering: C,* vol. 60, p. 163-183.

Heinl, Peter, Lenka Müller, Carolin Körner, Robert F. Singer et Frank A. Müller. 2008. « Cellular Ti–6Al–4V structures with interconnected macro porosity for bone implants fabricated by selective electron beam melting ». *Acta Biomaterialia,* vol. 4, n° 5, p. 1536-1544.

Hilliard, John E, et Lawrence R Lawson. 2003. *Stereology and stochastic geometry (Computational Imaging and Vision)*, 28, 1st. Dordrecht: Kluwer Academic Publishers.

Ho, Saey Tuan, et Dietmar W Hutmacher. 2006. « A comparison of micro CT with other techniques used in the characterization of scaffolds ». *Biomaterials,* vol. 27, n° 8, p. 1362-1376.

Holcombe, Sven 2008. *STL Write - Export a variety of inputs (patch, surface) to an STL triangular mesh.* < http://www.mathworks.com/matlabcentral/fileexchange/20922-stlwrite-filename--varargin- >. Consulté le July 11, 2016.

Horn, Timothy J., Ola L. A. Harrysson, Denis J. Marcellin-Little, Harvey A. West, B. Duncan X. Lascelles et Ronald Aman. 2014. « Flexural properties of Ti6Al4V rhombic dodecahedron open cellular structures fabricated with electron beam melting ». *Additive Manufacturing,* vol. 1, n° 0, p. 2-11.

Hrabe, Nikolas W., Peter Heinl, Brian Flinn, Carolin Körner et Rajendra K. Bordia. 2011. « Compression-compression fatigue of selective electron beam melted cellular titanium

(Ti-6Al-4V) ». *Journal of Biomedical Materials Research Part B: Applied Biomaterials,* vol. 99B, nº 2, p. 313-320.

Huiskes, R., H. Weinans, H. J. Grootenboer, M. Dalstra, B. Fudala et T. J. Slooff. 1987. « Adaptive bone-remodeling theory applied to prosthetic-design analysis ». *Journal of Biomechanics,* vol. 20, nº 11, p. 1135-1150.

Huiskes, Rik, Harrie Weinans et Bert Van Rietbergen. 1992. « The Relationship Between Stress Shielding and Bone Resorption Around Total Hip Stems and the Effects of Flexible Materials ». *Clinical Orthopaedics and Related Research,* vol. 274, p. 124-134.

Imwinkelried, Thomas. 2007. « Mechanical properties of open-pore titanium foam ». *Journal of Biomedical Materials Research Part A,* vol. 81, nº 4, p. 964-970.

Institut Canadien d'Information sur la Santé. 2015. « Arthroplasties de la hanche et du genou au Canada : rapport annuel de 2015 du Registre canadien des remplacements articulaires ». *Rapports du Registre canadien des remplacements articulaires*.

ISO 7206-4. 2010. *Implants for surgery - Partial and total hip joint prostheses - Part 4: Determination of endurance properties and performance of stemmed femoral components*. ISO - International Organization for Standardization. Consulté le 30 Apr 2016.

Jang, Wen-Yea, Stelios Kyriakides et Andrew M. Kraynik. 2010. « On the compressive strength of open-cell metal foams with Kelvin and random cell structures ». *International Journal of Solids and Structures,* vol. 47, nº 21, p. 2872-2883.

Kahn-Jetter, Z. L., et T. C. Chu. 1990. « Three-dimensional displacement measurements using digital image correlation and photogrammic analysis ». *Experimental Mechanics,* vol. 30, nº 1, p. 10-16.

Ke, X, M A Sutton, S M Lessner et M Yost. 1999. « Towards the standardization of in vitro load transfer investigations of hip prostheses ». *The Journal of Strain Analysis for Engineering Design,* vol. 34, nº 1, p. 1-15.

Khanoki, Sajad Arabnejad, R. Burnett Johnston, Jenny Ann Pura, Baljinder Singh, Michael Tanzer et Damiano Pasini. 2016. « High-strength porous biomaterials for bone replacement: A strategy to assess the interplay between cell morphology, mechanical properties, bone ingrowth and manufacturing constraints ». *Acta Biomaterialia,* vol. 30, p. 345-356.

Khanoki, Sajad Arabnejad, et Damiano Pasini. 2012. « Multiscale design and multiobjective optimization of orthopedic hip implants with functionally graded cellular material ».

Journal of Biomechanical Engineering-Transaction of the ASME, vol. 134, nº 3, p. 031004.

Kim, Hyun-Min, Fumiaki Miyaji, Tadashi Kokubo et Takashi Nakamura. 1996. « Preparation of bioactive Ti and its alloys via simple chemical surface treatment ». *Journal of biomedical materials research,* vol. 32, nº 3, p. 409-417.

Kröger, Heikki, Petri Venesmaa, Jukka Jurvelin, Hannu Miettinen, Olavi Suomalainen et Esko Alhava. 1998. « Bone density at the proximal femur after total hip arthroplasty ». *Clinical orthopaedics and related research,* vol. 352, p. 66-74.

Kruth, J. P., L. Froyen, J. Van Vaerenbergh, P. Mercelis, M. Rombouts et B. Lauwers. 2004. « Selective laser melting of iron-based powder ». *Journal of Materials Processing Technology,* vol. 149, nº 1–3, p. 616-622.

Kruth, Jean-Pierre, Peter Mercelis, J Van Vaerenbergh, Ludo Froyen et Marleen Rombouts. 2005. « Binding mechanisms in selective laser sintering and selective laser melting ». *Rapid prototyping journal,* vol. 11, nº 1, p. 26-36.

Kurtz, Steven, Kevin Ong, Edmund Lau, Fionna Mowat et Michael Halpern. 2007. « Projections of Primary and Revision Hip and Knee Arthroplasty in the United States from 2005 to 2030 ». *The Journal of Bone & Joint Surgery,* vol. 89, nº 4, p. 780-785.

Kwon, Y. W., R. E. Cooke et C. Park. 2003. « Representative unit-cell models for open-cell metal foams with or without elastic filler ». *Materials Science and Engineering: A,* vol. A343, nº 1-2, p. 63-70.

Lefebvre, Louis-Philippe. 2013. « Porous Metals and Metallic Foams in Orthopedic Applications ». In *Metal Foams: Fundamentals and Applications*, sous la dir. de Dukhan, N., p. 317-362. Lancaster: DEStech Publications, Inc. < http://books.google.ca/books?id=xZRG1EyBbzsC >.

Leong, K. F., C. M. Cheah et C. K. Chua. 2003. « Solid freeform fabrication of three-dimensional scaffolds for engineering replacement tissues and organs ». *Biomaterials,* vol. 24, nº 13, p. 2363-2378.

Levine, Brett Russell, Scott Sporer, Robert A. Poggie, Craig J. Della Valle et Joshua J. Jacobs. 2006. « Experimental and clinical performance of porous tantalum in orthopedic surgery ». *Biomaterials,* vol. 27, nº 27, p. 4671-4681.

Li, Bing-Yun, Li-Jian Rong, Yi-Yi Li et VE Gjunter. 2000. « Fabrication of cellular NiTi intermetallic compounds ». *Journal of materials research,* vol. 15, nº 01, p. 10-13.

Li, Jia Ping, Shi Hong Li, K De Groot et Pierre Layrolle. 2002. « Preparation and characterization of porous titanium ». In *Bioceramics 14*. Vol. 218, p. 51-54. Key Engineering Materials - Trans Tech Publ.

Li, S. J., L. E. Murr, X. Y. Cheng, Z. B. Zhang, Y. L. Hao, R. Yang, F. Medina et R. B. Wicker. 2012. « Compression fatigue behavior of Ti–6Al–4V mesh arrays fabricated by electron beam melting ». *Acta Materialia,* vol. 60, nº 3, p. 793-802.

Li, Yong-Hua, Li-Jian Rong et Yi-Yi Li. 2002. « Compressive property of porous NiTi alloy synthesized by combustion synthesis ». *Journal of alloys and compounds,* vol. 345, nº 1, p. 271-274.

Lipinski, P., A. Barbas et A. S. Bonnet. 2013. « Fatigue behavior of thin-walled grade 2 titanium samples processed by selective laser melting. Application to life prediction of porous titanium implants ». *Journal of the Mechanical Behavior of Biomedical Materials,* vol. 28, p. 274-290.

Maire, E, F Wattebled, JY Buffiere et G Peix. 2006. « Deformation of a Metallic Foam Studied by X-Ray Computed Tomography and Finite Element Calculations ». *Microstructural Investigation and Analysis, Volume 4*, p. 68-73.

Maire, E., A. Elmoutaouakkil, A. Fazekas et L. Salvo. 2003. « In Situ X-Ray Tomography Measurements of Deformation in Cellular Solids ». *MRS Bulletin,* vol. 28, nº 4, p. 284-289.

Maire, Eric, Paolo Colombo, Jerome Adrien, Laurent Babout et Lisa Biasetto. 2007. « Characterization of the morphology of cellular ceramics by 3D image processing of X-ray tomography ». *Journal of the European Ceramic Society,* vol. 27, nº 4, p. 1973-1981.

Maîtrejean, Guillaume, Patrick Terriault et Vladimir Brailovski. 2013a. « Density Dependence of the Macroscale Superelastic Behavior of Porous Shape Memory Alloys: A Two-Dimensional Approach ». *Smart Materials Research,* vol. 2013, p. 13.

Maîtrejean, Guillaume, Patrick Terriault et Vladimir Brailovski. 2013b. « Density dependence of the superelastic behavior of porous shape memory alloys: Representative Volume Element and scaling relation approaches ». *Computational Materials Science,* vol. 77, nº 0, p. 93-101.

Maîtrejean, Guillaume, Patrick Terriault, Diego Devís Capilla et Vladimir Brailovski. 2014. « Unit Cell Analysis of the Superelastic Behavior of Open-Cell Tetrakaidecahedral Shape Memory Alloy Foam under Quasi-Static Loading ». *Smart Materials Research,* vol. 2014, nº 0, p. 11.

Mangipudi, K. R., et P. R. Onck. 2011. « Multiscale modelling of damage and failure in two-dimensional metallic foams ». *Journal of the Mechanics and Physics of Solids,* vol. 59, n° 7, p. 1437-1461.

Marshall, AJ, et BD Ratner. 2005. « Quantitative characterization of sphere-templated porous biomaterials ». *AIChE journal,* vol. 51, n° 4, p. 1221-1232.

Martin, R.B. 1984. « Porosity and specific surface of bone ». *CRC Critical Reviews In Biomedical Engineering,* vol. 10, n° 3, p. 179-222.

Maskery, I., A. O. Aremu, M. Simonelli, C. Tuck, R. D. Wildman, I. A. Ashcroft et R. J. M. Hague. 2015. « Mechanical Properties of Ti-6Al-4V Selectively Laser Melted Parts with Body-Centred-Cubic Lattices of Varying cell size ». *Experimental Mechanics,* vol. 55, n° 7, p. 1261-1272.

Matějíček, Jiří, Blahoslav Kolman, Jiří Dubský, Karel Neufuss, Noel Hopkins et Jochen Zwick. 2006. « Alternative methods for determination of composition and porosity in abradable materials ». *Materials Characterization,* vol. 57, n° 1, p. 17-29.

Michailidis, N., F. Stergioudi, H. Omar et D. N. Tsipas. 2008. « Investigation of the mechanical behavior of open-cell Ni foams by experimental and FEM procedures ». *Advanced Engineering Materials,* vol. 10, n° 12, p. 1122-6.

Michailidis, N., F. Stergioudi, H. Omar et D. N. Tsipas. 2010. « An image-based reconstruction of the 3D geometry of an Al open-cell foam and FEM modeling of the material response ». *Mechanics of Materials,* vol. 42, n° 2, p. 142-147.

Min, Byung-Moo, Gene Lee, So Hyun Kim, Young Sik Nam, Taek Seung Lee et Won Ho Park. 2004. « Electrospinning of silk fibroin nanofibers and its effect on the adhesion and spreading of normal human keratinocytes and fibroblasts in vitro ». *Biomaterials,* vol. 25, n° 7–8, p. 1289-1297.

Morlock, M., E. Schneider, A. Bluhm, M. Vollmer, G. Bergmann, V. Müller et M. Honl. 2001. « Duration and frequency of every day activities in total hip patients ». *Journal of Biomechanics,* vol. 34, n° 7, p. 873-881.

Muliana, Anastasia Hanifah, et Rami Haj-Ali. 2005. « Multiscale Modeling for the Long-Term Behavior of Laminated Composite Structures ». *AIAA Journal,* vol. 43, n° 8, p. 1815-1822.

Mullen, Lewis, Robin C. Stamp, Peter Fox, Eric Jones, Chau Ngo et Christopher J. Sutcliffe. 2010. « Selective laser melting: A unit cell approach for the manufacture of porous, titanium, bone in-growth constructs, suitable for orthopedic applications. II. Randomized structures ». *Journal of Biomedical Materials Research Part B: Applied Biomaterials,* vol. 92B, n° 1, p. 178-188.

Murr, L. E., K. N. Amato, S. J. Li, Y. X. Tian, X. Y. Cheng, S. M. Gaytan, E. Martinez, P. W. Shindo, F. Medina et R. B. Wicker. 2011. « Microstructure and mechanical properties of open-cellular biomaterials prototypes for total knee replacement implants fabricated by electron beam melting ». *Journal of the Mechanical Behavior of Biomedical Materials,* vol. 4, n° 7, p. 1396-1411.

Murr, L. E., S. M. Gaytan, F. Medina, E. Martinez, J. L. Martinez, D. H. Hernandez, B. I. Machado, D. A. Ramirez et R. B. Wicker. 2010a. « Characterization of Ti–6Al–4V open cellular foams fabricated by additive manufacturing using electron beam melting ». *Materials Science and Engineering: A,* vol. 527, n° 7, p. 1861-1868.

Murr, LE, SM Gaytan, F Medina, H Lopez, E Martinez, BI Machado, DH Hernandez, L Martinez, MI Lopez et RB Wicker. 2010b. « Next-generation biomedical implants using additive manufacturing of complex, cellular and functional mesh arrays ». *Philosophical Transactions of the Royal Society A: Mathematical, Physical and Engineering Sciences,* vol. 368, n° 1917, p. 1999-2032.

Nemat-Nasser, Sia, Yu Su, Wei-Guo Guo et Jon Isaacs. 2005. « Experimental characterization and micromechanical modeling of superelastic response of a porous NiTi shape-memory alloy ». *Journal of the Mechanics and Physics of Solids,* vol. 53, n° 10, p. 2320-2346.

Niu, Wenjuan, Chenguang Bai, GuiBao Qiu et Qiang Wang. 2009. « Processing and properties of porous titanium using space holder technique ». *Materials Science and Engineering: A,* vol. 506, n° 1, p. 148-151.

Otsuki, Bungo, Mitsuru Takemoto, Shunsuke Fujibayashi, Masashi Neo, Tadashi Kokubo et Takashi Nakamura. 2006. « Pore throat size and connectivity determine bone and tissue ingrowth into porous implants: three-dimensional micro-CT based structural analyses of porous bioactive titanium implants ». *Biomaterials,* vol. 27, n° 35, p. 5892-5900.

Pabst, W., E. Gregorová, I. Sedlářová et M. Černý. 2011. « Preparation and characterization of porous alumina–zirconia composite ceramics ». *Journal of the European Ceramic Society,* vol. 31, n° 14, p. 2721-2731.

Panico, M., et L. C. Brinson. 2008. « Computational modeling of porous shape memory alloys ». *International Journal of Solids and Structures,* vol. 45, n° 21, p. 5613-26.

Parthasarathy, Jayanthi, Binil Starly et Shivakumar Raman. 2011. « A design for the additive manufacture of functionally graded porous structures with tailored mechanical properties for biomedical applications ». *Journal of Manufacturing Processes,* vol. 13, n° 2, p. 160-170.

Parthasarathy, Jayanthi, Binil Starly, Shivakumar Raman et Andy Christensen. 2010. « Mechanical evaluation of porous titanium (Ti6Al4V) structures with electron beam melting (EBM) ». *Journal of the Mechanical Behavior of Biomedical Materials,* vol. 3, n^{o} 3, p. 249-259.

Pattanayak, D. K., A. Fukuda, T. Matsushita, M. Takemoto, S. Fujibayashi, K. Sasaki, N. Nishida, T. Nakamura et T. Kokubo. 2011. « Bioactive Ti metal analogous to human cancellous bone: Fabrication by selective laser melting and chemical treatments ». *Acta Biomater,* vol. 7, n^{o} 3, p. 1398-406.

Petit, Clémence, Eric Maire, Sylvain Meille, Jérôme Adrien, Shingo Kurosu et Akihiko Chiba. 2016. « CoCrMo cellular structures made by Electron Beam Melting studied by local tomography and finite element modelling ». *Materials Characterization,* vol. 116, p. 48-54.

Qidwai, Muhammad A, Pavlin B Entchev, Dimitris C Lagoudas et Virginia G DeGiorgi. 2001. « Modeling of the thermomechanical behavior of porous shape memory alloys ». *International journal of solids and structures,* vol. 38, n^{o} 48, p. 8653-8671.

Ramirez, D. A., L. E. Murr, S. J. Li, Y. X. Tian, E. Martinez, J. L. Martinez, B. I. Machado, S. M. Gaytan, F. Medina et R. B. Wicker. 2011. « Open-cellular copper structures fabricated by additive manufacturing using electron beam melting ». *Materials Science and Engineering: A,* vol. 528, n^{o} 16, p. 5379-5386.

Rasband, W.S. « ImageJ, U. S. National Institutes of Health, Bethesda, Maryland, USA, http://imagej.nih.gov/ij/, 1997-2012. ».

Rivard, J., V. Brailovski, S. Dubinskiy et S. Prokoshkin. 2014. « Fabrication, morphology and mechanical properties of Ti and metastable Ti-based alloy foams for biomedical applications ». *Materials Science and Engineering: C,* vol. 45, n^{o} 0, p. 421-433.

Roberts, A. P., et E. J. Garboczi. 2002. « Elastic properties of model random three-dimensional open-cell solids ». *Journal of the Mechanics and Physics of Solids,* vol. 50, n^{o} 1, p. 33-55.

Robertson, Diane M, Leon St Pierre et Ramlal Chahal. 1976. « Preliminary observations of bone ingrowth into porous materials ». *Journal of biomedical materials research,* vol. 10, n^{o} 3, p. 335-344.

Ronan, William, Vikram S. Deshpande et Norman A. Fleck. 2016. « The tensile ductility of cellular Solids: The role of imperfections ». *International Journal of Solids and Structures*.

Rouquerol, J., D. Avnir, C. W. Fairbridge, D. H. Everett, J. M. Haynes, N. Pernicone, J. D. F. Ramsay, K. S. W. Sing et K. K. Unger. 1994. « Recommendations for the characterization of porous solids (Technical Report) ». *Pure and Applied Chemistry,* vol. 66, n^{o} 8, p. 1739-1758.

Roy, Sandipan, Niloy Khutia, Debdulal Das, Mitun Das, Vamsi Krishna Balla, Amit Bandyopadhyay et Amit Roy Chowdhury. 2016. « Understanding compressive deformation behavior of porous Ti using finite element analysis ». *Materials Science and Engineering: C,* vol. 64, p. 436-443.

Rozicka, M., J. Had, V. Kulisek et O. Uher. 2011. « Multiscale modeling of hybrid composite structures ». *Key Engineering Materials,* vol. 471-472, p. 916-21.

Ryan, Garrett E., Abhay S. Pandit et Dimitrios P. Apatsidis. 2008. « Porous titanium scaffolds fabricated using a rapid prototyping and powder metallurgy technique ». *Biomaterials,* vol. 29, n° 27, p. 3625-3635.

Ryan, Garrett, Patrick McGarry, Abhay Pandit et Dimitrios Apatsidis. 2009. « Analysis of the mechanical behavior of a titanium scaffold with a repeating unit-cell substructure ». *Journal of Biomedical Materials Research Part B: Applied Biomaterials,* vol. 90, n° 2, p. 894-906.

Ryan, Garrett, Abhay Pandit et Dimitrios Panagiotis Apatsidis. 2006. « Fabrication methods of porous metals for use in orthopaedic applications ». *Biomaterials,* vol. 27, n° 13, p. 2651-2670.

Schladitz, Katja, Claudia Redenbach, Tetyana Sych et Michael Godehardt. 2008. *Microstructural characterisation of open foams using 3d images*, 1st. Kaiserslautern: ITWM, Fraunhofer Inst. Techno-und Wirtschaftsmathematik, 30 p.

Schmalzried, T P, M Jasty et W H Harris. 1992. « Periprosthetic bone loss in total hip arthroplasty. Polyethylene wear debris and the concept of the effective joint space ». *The Journal of Bone & Joint Surgery,* vol. 74, n° 6, p. 849-863.

Seah, KHW, R Thampuran et SH Teoh. 1998. « The influence of pore morphology on corrosion ». *Corrosion Science,* vol. 40, n° 4, p. 547-556.

Shahbeyk, Sharif. 2013. « Yield/Failure Criteria, Constitutive Models, and Crashworthiness Applications of Metal Foams ». In *Metal Foams: Fundamentals and Applications*, sous la dir. de Dukhan, N., p. 131-216. Lancaster: DEStech Publications, Inc. < http://books.google.ca/books?id=xZRG1EyBbzsC >.

Shen, H., S. M. Oppenheimer, D. C. Dunand et L. C. Brinson. 2006. « Numerical modeling of pore size and distribution in foamed titanium ». *Mechanics of Materials,* vol. 38, n° 8–10, p. 933-944.

Shen, Hui, et L. Catherine Brinson. 2006. « A numerical investigation of the effect of boundary conditions and representative volume element size for porous titanium ». *Journal of Mechanics of Materials and Structures,* vol. 1, n° 7, p. 1179-1204.

Simoneau, C., V. Brailovski et P. Terriault. 2016. « Design, manufacture and tensile properties of stochastic porous metallic structures ». *Mechanics of Materials,* vol. 94, p. 26-37.

Simoneau, Charles, Patrick Terriault, Jonathan Rivard et Vladimir Brailovski. 2014. « Modeling of metallic foam morphology using the Representative Volume Element approach: Development and experimental validation ». *International Journal of Solids and Structures,* vol. 51, n^o 21–22, p. 3633-3641.

Singh, R, PD Lee, RJ Dashwood et TC Lindley. 2010a. « Titanium foams for biomedical applications: a review ». *Materials Science and Technology,* vol. 25, n^o 3-4, p. 127-136.

Singh, R, PD Lee, TC Lindley, C Kohlhauser, C Hellmich, M Bram, T Imwinkelried et RJ Dashwood. 2010b. « Characterization of the deformation behavior of intermediate porosity interconnected Ti foams using micro-computed tomography and direct finite element modeling ». *Acta biomaterialia,* vol. 6, n^o 6, p. 2342-2351.

Sotomayor, Oscar E., et Hareesh V. Tippur. 2014. « Role of cell regularity and relative density on elastoplastic compression response of 3-D open-cell foam core sandwich structure generated using Voronoi diagrams ». *Acta Materialia,* vol. 78, n^o 0, p. 301-313.

Spoerke, Erik D., Naomi G. Murray, Huanlong Li, L. Catherine Brinson, David C. Dunand et Samuel I. Stupp. 2005. « A bioactive titanium foam scaffold for bone repair ». *Acta Biomaterialia,* vol. 1, n^o 5, p. 523-533.

Takahashi, Yuji, Dai Okumura et Nobutada Ohno. 2010. « Yield and buckling behavior of Kelvin open-cell foams subjected to uniaxial compression ». *International Journal of Mechanical Sciences,* vol. 52, n^o 2, p. 377-385.

Tang, Liqun, Xuepeng Shi, Lue Zhang, Zejia Liu, Zhenyu Jiang et Yiping Liu. 2014. « Effects of statistics of cell's size and shape irregularity on mechanical properties of 2D and 3D Voronoi foams ». *Acta Mechanica,* vol. 225, n^o 4-5, p. 1361-1372.

Taylor, M. 2006. « Finite element analysis of the resurfaced femoral head ». *Proceedings of the Institution of Mechanical Engineers, Part H (Journal of Engineering in Medicine),* vol. 220, n^o H2, p. 289-97.

Tayton, E., S. Evans et D. O'Doherty. 2010. « Mapping the strain distribution on the proximal femur with titanium and flexible-stemmed implants using digital image correlation ». *Bone & Joint Journal,* vol. 92-B, n^o 8, p. 1176-1181.

Terriault, Patrick, et Vladimir Brailovski. 2013. « Implementation of Likhachev's model into a finite element program ». In *9th European Symposium on Martensitic Transformations, ESOMAT 2012, September 9, 2012 - September 16, 2012*. (Saint-Petersburg, Russia) Vol. 738-739, p. 160-164. Coll. « Materials Science Forum »:

Trans Tech Publications Ltd. < http://dx.doi.org/10.4028/www.scientific.net/MSF.738-739.160 >.

Terriault, Patrick, Guillaume Maîtrejean et Vladimir Brailovski. 2013. « Modeling of Superelastic Porous Materials ». In *SMST-2013 Proceedings of the International Conference on Shape Memory and Superelastic Technologies*. (Prague, Czech Republic), sous la dir. de International, ASM, p. 332 - 333 (2). ASM International.

Turner, TM, DR Sumner, RM Urban, DP Rivero et JO Galante. 1986. « A comparative study of porous coatings in a weight-bearing total hip-arthroplasty model ». *Journal of Bone and Joint Surgery - American Volume,* vol. 68, n^{o} 9, p. 1396-409.

U.S. Food and Drug Administration. 2016. « 3D Printing of Medical Devices ». < http://www.fda.gov/MedicalDevices/ProductsandMedicalProcedures/3DPrintingofMedicalDevices/default.htm >.

Van Hooreweder, Brecht, Yanni Apers, Karel Lietaert et Jean-Pierre Kruth. 2016. « Improving the fatigue performance of porous metallic biomaterials produced by Selective Laser Melting ». *Acta Biomaterialia*.

Vandenbroucke, Ben, et Jean-Pierre Kruth. 2007. « Selective laser melting of biocompatible metals for rapid manufacturing of medical parts ». *Rapid Prototyping Journal,* vol. 13, n^{o} 4, p. 196-203.

Volume Graphics. 2016. < http://www.volumegraphics.com/en/ >. Consulté le 2016-10-11.

Wang, Xiaojian, Yuncang Li, Jianyu Xiong, P. D. Hodgson et Cui'e Wen. 2009. « Porous TiNbZr alloy scaffolds for biomedical applications ». *Acta Biomaterialia,* vol. 5, n^{o} 9, p. 3616-24.

Wieding, Jan, Andreas Wolf et Rainer Bader. 2014. « Numerical optimization of open-porous bone scaffold structures to match the elastic properties of human cortical bone ». *Journal of the Mechanical Behavior of Biomedical Materials,* vol. 37, p. 56-68.

Willert, H. G., et M. Semlitsch. 1977. « Reactions of the articular capsule to wear products of artificial joint prostheses ». *Journal of Biomedical Materials Research,* vol. 11, n^{o} 2, p. 157-164.

Yamako, Go, Etsuo Chosa, Koji Totoribe, Shuji Hanada, Naoya Masahashi, Norikazu Yamada et Eiji Itoi. 2014. « In-vitro biomechanical evaluation of stress shielding and initial stability of a low-modulus hip stem made of β type Ti-33.6Nb-4Sn alloy ». *Medical Engineering & Physics,* vol. 36, n^{o} 12, p. 1665-1671.

Yan, Chunze, Liang Hao, Ahmed Hussein et Philippe Young. 2015. « Ti–6Al–4V triply periodic minimal surface structures for bone implants fabricated via selective laser melting ». *Journal of the Mechanical Behavior of Biomedical Materials,* vol. 51, p. 61-73.

Yan, Wenyi, Julien Berthe et Cuie Wen. 2011. « Numerical investigation of the effect of porous titanium femoral prosthesis on bone remodeling ». *Materials & Design,* vol. 32, n° 4, p. 1776-1782.

Yu, Mao-hong. 2002. « Advances in strength theories for materials under complex stress state in the 20th century ». *Applied Mechanics Reviews,* vol. 55, n° 3, p. 169-218.

Yue, S, RM Pilliar et GC Weatherly. 1984. « The fatigue strength of porous-coated Ti–6% Al–4% V implant alloy ». *Journal of biomedical materials research,* vol. 18, n° 9, p. 1043-1058.

Zhang, Dongsheng, et Dwayne D. Arola. 2004. « Applications of digital image correlation to biological tissues ». *Journal of Biomedical Optics,* vol. 9, n° 4, p. 691-699.

Zhao, S., S. J. Li, W. T. Hou, Y. L. Hao, R. Yang et L. E. Murr. 2016. « Microstructure and mechanical properties of open cellular Ti–6Al–4V prototypes fabricated by electron beam melting for biomedical applications ». *Materials Technology,* vol. 31, n° 2, p. 98-107.

Zhao, Ying, et Minoru Taya. 2006. « Analytical Modeling for Stress-Strain Curve of a Porous NiTi ». *Journal of Applied Mechanics,* vol. 74, n° 2, p. 291-297.

Zhiye, Gao, et Hu Qinhong. 2013. « Estimating permeability using median pore-throat radius obtained from mercury intrusion porosimetry ». *Journal of Geophysics and Engineering,* vol. 10, n° 2, p. 025014.